



ISSN 1590-2595

# quaderni di geofisica

n. 43

*Proceeding of the GNV Project Meeting*

## **DEVELOPMENT AND APPLICATION OF REMOTE SENSING METHODS FOR THE MONITORING OF ACTIVE ITALIAN VOLCANOES**

Edited by  
Mauro Coltelli

**Istituto Nazionale di Geofisica e Vulcanologia**

**2006**

**Direttore**

Enzo Boschi

**Editorial Board**

Raffaele Azzaro (CT)

Sara Barsotti (PI)

Viviana Castelli (MI)

Anna Grazia Chiodetti (AC)

Rosa Anna Corsaro (CT)

Luigi Cucci (RM1)

Mauro Di Vito (NA)

Sergio Gurrieri (PA)

Lucia Margheriti (CNT)

Simona Masina (BO)

Nicola Pagliuca (RM1)

Leonardo Sagnotti (RM2)

Salvatore Stramondo (CNT)

Andrea Tertulliani - coordinatore (RM1)

Gianluca Valensise (RM1)

Gaetano Zonno (MI)

**Segreteria di Redazione**

Francesca Di Stefano - responsabile

Tel. +39 06 51860055

Fax +39 06 36915617

Sabrina Palone

Tel. +39 06 51860405

Fax +39 06 51860585

redazionecen@ingv.it

quaderni  
di  
geofisica





*In the framework of the GNV Program 2000-2002 - Coordinated Project #13*

*Proceeding of the GNV Project Meeting:*

**DEVELOPMENT AND APPLICATION OF REMOTE  
SENSING METHODS FOR THE MONITORING OF  
ACTIVE ITALIAN VOLCANOES**

*Edited by*

*Mauro Coltelli*

*Istituto Nazionale di Geofisica e Vulcanologia*

*Sezione di Catania*

*Piazza Roma 2, Catania, Italy*



## Table of Contents

Preface .....	7
Geodetical/SAR monitoring of the Neapolitan volcanic district <i>Borgström S. et al.</i> .....	9
Application of differential SAR interferometry for studying eruptive event of 22 July 1998 at Mt. Etna <i>Coltelli M. et al.</i> .....	15
Report on observations and modeling of coupled magma chamber inflation and flank motion on Mt. Etna volcano <i>Lundgren P. et al.</i> .....	21
Monitoring the surface deformation of Mt. Etna with ERS-SAR images <i>Ferretti A. et al.</i> .....	24
Modelling ground deformations in volcanic areas by using SAR interferograms <i>Nunnari G. et al.</i> .....	30
Application of digital elevation model to volcanology <i>Achilli V. et al.</i> .....	36
Analysis of high resolution digital elevation models for morphometric relief classification <i>Baldi P. et al.</i> .....	37
Analysis of lava flows thermal characteristics by using short wave length infrared data acquired by spaceborne and airborne sensors: time series of images acquired on Mt. Etna between 1984 and 2001 <i>Lombardo V., Buongiorno M.F.</i> .....	51
Electromagnetic characterization of volcanic ash <i>Costanzo S., Di Massa G.</i> .....	59
Retrieval of tropospheric ash clouds of mt. etna from AVHRR data <i>Remitti M. et al.</i> .....	64
Estimation of the SO <sub>2</sub> flux of the eruption plume of the Mt. Etna volcano using MIVIS and ASTER data <i>Pugnaghi S. et al.</i> .....	72
Aerosol optical characteristics of volcanic plume retrieval by means of remote sensing techniques: the case of Mt. Etna studied using the MIVIS airborne multispectral image spectrometer <i>Spinetti. C., Buongiorno M.F.</i> .....	81
A tool for spatial data exploitation Vulcano island <i>Baldi P. et al.</i> .....	89



## Preface

This volume of “Quaderni di Geofisica” collects the proceedings of the mid-term meeting of the GNV coordinated project “Development and application of remote sensing methods for the monitoring of active Italian volcanoes” held on 24 and 25 January 2002 at Istituto Nazionale di Geofisica e Vulcanologia in Catania. The project was supported by Dipartimento di Protezione Civile in the frame of the GNV Program 2000-2003.

This research acted as a joint project between Research Institutes and Universities with the aim of improving the application of remote sensing techniques for the study of volcanoes and their activity that, in recent years, had significantly grown thanks to the availability of new sensors and new techniques for data processing. Remote sensing, by its nature, represents an advantageous method to observe, in safety and over large and often inaccessible areas, dangerous natural phenomena such as volcanic eruptions. Various surveying techniques have been experimented using both passive (optical) as well as active (radar) sensors which operate above the scene at high (satellites) and low (planes and helicopters) altitudes. A number of these techniques are very suitable for a systematic surveillance of volcanoes having the capability of detecting phenomena directly or indirectly linked with their dynamics. This applications include the observation of altimetric variations and ground temperature as a consequence of intrusions of magmatic masses, morphological changes caused or induced by eruptive activity, mapping of erupted products spread over the land surface and/or in the atmosphere, and concentration of the some gas (SO<sub>2</sub> and CO<sub>2</sub>) continuously emitted by volcanic plumes. The key point in the application of remote sensing for surveillance of active volcanoes lies in the time required to elaborate and interpret the data acquired by remote sensors. In this project we devised a number of remote sensing methods, among those already experimented by the scientific community, allowing the results to be available in a time span compatible with the requirements for monitoring precursor phenomena and eruptive events. The project described below is developed following five thematic Tasks aimed respectively to: the application of SAR Interferometry to ground deformation studies; the application of DTM to volcanology, the remote sensing of thermal anomalies from active volcanoes, the monitoring of eruptive clouds and the study of volcanic-plume's gas by mean of remote sensing techniques. The activities were performed by 104 scientists and technicians, organized in 15 Research Units from Italy but also France, UK and USA.

I am grateful to all colleagues who provided time and energy in this project, and which exposed their result in the project mid-term meeting: V. Achilli, P. Baldi, S. Borgström, P. Briole, M.F. Buongiorno, S. Costanzo, G. Di Massa, M. Fabris, F. Guglielmino, R. Lanari, V. Lombardo, P. Lundgren, M. Marsella, F. Mazzarini, G. Nunnari, C. Prati, G. Puglisi, S. Pugnaghi.

Special thanks are expressed to the GNV Evaluation Committee: Domenico Giardini of ETH Zurich, Gudmundur Sigvaldasson of NVO Reykjavik, and Marjorie Wilson of Leeds University; to the GNV Director: Paolo Gasparini; and to the INGV President Enzo Boschi, for all their support and valuable contributions to the project direction.

I am appreciate of the help given by INGV Sezione di Catania staff for the organizing of the meeting and, in particular, to Francesco Guglielmino and Maria Marsella for their editorial support and assistance for this volume.

*Mauro Coltelli*  
Project Scientific Coordinator



## Geodetical/SAR monitoring of Campi Flegrei caldera: the 2000 uplift event

Borgström S.<sup>1</sup>, Aquino I.<sup>1</sup>, Berardino P.<sup>2</sup>,  
Del Gaudio C.<sup>1</sup>, De Martino P.<sup>1</sup>, Fornaro G.<sup>2</sup>,  
Galluzzo D.<sup>1</sup>, Guarino S.<sup>2</sup>, Lanari R.<sup>2</sup>, Ricco C.<sup>1</sup>,  
Sansosti E.<sup>2</sup>, Siniscalchi V.<sup>1</sup>, Ricciardi G.P.<sup>1</sup>

<sup>1</sup>Istituto Nazionale di Geofisica e Vulcanologia  
Osservatorio Vesuviano  
Via Diocleziano 328, I-80124 Napoli, Italy

<sup>2</sup>Istituto per il Rilevamento Elettromagnetico  
dell'Ambiente - Consiglio Nazionale delle Ricerche  
Via Diocleziano 328, I-80124 Napoli, Italy

### Abstract

Campi Flegrei is a restless caldera located at the western end of the Bay of Naples (Italy). Besides the geodetic surveillance performed by the I.N.G.V. - Osservatorio Vesuviano via GPS and high precision leveling, a systematic monitoring of Campi Flegrei area has been recently started based on the use of SAR Interferometry (InSAR) techniques.

We present in the following the results achieved by performing a comparative analysis

between geodetic and SAR measurements, in order to investigate the inflation event occurring from early spring to summer 2000. Our goal is to highlight the potential of integrating IFSAR, GPS and leveling data for ground deformation monitoring applications.

### 1. Introduction

Campi Flegrei is a nested caldera which is located at the western end of the Bay of Naples (Italy) and it is the result of two major collapses [Orsi et al., 1996]: the outer rim was formed 37,000 years ago and is related to the Campanian Ignimbrite eruption, whereas the inner caldera was formed 12,000 years ago and is associated with the Neapolitan Yellow Tuff eruption [Di Vito et al., 1999].

The Campi Flegrei magmatic system is still active and has a long deformation history, as testified in the recent past by the bradyseismic crises of 1969-72 (maximum uplift of about 170 cm) and 1982-84 (maximum uplift of about 180 cm) [Orsi et al., 1999]. From January 1985 the area is undergoing a slow but continuous subsidence phase, with small inflation events recorded only in 1989, 1994 and, more recently, in the first months of 2000.

The space-temporal monitoring of ground

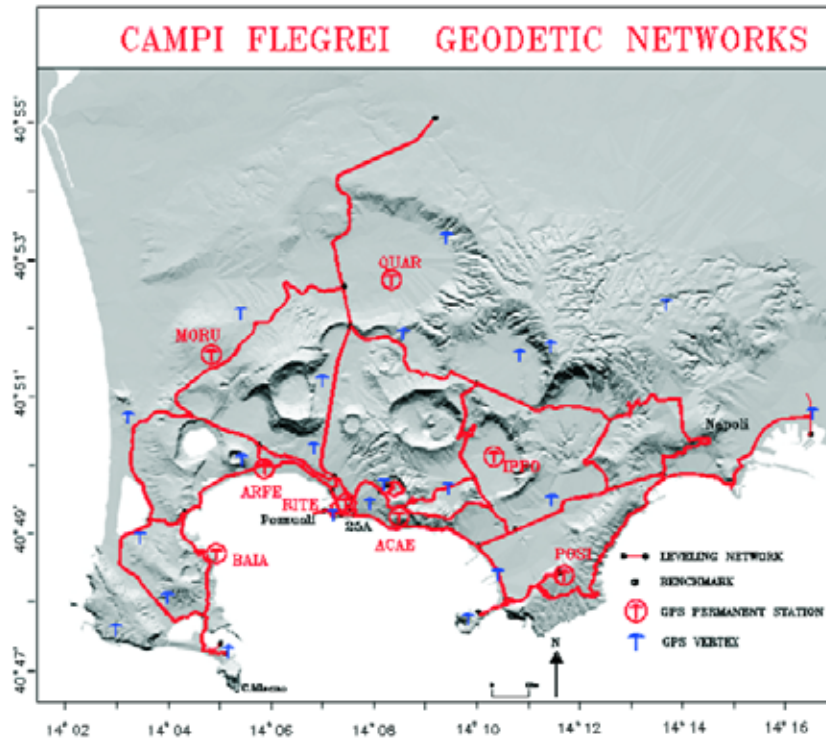


Figure 1 GPS and leveling networks at Campi Flegrei.

deformations in Campi Flegrei area is carried out in a systematic way by the I.N.G.V. - Osservatorio Vesuviano with geodetic surveillance networks operating both continuously and with periodic measurements, whose repetition frequency is a function of the dynamics of the area. At present, the leveling network includes 320 benchmarks on about 120 km of leveling line; moreover, there is also a GPS network of 35 3D vertices (yearly measured), eight of which equipped with continuously recording instruments (fig.1). The geodetic surveillance system is completed by a continuous tiltmetric network, tide gauge and gravimetric networks [I.N.G.V. - Osservatorio Vesuviano Internal Report, 2002].

Such a composite surveillance system may allow a geodetic control with centimetric and/or subcentimetric accuracies but provides an information related to the networks geometry only, thus avoiding to highlight possible migrations of the deformation field outside these ones. Moreover, considering the repeat time of the field measurements, they may be not sensitive to temporal changes in the deformation signal.

Therefore, it is fully understandable the need to thicken the data sampling both in space and in time, in order to guarantee a suitable level of surveillance in a highly populated volcanic area. In this context remote sensing techniques and in particular spaceborne differential SAR interferometry (DInSAR) may provide an important contribution [Gabriel et al., 1989, Massonnet et al., 1993], allowing to carry out spatially dense measurements of the investigated deformation field with, at present, a nearly one month repeat time. In contrast, DInSAR is limited with respect to GPS because it provides only one component of deformation: the displacement component projected into the radar line of sight. This limitation can be greatly relieved by using DInSAR data from more than one satellite track (ascending and descending) such that the two images look from nearly opposite directions and any changes in shape of the deformation reflect differences in the vertical versus horizontal deformation [Lundgren et al., 2001].

Based on the above considerations, it is evident the importance of an effective integration between the information available from geodetic and DInSAR measurements: we present in this work a first attempt to achieve this integration. In particular we focus on the Campi Flegrei uplift phenomenon occurred during 2000, that interrupted the caldera's recent trend

of subsidence. In this case several SAR data sets, acquired by the ERS-2 satellite of the European Space Agency (ESA), were available as well as continuous GPS and leveling measurements. The occurrence of this event during a period of increased geodetic observations allows us to compare these different data sets.

The implications of this integrated approach in civil protection scenarios are also finally addressed.

## **2. The 2000 Inflation Event**

Following the bradyseismic crises of 1969-72 and 1982-84, the Campi Flegrei caldera has been characterized by a slow but continuous subsidence phase, with small inflation events recorded only in 1989, 1994 and, more recently, in the first months of 2000; in particular, the 2000 uplift event was initially pointed out by a clear length variation of some GPS baselines [Achilli et al., 2001]. This episode represents, therefore, an interesting case study for analysing and comparing distinct sets of geodetic and IFSAR data.

### **2.1. GPS data**

As stated before, the GPS data from the continuous stations pointed out relevant changes<sup>1</sup> of the displacement vectors between March and August 2000.

In particular, during this period the 3D vertex located at the Accademia Aeronautica of Pozzuoli (ACAE), near the maximum deformation area, was interested by a planimetric displacement of about 2 cm in the ENE direction, with an uplift of about 4 cm. Also the 3D vertices of BAIA and IPPO (Ippodromo di Agnano) were interested by planimetric displacements.

### **2.2. Leveling data**

As a consequence of the changes recorded by the GPS continuous network, leveling measurements were monthly carried out along the coast line (see fig.1), starting from May 2000. The results from these measurements are shown in fig.3.

They confirmed the deformation phenomenon, highlighting a ground uplift of 3.8 cm in the maximum deformation area (Pozzuoli - C.so Umberto), in the period from September 1999 until August 2000.

However, we must remark that such a value is not representative of the whole defor-

---

<sup>1</sup> Data were processed by Bernese software (vers.4.2) and the GPS network was included in the ITRF'97 reference system.

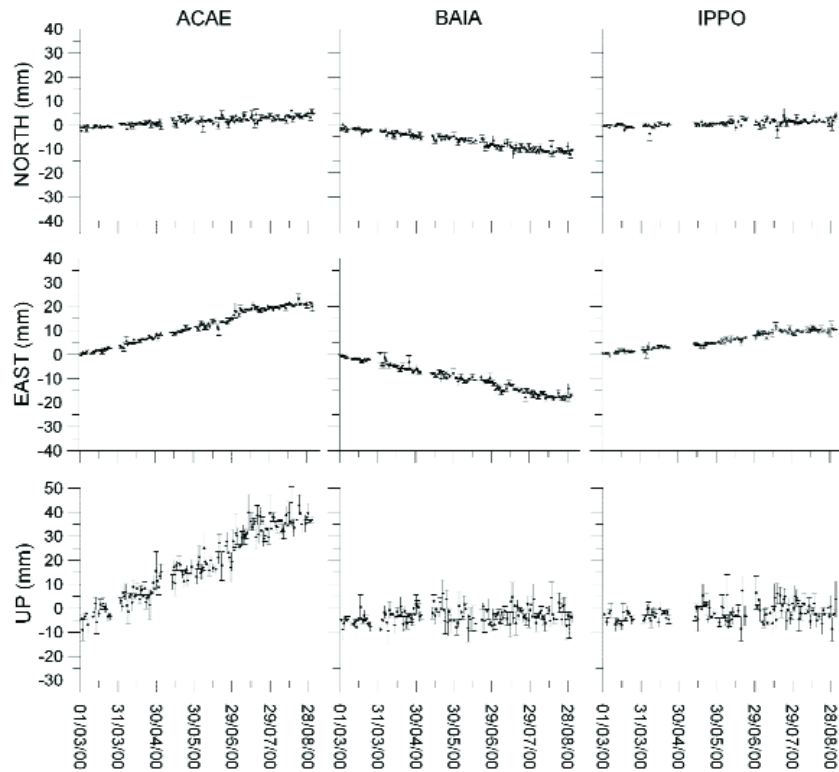


**Figure 2** Time series, between March and August 2000, of daily coordinate variations (in north, east and up directions) and their rms errors for ACAE, BAIA and IPPO stations relative to QUAR (see fig.1 for their location).

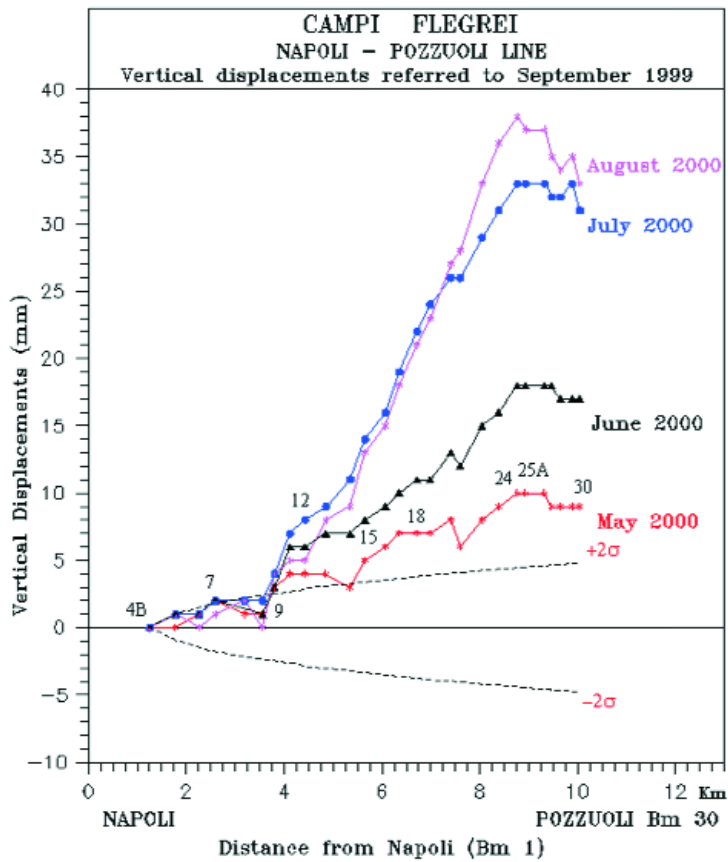


**Figure 3** Vertical displacements from leveling measurements referred to September 1999, coast line (benchmarks 4B to 30, see fig.1); the dashed lines represent the confidence limit at  $2\sigma$  level.

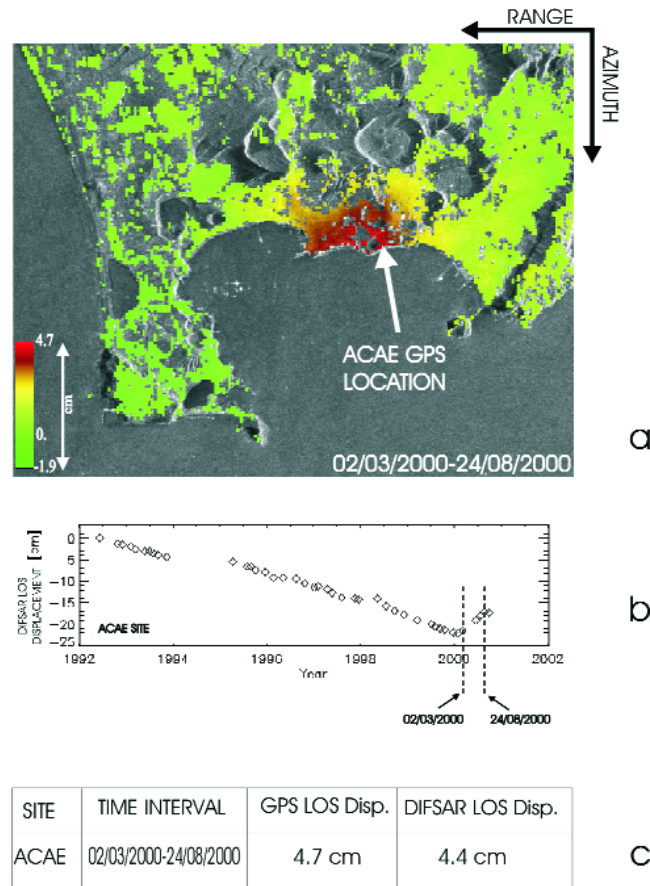


**Figure 4** DInSAR results. (a) Deformation map obtained from the descending ERS-2 acquisitions of March and August 2000. (b) Temporal evolution of the observed DInSAR displacements, in the time interval June 1992-September 2000, for a point close to the location of a GPS station. (c) Comparison of GPS measurements (ACAE site), projected along the radar line of sight (LOS) and DInSAR displacements in the time interval March-August 2000; measurements are referred to the peripheral area of Quarto which is stable.

mation of 2000, as it takes into account also the subsidence still acting during the last months of 1999.

### 2.3. DInSAR data

In order to have a “spatially dense picture” of the phenomenon detected by the geodetic networks, spaceborne IFSAR data, acquired by the ERS-2 sensor, were processed. In particular, the interferometric data processing was carried out by applying the algorithm recently proposed by [Berardino et al., 2001 and 2002] that allows both the production of spatially dense deformation maps and the reconstruction of deformation time-series for each coherent pixel of the imaged scene. We remark that the availability of both spatial and temporal information is crucial to identify and filter atmospheric phase artefacts which could be present in the interferograms [Goldstein, 1995].

The produced deformation map, referred to the period March to August 2000, is shown in

fig.4a and clearly shows a ground deformation pattern of more than 4 cm in Pozzuoli area. We further remark that the considered March/August IFSAR data pair is part of a 44 images data set, available at IREA-CNR, produced by the ERS-1 and ERS-2 systems from descending orbits and spanning the time interval from June 1992 until the end of September 2000. By processing the overall IFSAR data set it is possible to investigate not only the single 2000 event but also the complete temporal evolution of the bradyseismic phenomenon in the period 1992-2000. To clarify this point we plotted in fig.4b the temporal evolution of the deformation for a point close to the AC AE GPS station, located in the maximum deformation area. This plot clearly shows the inversion of the deformation, from subsidence to uplift, after the end of 1999 with a significant inflation from March to August 2000. A comparison between the GPS measurements, projected into the radar line of sight (LOS), and the DInSAR result is

also shown in fig.4c, clearly showing the good agreement between the two measurements.

### 3. Discussion and Conclusions

Ground deformations measurement in Campi Flegrei area represents a key issue for two main reasons: first of all because during inflation events ground deformations precede the renewal of seismic activity, as confirmed also during the 2000 deformation event. In this particular case different seismic events were recorded on July 2<sup>nd</sup> 2000, while ground deformations appear already on March [Osservatorio Vesuviano Internal Report, 2000]. Secondly, these measurements are fundamental for the precise definition of the deformation field acting in the area: the use in the recent past of geodetic techniques such as EDM and nowadays GPS has allowed to point out the presence of an horizontal component of ground motion, supported by a difference in the deformation pattern from ascending and descending interferograms. In this regard, the availability for the next future of a good interferometric data set from both ascending and descending orbits, will be the key point for the understanding of the dynamics acting in the area, besides allowing a source modelling.

Based on the presented geodetic/SAR study, some relevant points can be stressed; first of all we note that the comparative analysis between classical geodetic and DInSAR data shows clear agreement between these observations in both space and time. The main limitations toward achieving the most exacting comparisons were generally due to the poorer temporal sampling of the complete geodetic networks (i.e. leveling and GPS), or the poor spatial coverage of the GPS continuous sites versus the less complete component coverage of the SAR data. Future work in which we will include ascending interferograms should reduce this discrepancy. Moreover, the positive results from a combined monitoring, applying classical and IFSAR techniques during a deformation event in an active volcanic area, should open a new way toward an innovative monitoring methodology and an optimization of the surveillance system; this is obviously a relevant issue in civil protection scenarios.

As a final remark, we want to stress that this integrated geodetic/SAR analysis can be successfully used to investigate other areas; indeed, it has been already applied to study the Vesuvio volcano deformations and also in this case a peculiar deformation pattern was detected

[Lanari et al., 2002].

### Acknowledgments

This work has been partially sponsored by the (Italian) National Group for Volcanology (GNV) and by the Italian Space Agency. The DEM of the area has been provided by the I.G.M. of the Italian Army and the precise ERS-1/ERS-2 satellite orbit state vectors by the Technical University of Delft, The Netherlands.

We also want to thank Paul Lundgren of JPL for intense discussions on the interpretation of the measured deformations, which is matter of a companion paper.

### References

- Achilli, V., Aquino, I., Berardino, P., Borgström, S., Cecere, G., Del Gaudio, C., De Martino, P., Fabris, M., Fusco, A., Galluzzo, D., Lanari, R., Menin, A., Ricciardi, G.P., Ricco, C., Salemi, G., Sansosti, E., Sepe, V., Siniscalchi, V. and Tesauro, M., (2001). Integration of SAR Interferometry with classical geodetic techniques for ground deformation monitoring at the Phlegrean Fields (Naples, Italy). In: Proceedings of the Italy-Canada 2001 Workshop on "3D Digital Imaging and Modeling Applications of: Heritage, Industry, Medicine & Land", 3-4 April 2001, Padua, on CD-ROM.
- Berardino, P., Fornaro, G., Fusco, A., Galluzzo, D., Lanari, R., Sansosti, E. and Usai, S., (2001). A new approach for analyzing the temporal evolution of Earth surface deformations based on the combination of DInSAR interferograms. In: Proceedings IGARSS'2001.
- Berardino, P., Fornaro, G., Fusco, A., Galluzzo, D., Lanari, R., Sansosti, E. and Usai, S., (2002). A new Algorithm for Surface Deformation Monitoring based on Small Baseline Differential SAR Interferograms. accepted for publication on IEEE Transactions on Geoscience and Remote Sensing, 2002.
- I.N.G.V. - Osservatorio Vesuviano Internal Report "Rendiconto sull'attività di sorveglianza - II semestre 2001" (in italian), April 2002.
- Di Vito, M.A., Isaia, R., Orsi, G., Southon, J., de Vita, S., D'Antonio, M., Pappalardo, L., and Piochi, M., (1999). Volcanism and deformation since 12,000 years at the Campi Flegrei caldera (Italy). *J. Volcanol. Geotherm. Res.*, 91, 221-246.
- Gabriel, A., Goldstein R.M., and Zebker, H., (1989).

- Mapping small elevation changes over large areas: Differential radar interferometry. *J. Geophys. Res.*, 94, 9183-9191.
- Goldstein, R.M., (1995). Atmospheric limitations to repeat-track radar interferometry. *Geophys. Res. Lett.*, 22, 2517-2520.
- Lanari, R., De Natale, G., Berardino, P., Sansosti, E., Ricciardi, G.P., Borgström, S., Capuano, P., Pingue, F., and Troise, C., (2002). Evidence for a peculiar style of ground deformation inferred at Vesuvius volcano. in press on *Geophysical Research Letters*.
- Lundgren, P., Usai, S., Sansosti, E., Lanari, R., Tesauro, M., Fornaro, G., and Berardino, P., (2001). Modeling surface deformation observed with synthetic aperture radar interferometry at Campi Flegrei caldera. *J. Geophys. Res.*, 106, 19355-19366.
- Massonnet, D., Rossi, M., Carmona, C., Ardagna, F., Peltzer, G., Feigl, K., and Rabaute, T., (1993). The displacement field of the Landers earthquake mapped by radar interferometry. *Nature*, 364, 138-142.
- Orsi, G., de Vita, S., and Di Vito, M.A., (1996). The restless, resurgent Campi Flegrei nested caldera (Italy): Constraints on its evolution and configuration. *J. Volcanol. Geotherm. Res.*, 74, 179-214.
- Orsi, G., Civetta, L., Del Gaudio, C., de Vita, S., Di Vito, M.A., Isaia, R., Petrazzuoli, S.M., Ricciardi, G.P., and Ricco, C., (1999). Short-term ground deformations and seismicity in the resurgent Campi Flegrei caldera (Italy): an example of active block-resurgence in a densely populated area. *J. Volcanol. Geotherm. Res.*, 91, 415-451.
- Osservatorio Vesuviano Internal Report (July 2000). Crisi bradisismica della Caldera dei Campi Flegrei 2000 (in Italian).

## Application of differential SAR interferometry for studying eruptive event of 22 July 1998 at Mt. Etna

Coltelli M.<sup>1</sup>, Puglisi G.<sup>1</sup>,  
Guglielmino F.<sup>1</sup>, Palano M.<sup>2</sup>

<sup>1</sup>Istituto Nazionale di Geofisica e Vulcanologia, Sezione di Catania, Piazza Roma 2, 95123 Catania

<sup>2</sup>Dipartimento di Scienze Geologiche, Sezione di Geofisica, Università degli studi di Catania, C.so Italia 2, 95129 Catania

### Abstract

One of the main objectives of the project “Development and application of remote sensing methods for the monitoring of active Italian volcanoes” is directed to an operational use of differential interferometry as a tool for volcano monitoring. A first step to achieve this goal is to test commercial software in order to evaluate the most suitable for the project purposes. For testing software, SAR images collected by ERS2 from May 98 to August 98, before and after the strong eruptive event occurred on 22

July 98 at Voragine crater of Etna, have been selected. The explosive event was classified sub-plinian producing a 12 km high eruptive column and lapilli fell on land as far as 70 km south-eastward along the dispersal axis. Pre, post and across event image pairs have been processed. In particular the pair 13 May 98-22 July 98, 22 July 98-26 August 98, 13 May 98-26 August 98 are used for testing respectively pre, post and across event. In first analysis, the fringes in the differential products show a positive elevation trend in the summit area of the volcano. In particular, an increased of about 1,5 fringes in the period pre-event, and a decrement of 1 fringe in the period post-event is observed. This result is agreement with field of deformation expected in such kind of event, confirming that the interferometric processing tool used is suitable for the purpose of the project.

### Introduction

A vigorous explosive eruption was produced by Voragine Crater of Etna on 22 July 1998. A 10 km high eruptive column above the crater rim formed at the eruptive climax between 16.48 and 17.14 GMT (Fig.1) [Aloisi et al., 2002] and the ash cloud expanded radial

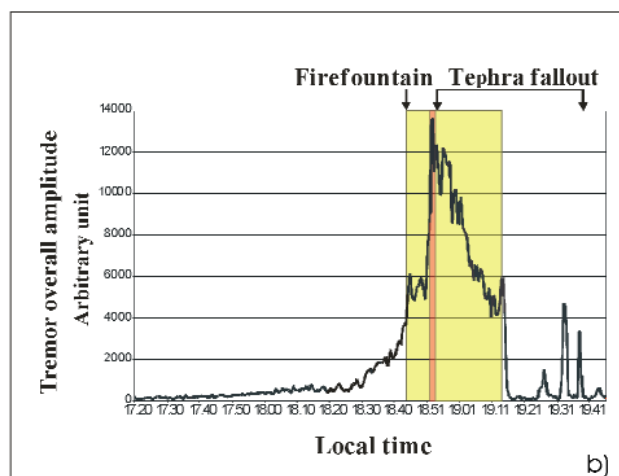


**Figure 1** Photograph of the 22 July 1998 paroxysmal event at Voragine crater, and plot of tremor amplitude.

because of the low speed wind. Lapilli fell as far as 12 km south-eastward along the dispersal axis.

Coarse ash fell in the distal zone after about 2 hours from the beginning of the eruption, in a wide area along the coastline comprises between Giarre to the north and Siracusa at about 100 km from the vent to the south (Fig.2).

The huge quantity of juvenile molten material fallen inside the crater caused its complete filling, followed by a large overflow which formed a 1 km long rootless lava flow running in the valley between NEC and BN.

Fieldwork measurements, grainsize analyses and calculation of the physical parameters allowed to characterize the eruption that result subplinian in magnitude in spite of the low volume of material erupted (about  $1 \times 10^6 \text{ m}^3$  the fallout +  $2 \times 10^6 \text{ m}^3$  the proximal deposit) [Andronico et al., in prep].

### SAR Interferometry Processing

The selection of the images was performed by inspecting the ERS archives with the DESCW software. In table 1 are listed all the image that were scheduled to be acquired over the Etna area. It is noteworthy that the 22 July

98 pass occurred at 21.16, thus few hours after the end of the eruptive event (see Fig.1).

These images were coupled forming the three interferometric pairs (IP1, IP2, IP3) listed in Table 2 with the associated values for the temporal baseline, perpendicular baseline and height of ambiguity. Table1

Pre, post and across event image pairs have been processed. In particular the pair 13 May 98-22 July 98, 22 July 98-26 August 98, 13 May 98-26 August 98 are used for testing respectively pre, post and across event.

The data processing was performed using the Image processing tools developed by Atlantis (EarthView InSar v. 1.2). The procedure used for the generation of interferometric products relevant to the selected image pairs is called two pass interferometry, this approach seeks to exploit all the external information available for a site, in particular, the topography through a digital elevation model.

As source of the topographic information, a photogrammetric DEM, with a measured accuracy in the order of 10 m has been considered.

This philosophy comes into play at four steps of the processing:

1. The two radar images must be coregistered with a precision of a fraction of a pixel. The

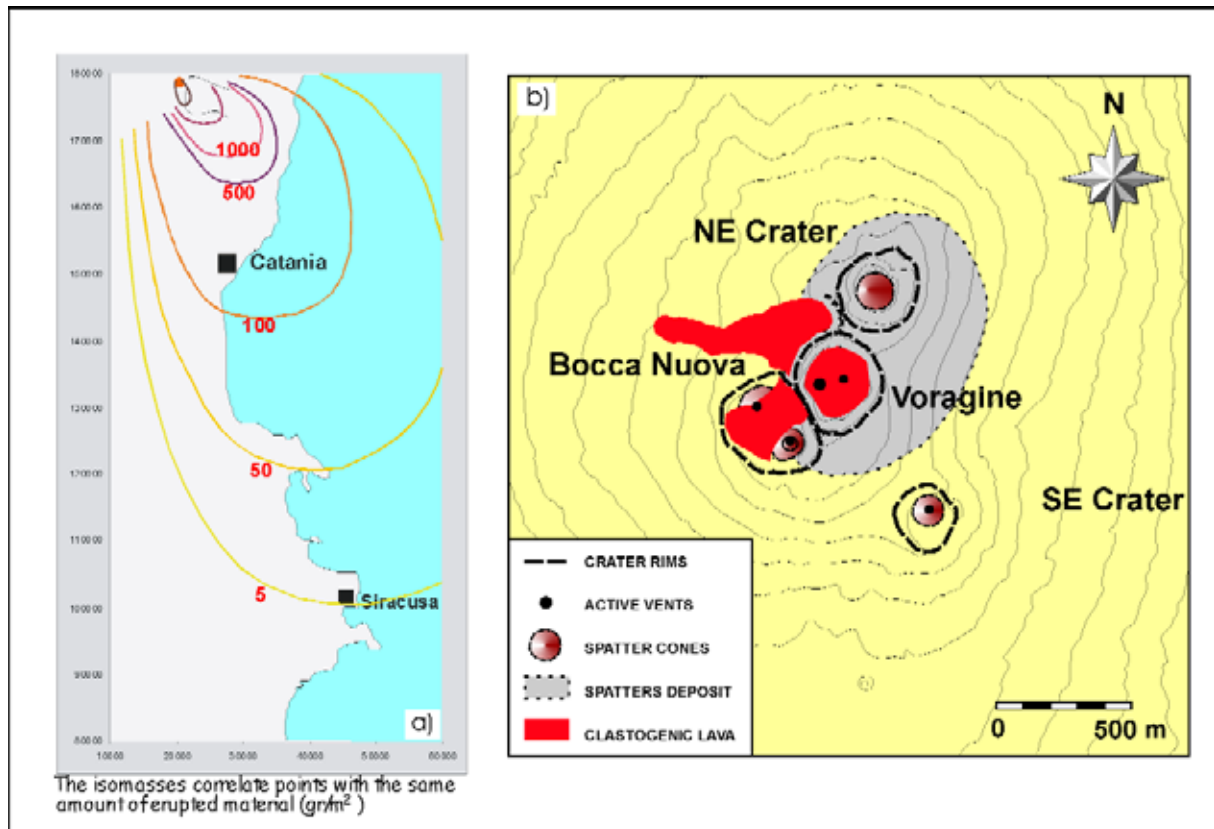


Figure 2 Distal (a) and proximal (b) pyroclastic deposits of the 22 July 1998 eruptive event.

Date of acquisition	13/05/98	22/07/98	26/08/98
Sensor	ERS2	ERS2	ERS2
Orbit	16015	17017	17518
Trak	129	129	129
Frame	747	747	747

**Table 1**

Image Pair	IP1	IP2	IP3
Date	13/05/98-22/07/98	22/07/98-26/08/98	13/05/98-26/08/98
Temporal baseline	70 days	35 days	105 days
Perpendicular Baseline length (m)	-310	78	-232
Height of ambiguity (m/cy)	30	136	38

**Table 2**

- DEM and the orbits predict a deformation grid, which is compared with a sparse grid obtained from local correlations on actual images.
2. One of the radar images must be registered in absolute geographic coordinates. A radar image is simulated whose amplitude depends on the local topographic slope, which is then correlated with the observed image.
  3. the topographic contribution is eliminate by subtracting the fringe pattern calculated from the DEM. The advantage of this approach is that it removes many unwanted fringes, leaving only those related to the signal of interest and/or errors in the DEM .
  4. the interferogram is projected into an orthogonal geographic coordinate system, so that users need not work in the distorted radar geometry. The software developed according to these principles runs automatically in most cases, starting from the SLC radar data and the DEM.

### Comparison of Results and Discussion

A preliminary rough analysis, of the interferograms has been performed. A positive elevation trend in the summit area of the volcano results this analysis. In particular, an increase of about 3 fringes in the period pre-event, a decrement of 1.5 fringe in the short period post-event (Fig.6), and a general uplift in the long period (13/05/98-26/08/98) is observed.

The existence of three GPS benchmarks around the summit crater area, belonging to the Mt. Etna GPS network, permits to consider data for validating the SAR measurements. Unfortunately, these GPS stations were not continuously running at this epoch, because the set up of the permanent GPS network on Mt. Etna was not finished, but the estimation of the strain tensor around the Summit Crater area for a time interval crossing the paroxysmal event it is allowed.

The principal ellipse strain axis, reported in Fig. 7, show an agreement with a strain pat-

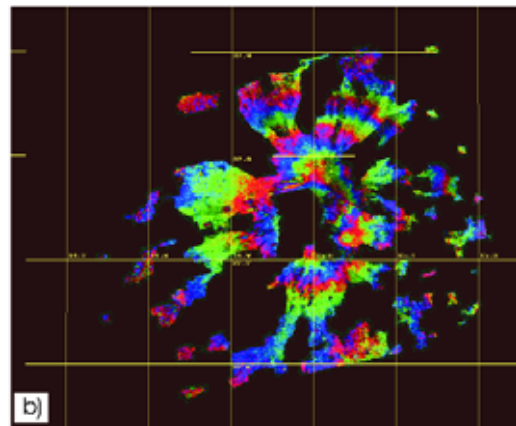
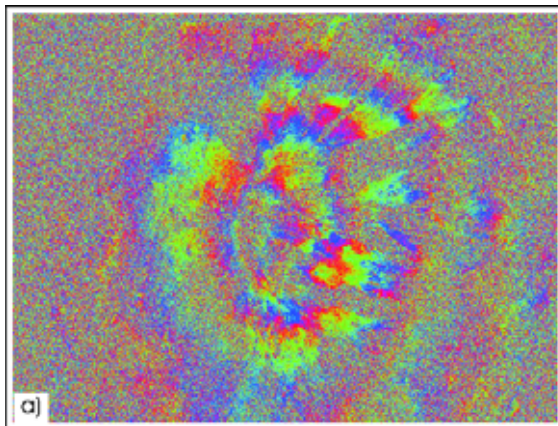


**Figure 3** (a) Interferometric pair 13 May 98-22 July 98; an increase of about 3 fringes in the period pre-event is observed. (b) The interferogram pair georeferenced. In this display the low coherence zone is masked out.

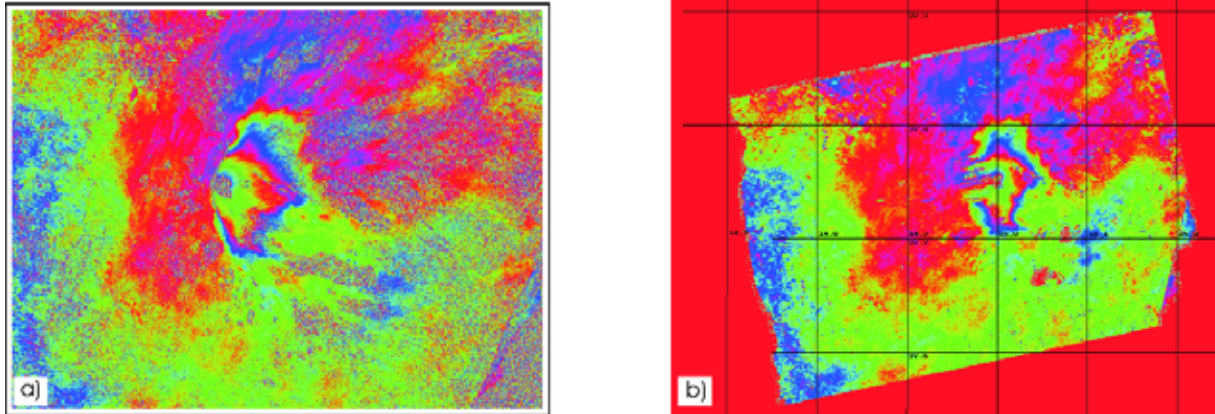


**Figure 4** (a) Interferometric pair 22 July 98-26 August 98; a decrement of 1.5 fringe in the short period post-event is observed. (b) The interferogram pair georeferenced. In this display the low coherence zone is masked out.

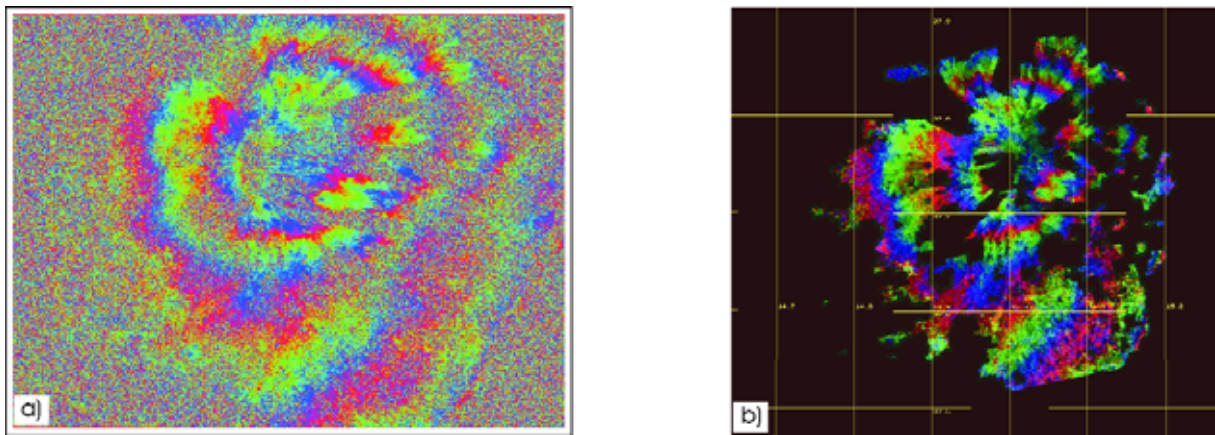


**Figure 5** (a) Interferometric pair 13 May 98-26 August 98; a general uplift in the long period is observed. (b) The interferogram pair georeferenced. In this display the low coherence zone is masked out.

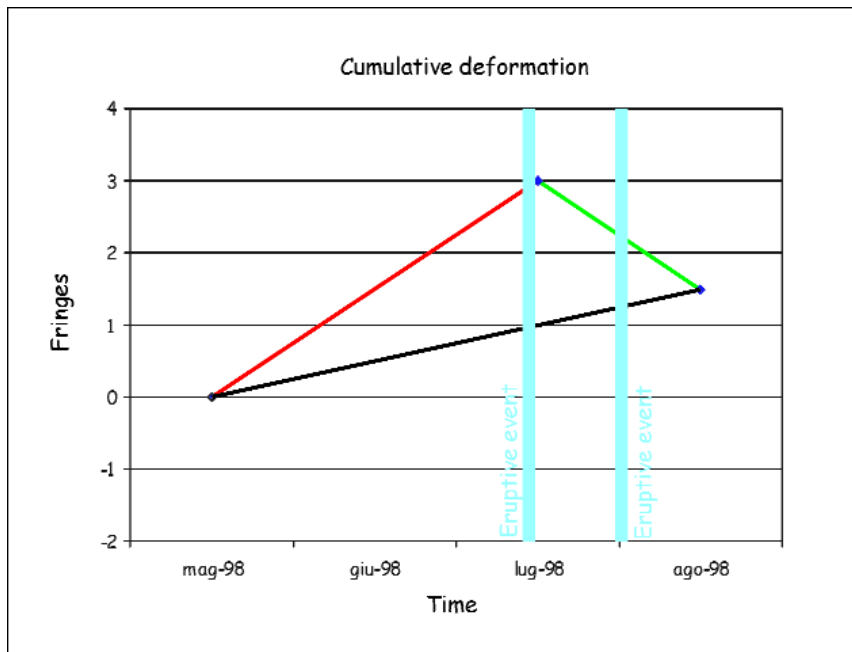


**Figure 6** Cumulative deformation plot.

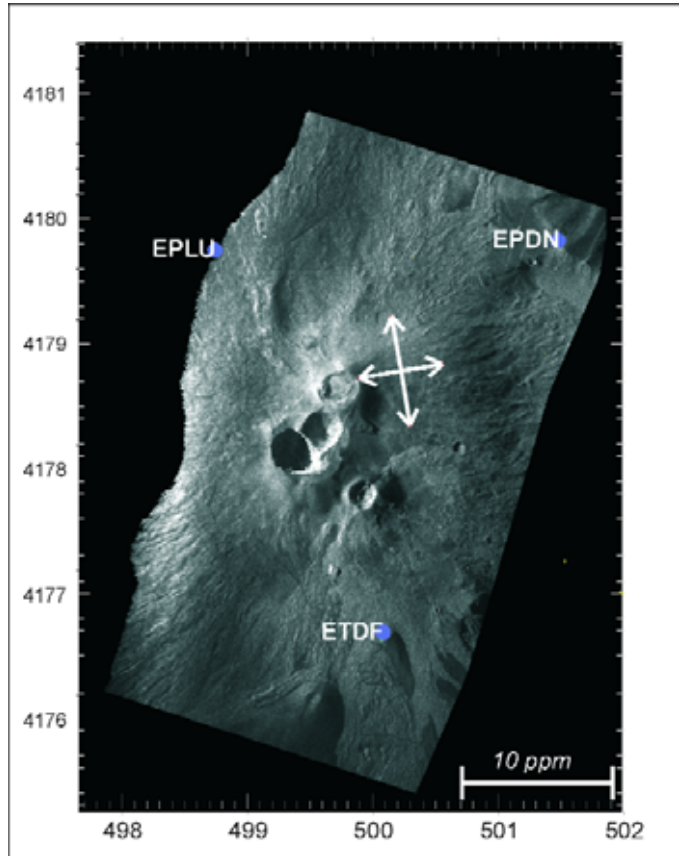


**Figure 7** Ellipse strain axes from GPS data.

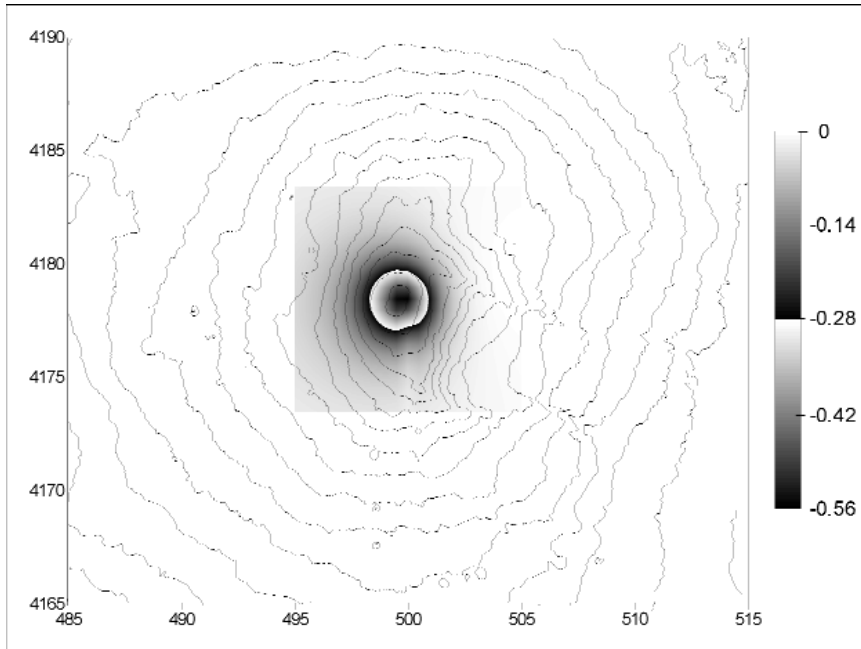


**Figure 8** Synthetic displacement field.

tern produced by an axis-symmetric pressure source, centered beneath the summit craters [Bonaccorso and Davis, 1999].

By assuming the existence of a magmatic source at depth of about 1.5 km from a reference

level located of about 2500 m a.s.l., it is possible to produce the synthetic displacement field reported in Fig. 8.

The corresponding magma withdrawal is estimated in the order of  $0.5 \cdot 10^6 \text{ m}^3$ .

## **Remarks and Plans for Future Works**

- The study the deformation pattern associated to the Mt. Etna paroxysmal event of 22 July 1998, shows a positive elevation trend in the summit area of the volcano. In particular, an increase in the period pre-event, a decrement in the short period post-event, and a general uplift in the long period is observed.
- The computed SAR image for this model reproduces the main characteristic features of real SAR interferogram
- Using an SAR interferogram, is possible to construct detailed models otherwise impossible using only conventional spatially sparse geodetic data
- A method for the non-linear inversion of ground deformation data using Simulated Annealing techniques and SAR images have been proposed (co-operation whit RU-UNICT)

## **References**

- Aloisi, M., D'Agostino, M., Dean, K. G, Mostaccio, A., Neri, G., (2002). Satellite analysis and PUFF simulation of the eruptive cloud generated by the Mount Etna paroxysm of 22 July 1998. *J. Geophys. Res.*, 107(B12) ECV 9/1-ECV 9/12.
- Bonaccorso, A., Davis, M., (1999). Models of ground deformation from vertical volcanic conduits with application to eruptions of Mount. St. Helens and Mount Etna, *J. Geophys. Res.*, 104, 10531-10542.
- Andronico, D. , Coltelli, M., Del Carlo, P. , (in prep). Tephra fallout from the smaller documented Subplinian eruption occurred at Mt. Etna on 22 July 1998.

## Report on observations and modeling of coupled magma chamber inflation and flank motion on Mt. Etna volcano

P. Lundgren<sup>1</sup>, P. Berardino<sup>2</sup>, M. Coltelli<sup>3</sup>,  
G. Fornaro<sup>2</sup>, R. Lanari<sup>2</sup>, G. Puglisi<sup>3</sup>,  
E. Sansosti<sup>2</sup>, and M. Tesauro<sup>2</sup>

<sup>1</sup>Jet Propulsion Laboratory  
California Institute of Technology, Pasadena, CA

<sup>2</sup>IREA – CNR, Napoli, Italy

<sup>3</sup>Istituto Nazionale di Geofisica e Vulcanologia  
Catania, Italy

### Abstract

Volcanoes deform dynamically due to changes in both their magmatic system and due to instability of their edifice. We analyze European Remote Sensing (ERS) satellite differential interferometric synthetic aperture radar (InSAR) data (1993-1996) for Mt. Etna spanning its quiescence from 1993 through the initiation of renewed eruptive activity in late 1995. We use SAR data from both ascending and descending ERS satellite tracks. Comparison of independent interferograms covering the first two years of the inflationary period shows a pattern consistent with inflation of the volcano. Longer term interferograms spanning 1993 to 1999 confirm the inflation pattern from 1993 to 1995 and show that atmospheric effects in many of these interferograms are minimal. Joint inversion of interferograms from ascending and descending satellite tracks require both inflation from a spheroidal magmatic source located beneath the summit at 5 km below sea level, and displacement of the east flank of Etna along a basal decollement. Both sources of deformation were contemporaneous within the resolution of our data and suggest that inflation of the central magma chamber acted to trigger slip of Etna's eastern flank.

Mt. Etna is one of the most studied volcanoes in the world. Its high level of activity and its complex structure make it an important site for studying the effects of volcanic activity on structural instabilities of the volcano. In this report we synthesize results that were initially observed and reported by Lanari et al. [1998] and have been more thoroughly investigated by Lundgren et al. [2002]. We use synthetic aperture radar (SAR) interferometry (InSAR)

[Rosen et al., 2000] to measure surface displacements to an accuracy of a couple of centimeters with a SAR scene that more than covers the entire volcano. This SAR data comes from the European Space Agency's ERS-1 and ERS-2 satellites. InSAR has the capability to observe deformation that is both broad (entire volcano inflation/deflation) and detailed (sub-centimeter radar line of sight displacements along a creeping fault). We will show that in during the period 1993-1995 (and beyond) both inflation of the volcano and motion of the fault-bounded eastern flank of Mt. Etna occurred.

SAR interferometry provides a relative displacement map of the surface as projected into the radar line-of-sight (LOS). This assumes reasonably small orbit separations (order 100 m), good knowledge of the satellite orbits, and a digital elevation model (DEM); factors that can reduce the quality of these displacement maps include decorrelation (due to changes in the radar back scatter) and atmospheric noise [Massonnet et al., 1995; Delacourt et al., 1998; Beauducel et al., 2000; Rosen et al., 2000]. The latter is the most difficult to understand since for a volcano the height of Etna (3300m) with a

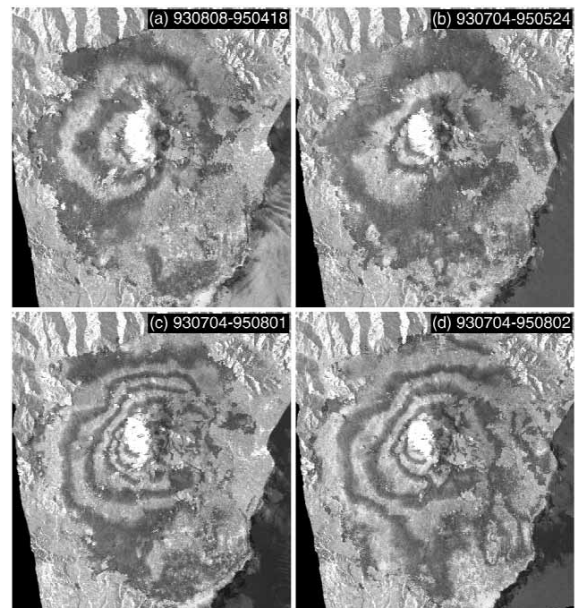


**Figure 1.** Unwrapped, geocoded SAR interferograms for approximately two-year time separations from *ascending* satellite tracks. Color wheel is set to 2.8 cm per cycle of range displacement. Background image is the radar backscatter amplitude image from the reference image. (a) 1993/08/08-1995/04/18 interferogram. (b) 1993/07/04-1995/05/24. (c) 1993/07/04-1995/08/01. (d) 1993/07/04-1995/08/02.

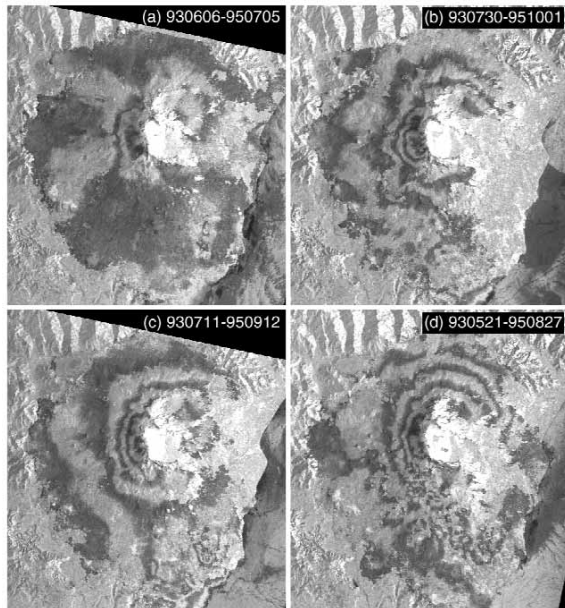


**Figure 2.** Unwrapped, geocoded SAR interferograms for approximately two-year time separations from descending satellite tracks. Color wheel and background image is the same as in Plate 1. (a) 1993/06/06-1995/07/05. (b) 1993/07/30-1995/10/01. (c) 1993/07/11-1995/09/12. (d) 1993/05/21-1995/08/27.

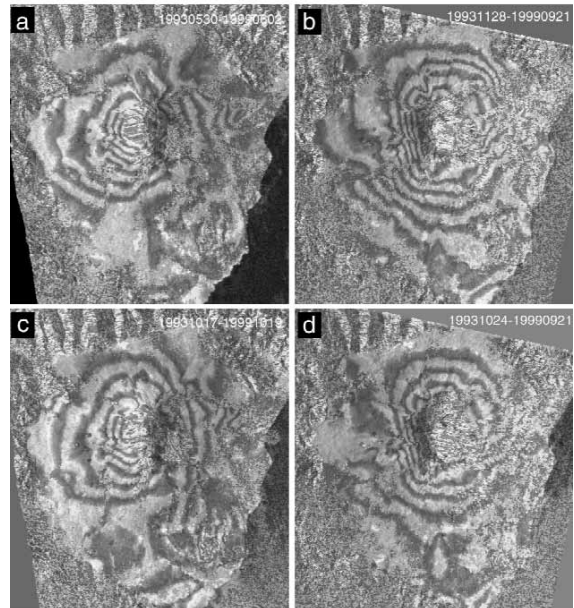


**Figure 3.** Ascending (a, c) and descending (b, d) track InSAR data. Each represent six-year independent interferograms.

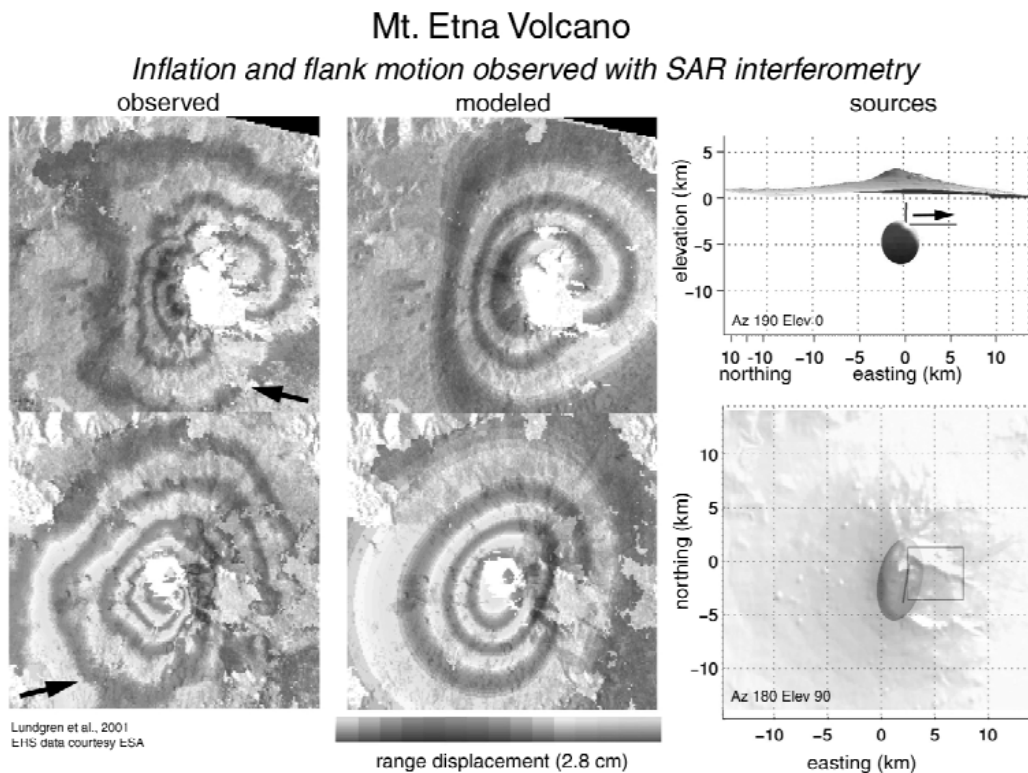


**Figure 4.** Joint inversion results for the topographically corrected elastic half space model. *Left column:* Data. *Top,* descending interferogram range displacements for 1993/06/06-1995/09/12. *Bottom,* ascending interferogram range displacements for 1993/08/08-1995/10/10. (b) Residual. *Central column:* Model. *Right column:* Three-dimensional views of the source model.

concentric shape the radar path delay due to topography in the presence of a layered troposphere and small inflation/deflation patterns due to a point source at several kilometers depth are similar in the vertical component.

Figures 1 and 2 show ascending and descending interferograms for the 1993-1995 time period. Additionally, two more interferograms (one for each ascending and descending satellite track acquisition) are shown in Figure 4. These InSAR data show a similarity between members of each satellite (ascending or descending) track (actually different tracks for the descending group) but a significantly different shape between the two groups. Such a difference would be expected for a pressurized magma chamber source, whereas for a layer atmospheric model the effect would be independent of the azimuthal component of the LOS.

In fact analysis of ERS data spanning from 1993-1999 over independent SAR acquisitions (Figure 3) demonstrates that the differences in the shape of the deformation between the ascending and descending data observed from 1993 to 1995 were dominated by surface deformation and not atmospheric effects. Numerical solutions for a single magmatic pressure source do not adequately fit both the ascending and descending fringe patterns (Figure 4). The answer lies in considering deformation from two dislocations that simulate movement of a portion of the eastern flank of Etna lying above the spheroidal magma chamber centered at 5 km depth. While a more detailed explanation (and justification) for this interpretation can be found in Lundgren et al. [2002], these observations and relatively simple model have several important implications:

Both ascending and descending interferograms are needed to better constrain the source of deformation.

Atmospheric effects are not as big a problem as previously thought (although still poorly defined and requiring redundant InSAR data).

During the 1993 to 1995 period (and beyond) Mt. Etna experienced both inflation and structural motion.

Clearly more data will help us to better understand the connection and dynamics between magma movement and volcano structural instabilities for future hazard mitigation.

## References

- Beauducel, F., P. Briole, and J.-L. Froger, Volcano-wide fringes in ERS synthetic aperture radar interferograms of Etna (1992-1998): Deformation or tropospheric effect?, *J. Geophys. Res.*, *105*, 16,391-16,402, 2000.
- Delacourt, C., P. Briole, and J. Achache, Tropospheric corrections of SAR interferograms with strong topography. Application to Etna, *Geophys. Res. Lett.*, *25*, 2849-2852, 1998.
- Lanari, R., P. Lundgren, and E. Sansosti, Dynamic deformation of Etna volcano observed by satellite radar interferometry, *Geophys. Res. Lett.*, *25*, 1541-1544, 1998.
- Lundgren, P., P. Berardino, M. Coltelli, G. Fornaro, R. Lanari, G. Puglisi, E. Sansosti, and M. Tesauro, Coupled magma chamber inflation and sector collapse slip observed with SAR interferometry on Mt. Etna volcano, *J. Geophys. Res.*, in revision, 2002.
- Massonnet, D., P. Briole, and A. Arnaud, Deflation of Mount Etna monitored by spaceborne radar interferometry, *Nature*, *375*, 567-570, 1995.
- Rosen, P. A., S. Hensley, I. R. Joughin, F. K. Li, S. N. Madsen, E. Rodriguez, and R. M. Goldstein, Synthetic aperture radar interferometry, *Proc. IEEE*, *88*, 333-382, 2000.

## Monitoring the surface deformation of Mt. Etna with ERS-SAR images

Ferretti A.<sup>2</sup>, Colombo D.<sup>2</sup>, Savio G.<sup>2</sup>,  
Prati C.<sup>1</sup>, Rocca F.<sup>1</sup>

<sup>1</sup>DEI - Politecnico di Milano  
Piazza L. da Vinci 32 – www.polimi.it

<sup>2</sup>Telerilevamento Europa (T.R.E.) S.r.l  
Via V. Colonna 7 – Milano – www.treuropa.com

### Abstract

The main goal of this paper is to show how satellite SAR data can be exploited to get surface deformation measurements of an active volcano like Mt. Etna. In particular it is shown that small baseline SAR interferograms are suitable for an accurate imaging of ground deformations with mainly continuous patterns in space. The Mt. Etna deformation occurred during the eruptive event of the July 2001 is shown as a nice and interesting result of this technique applied to ERS-2 data. However, whenever small ground deformations are limited to isolated points or concentrated across lines (e.g. active faults) a more sophisticated analysis should be carried out by means of the Permanent Scatterers (PS) technique. The slip of the eastern flank of Mt. Etna observed by ERS-1 and ERS-2 satellites in 40 repeated passes from 1995 to 2000, is used to show the PS technique potential.

### 1. Introduction

Differential SAR interferometry (DINSAR) has been widely and successfully used during the last 10 years for monitoring land motion of large areas with centimetric accuracy [Massonnet et al. 1995] [Hanssen 2000]. Most of the results have been achieved thanks to the impressive amount of SAR images provided by the two ESA satellites ERS-1 (1991-2000) and ERS-2 (since 1995). The precise orbit and attitude control of ERS-1 and ERS-2 are at the basis of the successful generation of thousands of interferograms and land motion maps.

At the beginning of 2001, ERS-2 platform attitude control had problems. As a consequence, the generation of SAR interferograms became impossible. A back-up attitude control system has been then activated and tuned by the ESA-ESRIN and ESOC staff, and in June 2001,

the interferometric capability of ERS-2 (in gyro-less mode) has been practically recovered.

The first ERS-2 SAR interferometric test in gyro-less mode has been carried out at Polimi in cooperation with T.R.E. on Mt. Etna using 3 images taken in June, July and August 2001. Notwithstanding the residual attitude problems, clear (and impressive) surface deformation maps of the Etna volcano connected to the eruptive event of the July 2001 have been determined. The achieved results are presented in the next section. They clearly show the capability of DINSAR to monitor extended ground deformation when the following requirements are met:

- (i) ground and orbital conditions allow high coherence on wide areas;
- (ii) the interferometric signal due to the ground deformation is much larger than that due to atmospheric changes.

In 1999, to overcome these limiting factors of DINSAR (lack of spatially extended coherence and atmospheric artifacts), an alternative processing of SAR images, the Permanent Scatterers Technique (PST), has been developed, tested and validated at Polimi. The theoretical principle behind the PST will be briefly summarized in the third section without entering the technical details that can be found in [Ferretti et al. 2000] [Ferretti et al. 2001]. In the framework of the GNV project on the “DEVELOPMENT AND APPLICATION OF REMOTE SENSING METHODS FOR THE MONITORING OF ACTIVE ITALIAN VOLCANOES”, the PST has been used to measure the average Line Of Sight (LOS) ground deformation that affected the eastern flank of Mt. Etna in the 5 years period from 1995 to 2000. The results achieved along two N-S sections crossing the eastern flank of Mt. Etna are analyzed in the third section.

### 2. Etna Deformation occurred during the July 2001 Eruption

Two SAR images obtained from the ERS-2 acquisitions in gyro-less mode on 11 July - 15 August 2001 over the Mt. Etna have been used to get a differential interferogram across the eruptive event of July 2001.

The following digital signal processing steps have been carried out:

- 1 Precise estimation of the attitude of the satellite (Doppler centroid) for each image and phase preserving focusing.
- 2 Common band filtering both in azimuth and slant range [Gatelli et al. 1994].

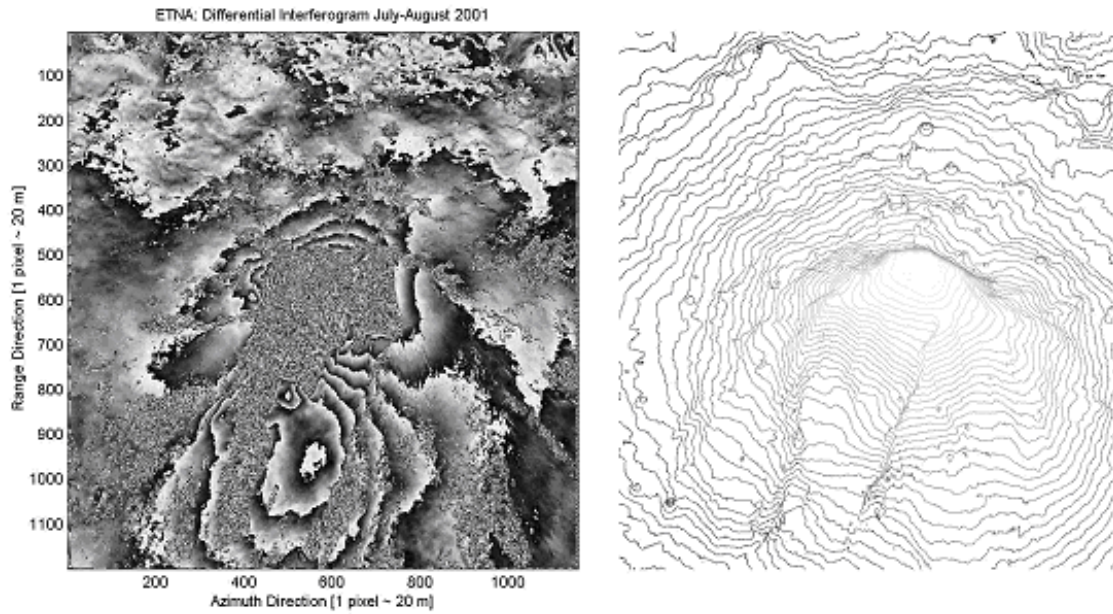


**Figure 1** Left: differential interferogram generated with the two ERS-2 SAR images taken on July 11 and August 15, 2001 (SAR coordinates: range, azimuth). A deformation fringe pattern is clearly visible close to the main faults that cross Mt. Etna and on the Valle del Bove (lower part of the map). Each fringe corresponds to a ground displacement of 2.8cm along the SAR LOS (about 23 deg. off-nadir). Right: Contour lines of Mt. Etna DEM (SAR coordinates).

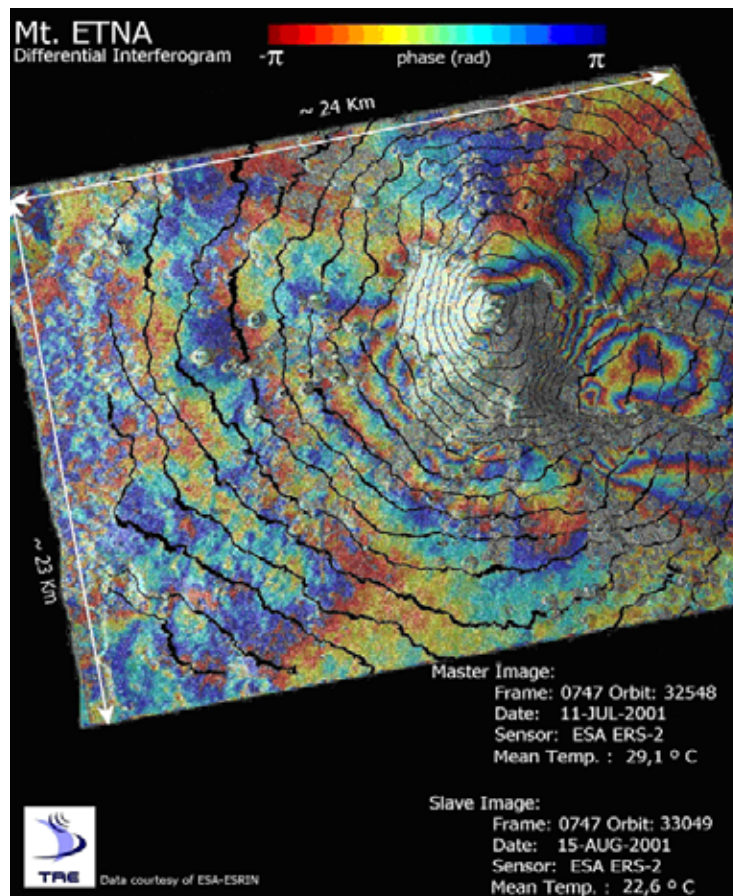


**Figure 2** Geocoded differential interferogram generated with the two ERS-2 SAR images taken on July 11 and August 15, 2001. Each fringe corresponds to a ground displacement of 2.8cm along the SAR LOS (about 23 deg. off-nadir). The contour lines of Mt. Etna DEM are shown in black.

- 3 Sub-pixel registration of the images.
- 4 Generation of differential interferograms using an available Digital Elevation Model (vertical accuracy better than 7m.- courtesy of Institut de Physique du Globe de Paris).
- 5 Compensation of different atmospheric profiles with the elevation. Local measurements of pressure, temperature and humidity have been exploited for this sake [Bonforte et al. 2001].
- 6 Data geocoding.

The differential interferogram is shown in figure 1. Here, a deformation fringe pattern is clearly visible close to the main faults that cross Mt. Etna (including the Pernicana fault that is one of the sites to be monitored in the framework of the GNV project). Each fringe corresponds to a ground displacement of 2.8cm along the SAR Line Of Sight (about 23 deg. off-nadir).

The deformation map generated with these ERS-2 SAR images have been then geocoded in order to facilitate its geophysical interpretation and a comparison with independent ground measurements carried out by the volcanologists of the INGV in Catania. The geocoded

differential interferogram is shown in figure 2.

### 3. The Average Velocity of the Mt. Etna Eastern Flank measured with the PST

The ground deformation analysis carried out by means of the Permanent Scatterers Technique (PST) is conceptually different from that carried out by means of DINSAR and offers many advantages that will be briefly discussed here.

The very basic PST principle can be summarized as follows where ERS, ENVISAT or RADARSAT missions are considered as data sources:

- 1 Isolated targets that maintain their coherence during the monitoring time interval (Permanent Scatterers) can be identified from a statistical analysis of at least 15 complex SAR images. The requested baseline limit is 15 to 20 times greater than for DINSAR, thus making all the archived SAR images exploitable and minimizing the monitoring sampling interval. Moreover, coher-

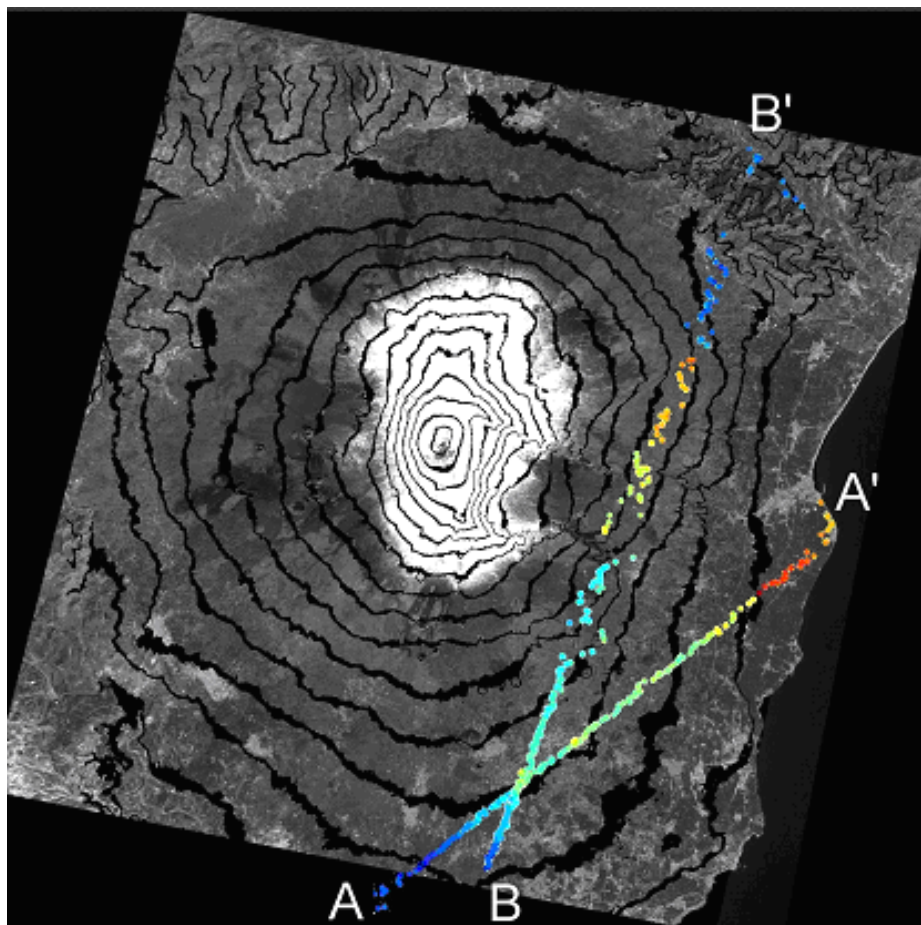


**Figure 3** Profiles AA' and BB' crossing the eastern flank of Mt. Etna from South to North along which the average PS velocity has been computed.

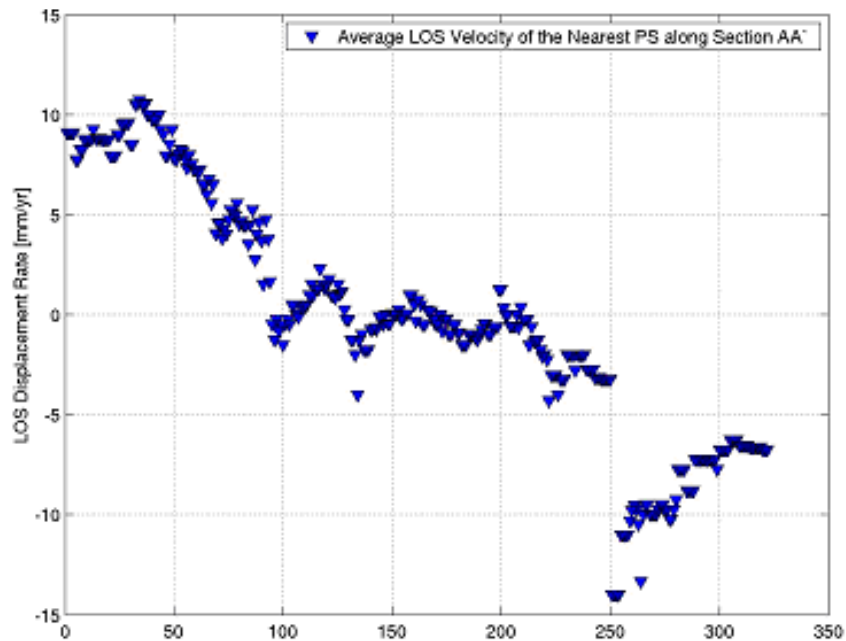


**Figure 4** Average LOS PS velocities along the profile AA'. The dispersion of LOS velocities is in the order of 1 mm/year; no averaging of neighboring PS has been carried out. The effects of the non uniform distribution of the PS along the transept contribute to the residual dispersion. Rapid ground velocity variations identify several active faults.

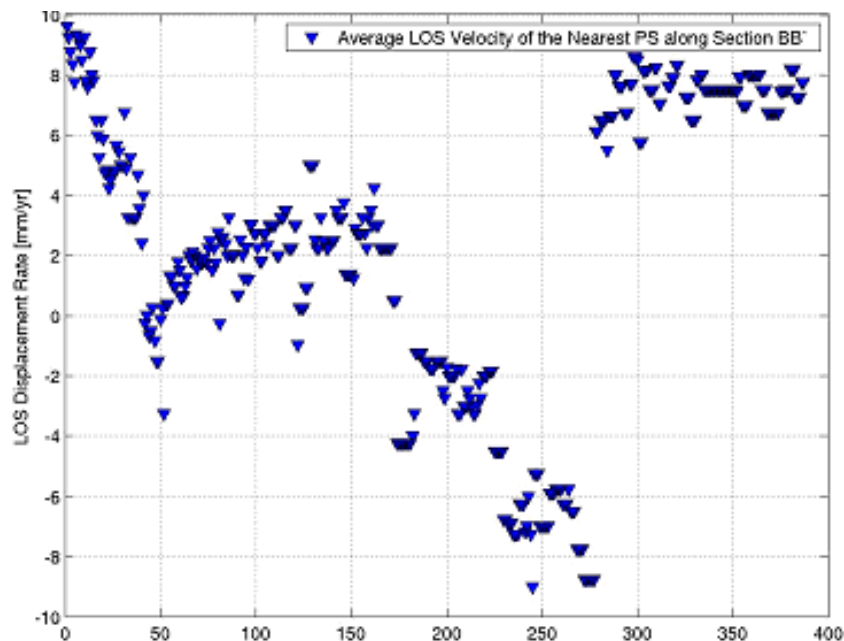


**Figure 5** Average LOS PS velocities along the profile BB'. The large ground velocity variation on the right part of the profile corresponds to the slipping of the Pernicana fault. The dispersion of LOS velocities along the profile BB' looks higher than in profile AA'. This is just a visual impression connected to the position of the PS as clearly shown in figure 3; again, no averaging of neighboring PS has been carried out.

ence estimation is done in time with no need of spatial averaging as for DINSAR, thus making possible the identification of isolated coherent targets that would result invisible to

DINSAR analysis.

- 2 The relative elevation of the PSs can be measured with accuracy better than 1 meter thanks to the large baseline dispersion. As a

consequence no reference DEM is needed.

- 3 Finally, isolated target motion and atmospheric artifacts can be separated by means of a joint space-time data analysis.

The PST has been used to monitor Mt. Etna deformations during the 5 years period of relative low volcanic activity from April 1995 to December 2000. 40 ERS images have been used with normal baselines ranging from -1056 to +1109 meters with respect to the reference orbit. The quality of the information of this data set is shown in the following examples. In figure 3 two profiles AA' and BB' crossing the eastern flank of Mt. Etna from South to North are shown. Figures 4 and 5 show the average Line of Sight velocity of more than 300 PS identified along the two profiles AA' and BB'. The accuracy of the velocity values (computed independently one from the other) can be appreciated from these plots where the vertical scale is expressed in millimeters per year. From a geophysical point of view, these plots clearly show the presence of many active faults splitting the Etna eastern flank in blocks with different slipping velocities. The PS results are currently object of analysis by volcanologists in Catania (GNV) and Paris (IPGP).

## Conclusions

Despite its potentialities, conventional Differential SAR Interferometry (DINSAR) analysis is not the solution for a routine monitoring of surface deformation phenomena by means of satellite repeat-pass observations. Atmospheric effects and phase decorrelation strongly limit the use of this technology as a standard geodetic tool. Whenever the SNR is not very high (as in co-seismic displacement fields and ground deformations due to eruptions) only in a multi-image framework it is possible to separate motion components from clutter and noise and to identify radar targets where reliable displacement information can be recovered.

To this end, the ESA-ERS archive represents a unique dataset to study slow geophysical phenomena and to test different multi-temporal data analysis algorithms. This archive is still underused and its value underestimated by the scientific community. We think that all attempts to extract information from this huge dataset should be fostered and promoted. The ESA acquisition policy chosen for the ERS mission was a success: building a consistent and coherent archive will be in the future a "must" for any

SAR mission dedicated to Civil Protection and monitoring applications. In order to pass from an academic research activity to an operational tool for ground deformation monitoring, any DINSAR analysis should deal with two essential issues: (a) high precision and reliability of the measurements: the processing chain should permit a reliable error analysis, also from a mathematical point of view (robust theoretical framework); (b) high data geocoding precision. The first point implies that final users should be provided with data as well as quality controls. The second point addresses the importance of the integration of EO data in GIS packages, now becoming a standard working tool for many user groups.

The necessity to deal with SAR data characterized by lower stability platforms pushed toward the development of new processing strategies that significantly improved the quality of the results both for standard DINSAR analyses and the PS approach.

It seems indeed that, in the future, interferometric data (ERS-2, ENVISAT, RADARSAT and ALOS) will play a key-role for geodetic measurements and will become a standard tool for monitoring the 3 components of the surface motion. In fact, all three components of the motion are measurable (and not only LOS data) if 230 and 450 ascending and descending orbit data are available. For absolute motion measurements, synergistic strategies with GPS and GALILEO data can be easily envisaged and are likely to be applied in many fields. Hopefully, volcanologists, geophysicists as well as Civil Protection authorities will be provided with powerful Decision Support Systems that will help in identifying the best actions to be undertaken.

## References

- Ferretti A., Prati C. and Rocca F.,(2001). Permanent Scatterers in SAR Interferometry. IEEE Trans. on Geoscience and Remote Sensing 39(1):8-20, January 2001.
- Ferretti A., Prati C. and Rocca F.,(2000). Non-linear Subsidence Rate Estimation Using Permanent Scatterers in Differential SAR Interferometry. IEEE Trans. on Geoscience and Remote Sensing, Vol. 38, no. 5, September 2000.
- Bonforte A., Ferretti A., Prati C., Puglisi G. and Rocca F.,(2001). Calibration of Atmospheric Effects in SAR Interferometry by GPS and local atmosphere models: first results.

Journal of Atmospheric and Terrestrial  
Physics, 63, 1343-1357.

Massonnet D., Briole P., Arnaud A., (1995).  
Deflation of Mount Etna monitored by spaceborne radar interferometry. *Nature*, 375,  
567-570.

Ramon F Hanssen,(2001). *Radar Interferometry:  
Data Interpretation and Error Analysis.*  
Kluwer Academic Publishers, Dordrecht,  
2001.

## **Modelling ground deformations in volcanic areas by using SAR interferograms**

G. Nunnari<sup>1</sup>, G. Puglisi<sup>2</sup>,  
F. Guglielmino<sup>2</sup>, M. Coltelli<sup>2</sup>

<sup>1</sup>Dipartimento di Ingegneria Elettrica, Elettronica e dei Sistemi  
Università di Catania (Italy)  
Viale A. Doria, 6, 95125 – Catania, Italy,  
Tel. +39 095 7382306, e-mail:gnunnari@dees.unict.it

<sup>2</sup>Istituto Nazionale di Geofisica e Vulcanologia,  
Sezione di Catania  
Piazza Roma, 3, 95122 – Catania, Italy  
Tel. +39 095 716581, e-mail:puglisi-g@ct.ingv.it

### **Abstract**

The inversion problem dealt with is the identification of the parameters of a magma-filled dike which causes observable changes in ground deformation data. It is supposed that ground deformation data are measured by using the SAR (Synthetic Aperture Radar) Interferometry technique. The inversion approach, which is carried out by a systematic search technique based on the Simulated Annealing (SA) optimization algorithm, guarantees a high degree of accuracy. The results given in the paper are supported by experiments carried out using an interactive software tool developed ad hoc, which allows both direct and inverse modeling of SAR interferometric data related to the opening of a crack at the beginning and throughout a volcanic activity episode.

### **Introduction**

SAR interferometry is currently one of the most powerful techniques for observation of the earth's surface in particular for topographical measurement of vast geographical areas [Massonnet and Ribaute, 1993], [Gabriel et. al, 1989],[Curlander and McDonough, 1991], [McCloy, 1995] and small surface changes of a surface over a pre-defined time interval (Differential Radar Interferometry). SAR systems record both amplitude and phase of the back scattered radar echoes. If two SAR images from slightly different viewing angles are considered (interferometric pair) their difference (interferometric fringes) can be usefully exploited to generate Digital Elevation Maps (DEMs), measuring shifts in tectonic plates, movement of glaciers and so on. Recently SAR interferome-

try was considered also to monitor ground deformation in volcanic active areas [Coltelli et al., 1996], [Lanari et al., 1996], [Briole et al., 1999] SAR interferometry allows to integrate the techniques traditionally considered to measure ground deformations in volcanic areas such as EDM (Electronic Distance Measuring) or GPS (Global Positioning System) techniques.

The inversion problem considered in this paper consists of identifying the geometric and cinematic parameters of a magma-filled dike, which will be indicated as the source, by observing the changes it causes in SAR interferometric images. Analysis of the mathematical model conceived by Okada [Okada, 1985] show that the inversion problem is an extremely nonlinear one. Hence the inversion solution cannot be obtained only in terms of optimisation approaches. In this paper it is shown that in spite of the high degree of non-linearity the inverse problem can be unambiguously solved and an appreciable degree of accuracy can be obtained by using a randomised optimisation algorithms such the Simulated Annealing (SA) algorithm.

### **Direct Modelling**

#### **Generation of SAR synthetic data**

The model refers to Mt. Etna volcano (Sicily – Italy), where a number of eruptions have been originated by dikes opening from a certain depth toward the surface. These phenomena are accompanied by ground deformations and anomalies in the magnetic and gravity fields. The considered geophysical phenomena may be observed when a crack opens up due to the intrusion of magma. Compared to the real situation, the Okada source model, subsequently described, is of course greatly simplified.

#### **The Okada model**

This model gives the analytical expression of the surface displacements, strains and tilts due to inclined shear and tensile faults in a half-space. In this section, only the tensile components of the deformations are given, in order to illustrate the level of complexity of the direct model.

Let  $O(X,Y,Z)$  be a Cartesian coordinate system representing the traditional UTM system where  $X$  and  $Y$  represent the East and North directions respectively, while  $Z$  represents the vertical direction. Let us consider a dislocation according to the Okada model, having the geometric parameters represented in Fig. 1 whose symbols are described in Tab. I.

Variable	Symbol	Units of Measure	Ranges
Strike	$\sigma$	Degrees	[0,360]
Dip	$\delta$	Degrees	[0,90]
Length	L	Meters	[1000,7000]
Width	W	Meters	[1000,5000]
Opening	U3	Meters	[1,5]
Longitude	Xb	Meters	[-10000,10000]
Latitude	Yb	Meters	[-10000,10000]
Depth	Zb	Meters	[-1000,-7000]

**Table I** Variables, related symbols, unit of measures and ranges considered for the simulation experiments carried out in this paper.

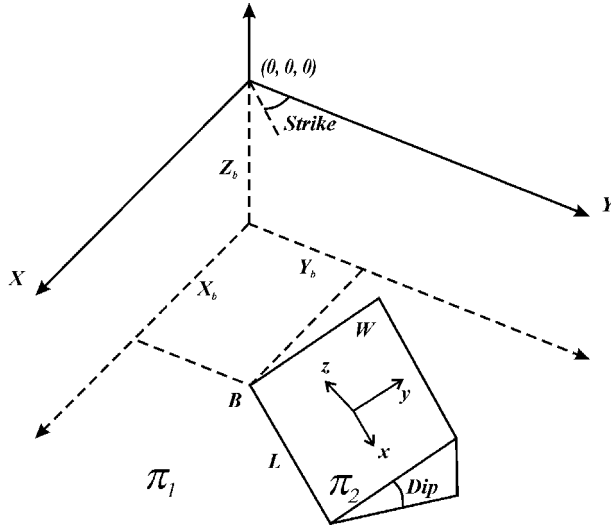


**Figure 1** The Okada dislocation Model.

The point B, having coordinates  $(X_B, Y_B, Z_B)$ , lies on the plane  $\pi_1$ , parallel to the plane XY. The side L (Length) of dislocation is supposed to lay on the  $\pi_1$  plane being the point B one of its vertices, while the side W (Width) is a segment laying on the plane  $\pi_2$ , inclined by an angle referred as Dip with respect to  $\pi_1$  and orthogonal to L.

Moreover, let us consider a further reference system  $o(x,y,z)$  having the x, y axis on the  $\pi_2$  plane and the z axes orthogonal to  $\pi_2$ . In this reference system, x is parallel to L, while y is parallel to W.

The components of the movement caused by a tensile dislocation (tensile fault) relative to a generic point on the plane XY referred to the  $o(x,y,z)$  system were obtained by Okada, are represented by the following relations (see also Fig. 2).

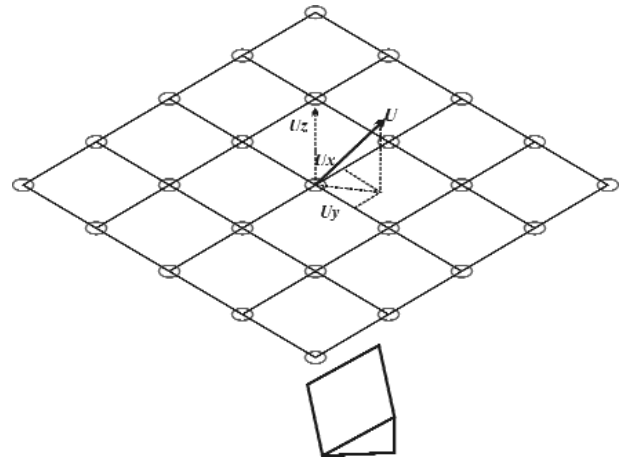


**Figure 2** The deformation vector U and its components

$$\begin{cases} u_x = \frac{U_3}{2\pi} \left[ \frac{q^2}{R(R+\eta)} - I_3 \sin^2 \delta \right] \\ u_y = \frac{U_3}{2\pi} \left[ \frac{-\tilde{d}q}{R(R+\xi)} - \sin \delta \left\{ \frac{\xi q}{R(R+\eta)} - \tan^{-1} \frac{\xi \eta}{qR} \right\} - I_1 \sin^2 \delta \right] \\ u_z = \frac{U_3}{2\pi} \left[ \frac{\tilde{y}q}{R(R+\xi)} + \cos \delta \left\{ \frac{\xi q}{R(R+\eta)} - \tan^{-1} \frac{\xi \eta}{qR} \right\} - I_3 \sin^2 \delta \right] \end{cases}$$

where

$$\begin{cases} p = y \cos \delta + d \sin \delta \\ q = y \sin \delta - d \cos \delta \\ \tilde{y} = \eta \cos \delta + q \sin \delta \\ \tilde{d} = \eta \sin \delta - q \cos \delta \\ R^2 = \xi^2 + \eta^2 + q^2 = \xi^2 + \tilde{y}^2 + \tilde{d}^2 \\ X^2 = \xi^2 + q^2 \end{cases}$$

being

$$\begin{cases} I_1 = \frac{\mu}{\lambda + \mu} \left[ \frac{-1}{\cos \delta} \frac{\xi}{R + \tilde{d}} \right] - \frac{\sin \delta}{\cos \delta} I_5 \\ I_2 = \frac{\mu}{\lambda + \mu} [-\ln(R + \eta)] - I_3 \\ I_3 = \frac{\mu}{\lambda + \mu} \left[ \frac{1}{\cos \delta} \frac{\tilde{y}}{R + \tilde{d}} - \ln(R + \eta) \right] + \frac{\sin \delta}{\cos \delta} I_4 \\ I_4 = \frac{\mu}{\lambda + \mu} \frac{1}{\cos \delta} \left[ \ln(R + \tilde{d}) - \ln(R + \eta) \sin \delta \right] \\ I_5 = \frac{\mu}{\lambda + \mu} \frac{2}{\cos \delta} \tan^{-1} \frac{\eta(X + q \cos \delta) + X(R + X) \sin \delta}{\xi(R + X) \cos \delta} \end{cases}$$

if  $\cos \delta \neq 0$ , and

$$\begin{cases} I_1 = -\frac{\mu}{2(\lambda + \mu)} \frac{\xi q}{(R + \tilde{d})} \\ I_3 = \frac{\mu}{2(\lambda + \mu)} \left[ \frac{\eta}{R + \tilde{d}} + \frac{\tilde{y} q}{(R + \tilde{d})} - \ln(R + \eta) \right] \\ I_4 = -\frac{\mu}{\lambda + \mu} \frac{q}{R + \tilde{d}} \\ I_5 = -\frac{\mu}{\lambda + \mu} \frac{\xi \sin \delta}{R + \tilde{d}} \end{cases}$$

if  $\cos \delta = 0$ .

In these equations,  $(x, y, z)$  and  $(\xi, \eta, q)$  are coordinates of appropriate reference systems;  $R, d$  and appropriate scalar quantities; the symbol “|” represents Chinnery’s notation. The other symbols are explained in Tab. 1. Let us indicate by  $P_i$  a generic point on a regular grid defined in the XY plane as shown in Fig. 2. Moreover, let us indicate with  $u_x, u_y, u_z$  the components of the deformation referred to the  $o(x, y, z)$  coordinate system measured at the point  $P_i$  due to a tensile dislocation. These components can be easily referred to the  $O(X, Y, Z)$  coordinate system according to the following transformation formulas:

$$\begin{cases} U_X = u_x \sin \sigma - u_y \cos \sigma \\ U_Y = u_x \cos \sigma + u_y \sin \sigma \\ U_Z = u_z \end{cases}$$

where  $\sigma$  is the Strike angle.

Then, let  $U$  be the deformation vector having  $U_X, U_Y,$  and  $U_Z$  as components. We need

to project this vector along the direction of the satellite view to be able to generate an synthetic interferogram. So, let  $\rho$  be the vector of the direction cosines that defines the satellite view angle with respect to the  $O(X, Y, Z)$ . reference system. Hence the searched projection is

$$U_\rho = \rho \cdot U = \rho_X U_X + \rho_Y U_Y + \rho_Z U_Z$$

The quantity  $U_\rho$  must be scaled into the interval  $0-2\pi$  to calculate the traditional fringes that characterise an interferogram, by using the relation

$$\bar{U}_\rho = \frac{2\pi}{\lambda} \text{frac} \left( \frac{U_\rho}{\lambda} \right)$$

where  $\lambda$  is the principal wave length emitted by the satellite antenna, that is  $28 \cdot 10^{-3}$  m in the case of ERS-2, and  $\text{frac}()$  is the fractionary part. Examples of synthetic interferograms are reported in the following figures 3 a) and b).

### Inverse Modelling

The Simulated Annealing (SA) algorithm is currently one of the most powerful optimisation techniques available. S. A. has been successfully applied to geophysical inversion problems, e. g. the inversion of seismic waveforms (e. g., [Sen and Stoffa, 1991], [Scherbaum et al., 1994]). It is inspired by the optimization process of crystalline structures during the cooling down of a melt. If the liquid cools down slowly the crystals will develop an (almost) perfect structure corresponding to an (almost) absolute energetic minimum. The structures will become less perfect and thus richer in energy if the cooling is faster. The reason for this resides in the fact that, following concepts of statistical mechanics, the particles may escape a certain energy level with a probability which increases with temperature. Temporary less perfect structures are possible. If the cooling process is slow, particles will have more probability to escape local minima and to approach the global one. In turn, fast cooling will «frozen» the particles at the places just where they are since the probability of escaping a certain energy level becomes low. In our optimization with S. A. the particles of the melt correspond to the models which are fluctuating randomly within a certain model space.

In this study the observation grid is assumed to consist of a mesh of  $21 \times 21$  stations, spaced at a distance of 1000 m, covering a

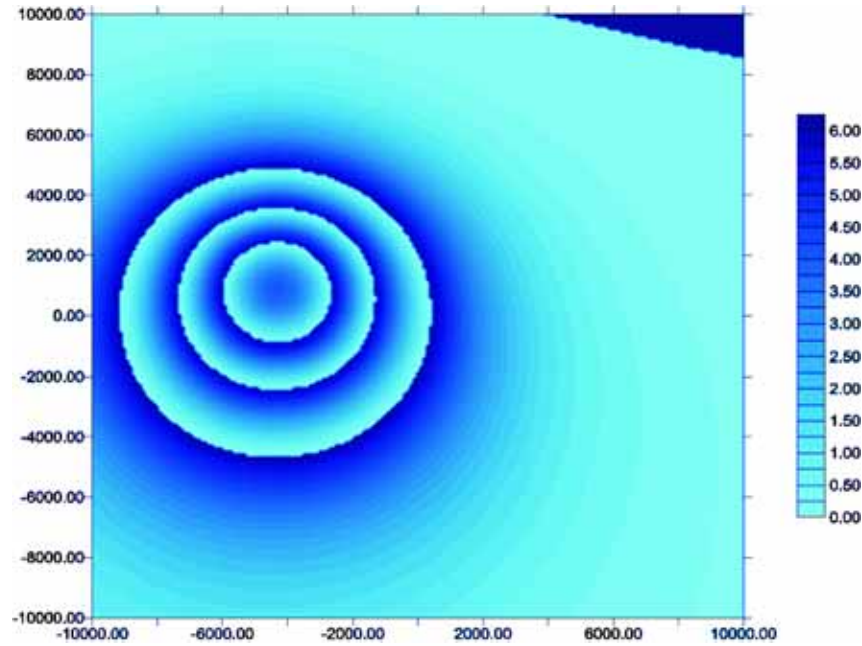


**Figure 3a** Synthetic interferogram generated by using a tensile dislocation Okada model having the following parameters: Strike = 162°, Dip = 17° Length = 1823m, Width = 1052 m, Opening = 3.82 m, Xb = - 2459 m, Yb=4047 m, Zb = -5361 m.

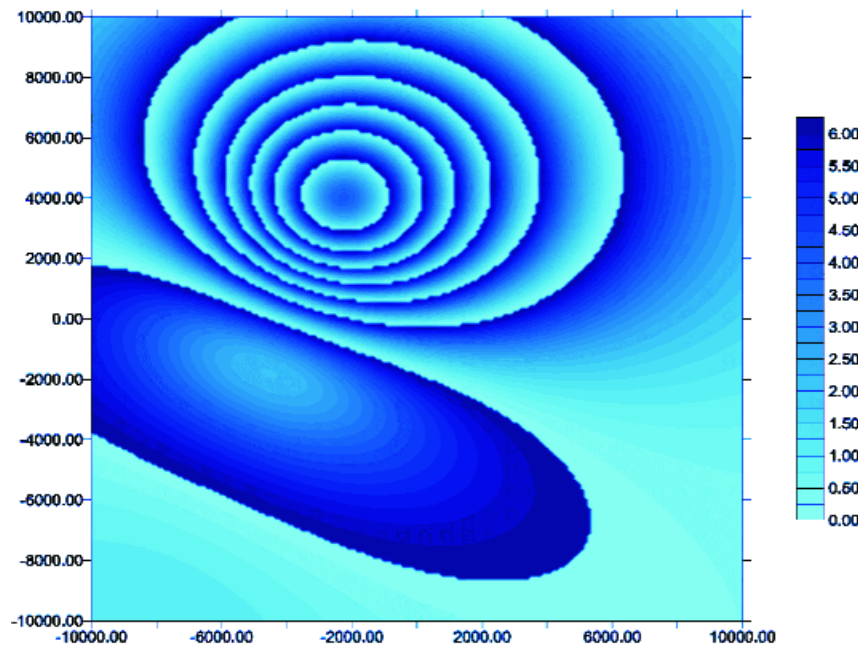


**Figure 3b** Synthetic interferogram generated by using a tensile dislocation Okada model having the following parameters: Strike = 337°, Dip = 52° Length = 2098 m, Width = 3737 m, Opening = 4.76 m, Xb = - 1612 m, Yb=3729 m, Zb = -4814 m.

region of 20x20 km. The origin of the reference system is assumed to be in the centre of the grid.

The considered cost function *Fit* is given by the following expression

$$Fit = \frac{1}{N} \sum_{i=1}^N \left[ \sum_{j=1}^3 \left| U_R^{(i,j)} - U_C^{(i,j)} \right| \right]$$

where N is the number of points of the grid (i.e. in the considered case N=21x21=441), i is the index of the row position in the grid (i=1..N), j is the direction index (X → j=1, Y → j=2, Z → j=3), UR and UC are the actual and computed deformation respectively.

Several trials were performed in order to

set the free parameters of the SA algorithm. The performance indexes considered to assess the accuracy of the implemented inversion scheme are given by the following relations, where  $j$  is the parameter index ( $j=1..8$ ):

- Mean Error  $E_M$

$$E_M^{(j)} = \frac{1}{M} \sum_{i=1}^M [V_R^{(i,j)} - V_C^{(i,j)}]$$

where  $V_R^{(i,j)}$  is the generic  $j^{\text{th}}$  variable of the  $i^{\text{th}}$  real model,  $V_C^{(i,j)}$  is the corresponding calculated variable and  $M$  is the number of models ( $M=300$ ).

- Mean Absolute Error  $E_A$

$$E_A^{(j)} = \frac{1}{M} \sum_{i=1}^M |V_R^{(i,j)} - V_C^{(i,j)}|$$

- Root Mean Squared Error  $E_R$

$$E_R^{(j)} = \frac{1}{M} \sqrt{\sum_{i=1}^M [V_R^{(i,j)} - V_C^{(i,j)}]^2}$$

- Mean Percent Absolute Error  $E_{\%}$

$$E_{\%}^{(j)} = 100 \frac{1}{R^{(j)} \cdot M} \sum_{i=1}^M |V_R^{(i,j)} - V_C^{(i,j)}|$$

where  $R^{(j)}$  is the range in which the variable  $j^{\text{th}}$  is defined.

- Standard deviation of errors  $\sigma_E$

$$\sigma_E^{(j)} = \frac{1}{M} \sqrt{\sum_{i=1}^M [E^{(i,j)} - \bar{E}^{(j)}]^2}$$

where  $E^{(i,j)}$  is the  $i^{\text{th}}$  error of the  $j^{\text{th}}$  variable, while  $\bar{E}^{(j)}$  is the mean value of the  $j^{\text{th}}$  variable.

- Index of agreement  $d$

$$d^{(j)} = 1 - \frac{\sum_{i=1}^M [V_R^{(i,j)} - V_C^{(i,j)}]}{\sum_{i=1}^M [|V_R^{(i,j)} - \bar{V}_C^{(j)}| + |V_C^{(i,j)} - \bar{V}_R^{(j)}|]}$$

where  $\bar{V}_C^{(j)}$  and  $\bar{V}_R^{(j)}$  are, respectively, the mean values of the  $j^{\text{th}}$  calculated variable and the  $j^{\text{th}}$  real one.

## Numerical Results

The values obtained for the considered

performance indexes, referring to the inversion of about 300 models, that were chosen in order to represent the whole space of parameters, are reported in the following Tab. II

Parameter	$E_M$	$E_A$	$E_R$	$E_{\%}$	$\sigma_E$	$d$
$\sigma$	3.421	17.0	22.874	4.736	22.616	0.987
$\delta$	0.75	4.4	5.867	4.937	5.818	0.987
L	66.21	359.5	452.358	5.993	447.486	0.982
W	32.98	279.9	345.664	6.999	344.087	0.977
U3	0.047	0.28	0.355	7.223	0.352	0.975
Xb	-35.4	245.13	331.324	2.451	329.419	0.997
Yb	-29.1	224.82	297.090	2.248	295.654	0.997
Zb	28.0	378.3	470.535	6.307	469.701	0.981

**Table II** Performance indexes.

It can be seen that all the model parameter are estimated with an average error  $E_{\%}$  that is lower than 10% in case of free-noise data. In more detail the source coordinates Xa and Xb are obtained with lower than 3% while for Zb the average error reaches 7%. The L, W and U3 parameters are estimated with  $E_{\%}$  around 7% while the Strike and Deep angles are both estimated with  $E_{\%}$  of about 5%. Moreover, it has been estimated that when the test data are corrupted with a gaussian type noise up to 30% the coordinates Xa and Xb are obtained with  $E_{\%}$  lower than 5% while for Zb, L and W the average error reaches about 10%. Finally the Strike and Deep angles are both estimated with  $E_{\%}$  of about 15%

## Conclusions

This paper has proposed a method for the nonlinear inversion SAR interferometric data by using a SA optimisation algorithm. More specifically, it has dealt with the inversion of ground deformation data relating to magma-filled dikes in volcanic areas. Situations of this kind are very frequent in areas like that of Mt. Etna. To guarantee a sufficient set of data for the study, the data was synthesised using models proposed by Okada. The results presented are essentially as follows. It was first experimentally demonstrated that the inversion procedure using SA can be unambiguously solved. As regards the degree of accuracy, the results obtained confirm the reliability of SA in determining the most important parameters of the model, i.e., the source coordinates and orientation, even in the presence of noise-affected data.

## Acknowledgements

This work was supported by the Italian GNV (Gruppo Nazionale per la Vulcanologia) under the coordinate project “Development and application of Remote sensing methods for the monitoring of active Italian volcanoes”.

## References

- Briole, P., Avallone, A., Beauducel, F., Bonforte, A., Cayol, V., Deplus, C., Delacourt, C., Froger, J. L., Malengreau, B., Puglisi, G., (1999). *Interferometrie Radar Appliquée aux Volcans: Cas de L'Etna et des Champs Phlégréens (Italie)*. Rapport Quadriennal CNFGG 1995-1998, pres. at Union Internationale de Geodesie et Geophysique, Birmingham, 121-128.
- Coltelli, M., Dutra, L., Fornaro, G., Franceschetti, G., Lanari, R., Migliaccio, M., Moreira, J. R., Papathanassiou, K. P., Puglisi, G., Riccio, D., Schwäbisch, M., (1996). *SIR-C/X-SAR Interferometry over Mt. Etna: DEM Generation, Accuracy Assessment and Data Interpretation*. DLR-Forschungsbericht 95-48.
- Curlander, J. C. and McDonough, R. N., (1991). *Synthetic Aperture Radar, Systems & Signal Processing*, Introduction to SAR (J. J. Wiley & Sons Inc, New York.
- Gabriel, A. K., Goldstein, R. M., Zebker, H. A., (1989). *Mapping Small Elevation Changes over Large Areas: Differential Radar Interferometry*. Journal of Geophysical Research 94, B7 9183-9191.
- Lanari, R., Fornaro, G., Riccio, D., Migliaccio, M., Papathanassiou, K. P., Moreira, J. R., Schwäbisch, M., Dutra, L., Puglisi, G., Franceschetti, G., Coltelli, M., (1996). *Generation of Digital Elevation Models by Using SIR-C/X-SAR Multifrequency Two-Pass Interferometry: The Etna Case Study*, IEEE Trans. on Geoscience and Remote Sensing, 34, 5 1097-1114.
- Massonnet, D. and Rabaute, T., (1993). *Radar Interferometry: Limits and Potential*. IEEE Trans. on Geoscience and Remote Sensing, 31, 2 435-464.
- McCloy, K. R., (1995). *The physical principles of remote sensing, Resource Management Information System – Process and Practice*. Taylor & Francis press, chp 2 , 67-96
- Okada, Y., (1985). *Surface deformation due to shear and tensile faults in a halfspace*. Bull. Seismol. Soc. Amer., vol. 75, pp. 1135–1154.
- Scherbaum, F., Palme, C., Langer, H. (1994). *Model Parameter Optimization for Site Dependent Simulation of Ground Motion by Simulated Annealing: Reevaluation of the Ashigara Valley Prediction Experiment*. Nat. Hazards, 10, pp. 275-296.
- Sen, M.K. and Stoffa, P. L., (1991). *Nonlinear One-Dimensional Seismic Waveform Inversion Using Simulated Annealing*. Geophysics 1624-1638.

### **Application of digital elevation model to volcanology**

Achilli V.<sup>1</sup>, Baldi P.<sup>2</sup>, Fabris M.<sup>1</sup>, Marsella M.<sup>3</sup>,  
Monticelli R.<sup>3</sup>, Salemi G.<sup>1</sup>

<sup>1</sup>DAUR, University of Padova

<sup>2</sup>Dipartimento di Fisica, University of Bologna

<sup>3</sup>DITS, University of Rome "La Sapienza"

in this work derive from the 1971, 1983, 1993, 1996, 2001 surveys. For the first two datasets DEM derived from images at 1:10000 scale were available while the 1:5000 images acquired in 1993, 1996 and 2001 were fully processed within this work and used for a detailed analysis of the main crater area.

The work is in press on *Annals of Geophysics*.

### **Abstract**

A number of methods based on data acquired by means of remote sensing systems are now available for the generation of Digital Elevation Models (DEM) over large areas. These include satellite SAR interferometry, airborne laser scanning, aerial photogrammetry as well as spaceborne optical and radar stereo option. Among these techniques, Digital Photogrammetry represents one of the most powerful tool for acquiring, through semiautomatic procedure, a large amount of 3D points for the generation of high spatial resolution DEM and the relative rectified images.

In digital photogrammetry in fact, the processing of the images is obtained with matching procedures which are based on well defined shape comparison techniques or on the grey level distribution in the corresponding zones of the images [Kraus 1994; Heipke 1995]. The capability of the correlation algorithms to work at sub-pixel level affects the final precision of digital products, together with the quality of the image, the presence of shadows and the morphology of the surface

In volcanic areas, digital photogrammetry techniques were experimented only recently, showing remarkable potentialities [Achilli et al., 1998; Baldi et al., 2000, 2002], such as the possibility to accurately describe morphological features of ground surfaces, to study gravitative instability phenomena induced by volcanic activity and to detect and map areas involved in crustal deformations phenomena.

The objectives of the work is to describe the photogrammetric digital procedure applied to high resolution images acquired over the Vulcano Island, to discuss the quality of the results obtained and to perform a comparative analysis using multitemporal DEM.

Low altitude photogrammetric data over the Vulcano Island have been acquired several time during the last 30 years: the data analyzed

## Analysis of High Resolution Digital Terrain Model for Morphometric Parameters Extraction and Classification

Baldi P.<sup>2</sup>, Marsella M.<sup>1</sup>, Signoretto V.<sup>2</sup>

<sup>1</sup>University of Rome "La Sapienza", D.I.T.S.

<sup>2</sup>University of Bologna, Physic Department

### Abstract

A morphometric analysis of a high resolution digital terrain model (DTM) has been performed in order to define morphological features and classify landforms of "La Fossa" Cone of Vulcano Island (Aeolian Arc, Italy). The digital model with a grid size of 1X1m has been obtained by means of an automatic digital processing of digitized airborne stereo images. Maps of the four more important morphometric parameters (slope angle, aspect of terrain, profile curvature and plan curvature) have been extracted and analyzed. The visual interpretation of morphometric maps aided by a lithology map [Keller, 1980] and vegetation boundaries map, derived from aerial photos, a classification of landform based on terrain elemental units has been performed and graphically represented as a *Terrain Units Map*. Terrain units represent geomorphologically different units characterized by a predominance of certain surface processes and therefore certain landforms. Starting from morphometric parameters a *Morphometric Units Map* has been generated, and used to perform a study about the identification of terrain instable sectors. By an automatic procedure in which morphometric parameters were the input variables, a terrain classification based on morphometric units has been derived. The classification process consisted on two steps, the classification of each slope factor into a few significant classes, stored into a single layer, and the sequentially overlaying of all the layers allowing to obtain homogeneous domains. The use of high resolution DTMs in terrain analysis allows to perform very detailed morphometric analysis to derive terrain units and slope surface boundaries maps.

### Introduction

As a sub discipline of geomorphology, geomorphometry deals with the qualitative and quantitative description and measurement of

ground surface relief. The study of landforms and patterns by numerical methods has a large spectrum of applications, from hydrology [Beven and Moore, 1992], tectonics and geomorphology [Onorati et al. 1992] to oceanography, climatology and geohazard assessment [Carrara et al. 1991; Pike, 1988]; other applications concern land-use planning, civil engineering, trafficability maps for military operations deriving and energy resources evaluation [Elliott et al. 1991]. Quantitative terrain study has been recently revolutioned by the availability of digital terrain modelling and Geographic Information System (GIS) instruments for topographic analysis and display. The landform numerical description consists on the parametrization of a ground surface model by morphometric parameters [Pike, 1993], that is "a set of measurements that describe topographic form well enough to distinguish topographically disparate landscapes" [Pike, 1988]. This concept has been taken further within the field of geomorphometry [Beven and Kirkby, 1979; Moore et al. 1991], whose basic assumption is that there is a close relationship between surface processes and surface characteristics, that can be expressed as topographic parameters. Combination of topographic parameters, through a relief classification process, define topographic units, that is areas with a predominance of certain surface processes and therefore also landforms. In literature [Florinsky, 1998] exists exhaustive lists of variables and parameters that are commonly used for geomorphological different purposes, but a systematic parametrization of relief altimetric and planimetric variation has been suggested by Evans [1972, 1980], by taking the five more important parameters that may be defined for any two-dimensional continuous surface: elevation, slope, aspect, profile curvature and plan curvature. Morphometric parameters maps together with the maps of other important slope-stability factors (lithology, tectonic structure, land-use, land-cover, clima condition, vegetation, etc.) may be the input variables in landform stability analysis, the base study for any further landslide disaster management project and for hazard mapping.

The base of relief analysis is the raw elevation data, which may be collected in a variety of ways. In the past all topographic data were collected by surveyors using instruments such as the level, theodolite and more recently EDM; today, the same data may be collected by remote sensors on airborne or spaceborne platforms (Photogrammetry, Laser Scanning, SAR) and GPS receivers. Automatic processing of data

allows to obtain a Digital Terrain Model (DTM), whose quality principally depends on density of acquired height points and on data acquisition system. The availability of digital elevation models has provided geomorphologists with new tools for quantitatively analysing topography (for an exhaustive bibliography see [Pike, 1993]) by computer manipulation of DTMs, by automating manual classifications [Dikau et al. 1990] or by devising new ones [Pike, 1988; Evans, 1980].

### Morphometric Parameters

In geomorphometry all parameters, defined as secondary point parameters [<http://rbonk.host.sk/prj/thesis/node23.html>], are derived from elevation field (primary field), in what they represent the 1<sup>st</sup> and 2<sup>nd</sup> order differentials of that primary field in the XY and orthogonal planes. Elevation belongs to the primary point parameters, whose characteristic is to express the distance from a given point to important area, line, or point; in the case of elevation, the base area is the Geoid, defined as equipotential surface of Earth's gravitational field, and elevation is the level of gravitational energy of earth's surface points as well. According to that statement, all morphometric parameters derived from elevation (H) have their physical interpretation as characteristics of Earth's gravitational field and their expressions on earth's surface. They are attributes of every point on Earth's surface and can be defined as changes of primary positional parameter in various directions within differentially small surrounding area of given point. Slope is the most important measure under which geomorphic agents work, and it determines the horizontal component of gravity which drives water and materials downward.

Slope angle  $\alpha$  in a point A (Fig.1) is the angle between the plane tangent to the topographic surface at the point and horizontal plane, parallel to Geoid surface. Slope is classified as a vector which has a quantity (Gradient) and a direction (Aspect). The value of the gradient determines velocity of surface gravitational processes, and its spatial changes determine the acceleration and deceleration of processes. If slope gradient is defined as the maximum rate of change in altitude, aspect is the compass direction of this maximum rate of change (Fig.1), defined by degree of exposition of terrain against from certain direction acted processes, such as wind, solar radiation, wave motion

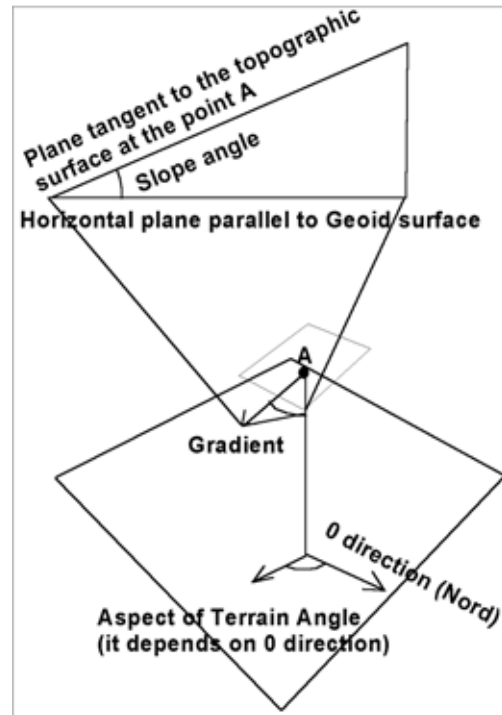


**Figure 1** Slope components [slope gradient can be express in percent or in degrees].

[Minár, 1998]. Because of changing direction of acted processes, this parameter is usually expressed by Aspect of Terrain to world's sides, ranging from 0 to 360°.

Curvature, or Laplacian (scalar), is another important parameter in slope dynamic analysis; it expresses diverging and converging material (rate of erosion and deposition) or water flow [<http://www.lapgis.chs.nihon-u.ac.jp/nogami/measures.html>]. Flow divergence or convergence depends on the direction of flowlines downslope; flowlines are imaginal lines on the terrain oriented in every point in the direction of maximal slope. Flowline curvature in gradient direction (Profile Curvature, Fig.2) reflects the change in slope angle and thus controls the change of velocity of mass flowing down along the slope curve. Profile curvature is responsible of deceleration of gravitational flows, in case of concave flowlines form, and of acceleration in case of convex flowlines form. Flowline curvature in the gradient perpendicular direction (Fig.2) reflects the change in aspect angle and influences the divergence/convergence of gravitational flows. It is responsible of divergence, in case of convex flowlines form, and of convergence, in case of concave flowlines form [Peschier, 1996]. This curvature usually is measured in the horizontal plane as the curvature of contours and is called Plan Curvature

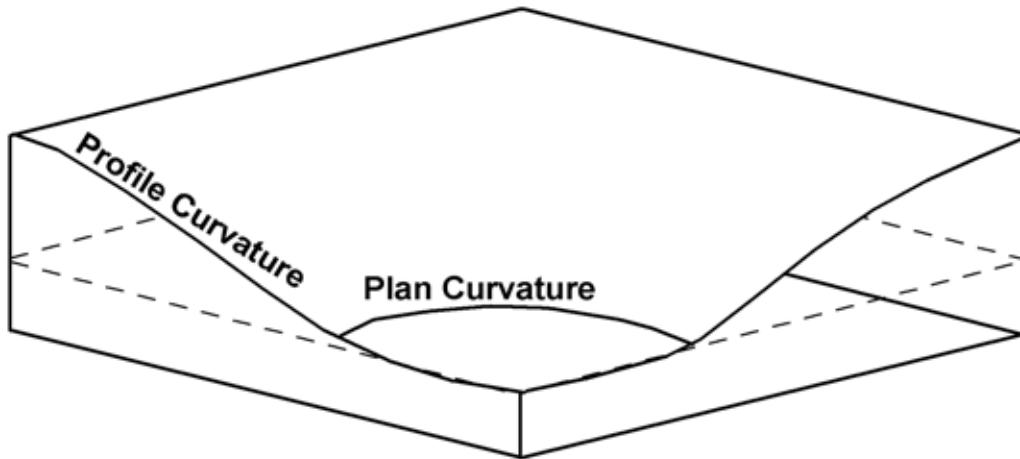


Figure 2 Geometric forms of slope.

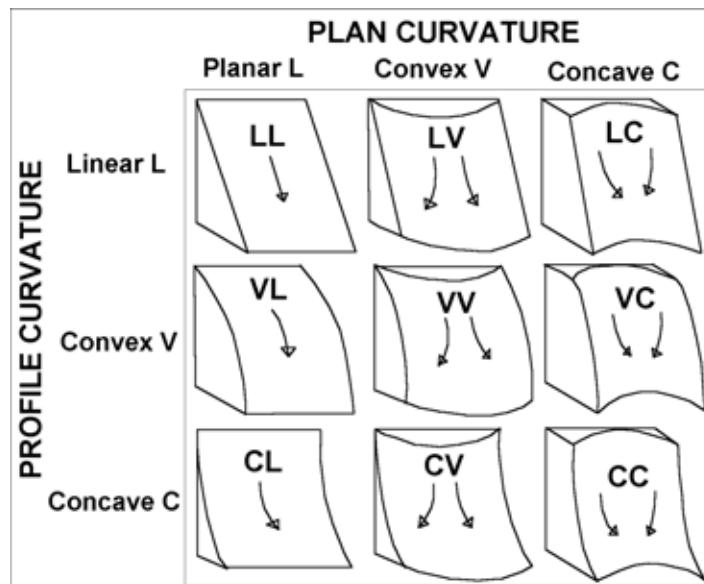


Figure 3 Nine possible landforms obtained by combining the concepts of profile and plan curvature.

[Zevenbergen and Thorne, 1987; Moore et al. 1991].

Krcho [1973, 1991] introduced, for the study of flow divergence/convergence, the more appropriate concept of Tangential Curvature, measured in the normal plane in the direction perpendicular to gradient, that is the direction of tangent to contour at a given point. By combining the concepts of Profile and Plan Curvature it is possible to obtain all the nine possible landforms (Fig.3), with the exception of the horizontal plane on which no flowlines can be defined and so curvature values are zero.

### Landform Units Classification

In literature all major approaches repre-

senting landform treat this surface as composed of smaller units [http://www.geovista.psu.edu/sites/geocomp99/Gc99/067/gc\_067.htm], defined by portions of land surface containing a set of ground conditions which differ from the adjacent units across definable boundaries [Hansen, 1984]. In general there is no single agreed-upon the criteria to establish the nature and the characters of landform units, but essentially three classification criterious are the more adopted by authors. Speight [1977] makes units boundaries reflecting geomorphological and geological differences, by manually defining "Terrain units"; the main drawback of the method is that it is intrinsically subjective, thus different investigators often classify a region in a different way.

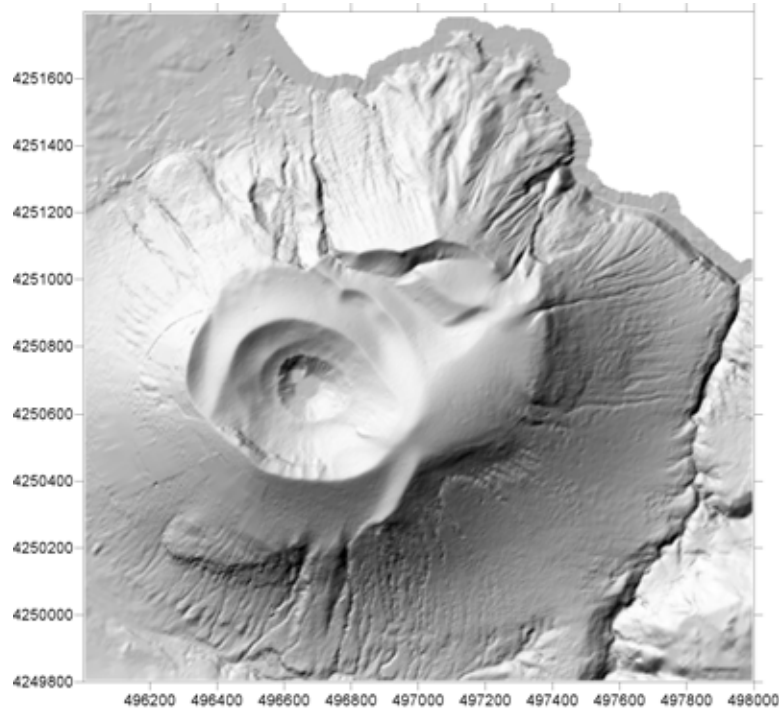


**Figure 4** Shaded Relief Representation of “La Fossa” Cone’s 1996 DTM.

Mark and Ellen [1995] support an approach in which DTM’s grid-cells become the terrain-unit of reference; the limitation of the method is that units boundaries do not bear any relation to geomorphological, lithological or environmental boundaries. Chung et al. [1995] adopt an automatic terrain classification technique which consists on the extraction by DTM of elemental units (“Unique Condition Units”, UCU) that represent an aggregation of pixels that exhibit homogeneous properties [<http://rbonk.host.sk/prj/thesis/node23.html>]. The method is performed with the iterative cluster analysis, that groups images pixels into unique categories according to values of a coefficient of similarity and allows to obtain a single output map in which the number, size and nature of UCU are strictly dependent on the criteria used in classifying the input factors.

The main drawback of the method lies in the fact that the full objectivity of the technique, it being the result of an automated overlay algorithm, is inherent with the subjectivity in factors classification [Carrara and Guzzetti, 1995].

### Study area

Aeolian volcanic arc, located in the Tyrrhenian Sea (Italy) approximately 15 miles to the NE of Sicily, is built on the Sicilian-

Calabrian northern continental slope, which grades northward down to the south-east Tyrrhenian bathyal plain [Kokelaar P. and Romagnoli C., 1995].

The arc has a continental crust basement [Calanchi et al. 1995], 16-18km thick, and it is located along a very active fault system [Neri et al. 1991] that trend mainly NE-SW, NW-SE and E-W [Capaldi et al. 1978, Fabbri et al. 1980, 1982]. The archipelago is constituted from seven islands, four of which, Alicudi, Filicudi, Panarea e Stromboli, with Sisifo, Enarete, Eolo, Lamentini, Alcione and Palinuro seamounts, form a semi-arc structure elongated W-E with a 7000km<sup>2</sup> areal development and a 200km linear development. Salina, Lipari and Vulcano form the central aeolian septor, elongated NNW-SSE [Amore et al. 1996]. The Vulcano Mount’s base is at a depth of 1000m; the island is about 450m high above m.s.l. with an area of 22km<sup>2</sup>. Morphologically Vulcano can be divided into four main structural units: Southvulcano, Lentic mountains, Fossa of Vulcano and Vulcanello peninsula. Fossa of Vulcano is the active crater of the island which rises from sea level up to 390m forming a steep cone. It’s activity, whose last experienced eruptive process in 1888-1890, is characterized by eruptions separated by long intervals of low activity. The systematical monitoring of the volcano processes, allowed the observation of a persisting fumarolic activity

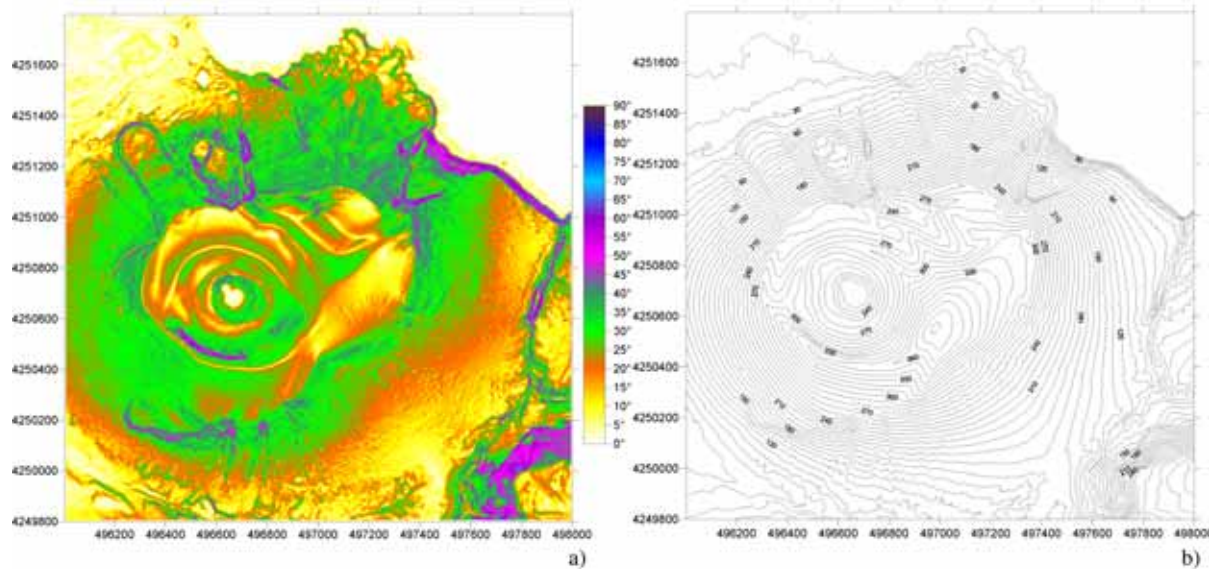


**Figure 5** a) Slope Angle Map and b) Contour Lines Map of “La Fossa” Cone’s 1996 DTM.

with variation of chemical composition, low seismic activity and opening of new fractures [Barberi et al. 1991]. The most conspicuous petrological feature of Vulcano is the potassic character, already present in the most unfractionated magmas (shoshonitic-basalts) of Southvulcano and maintained over rhyolitic lavas formed the Lentia mountain group and over recent activity of La Fossa Cone [Keller, 1980]. Morphodynamic evolution of Fossa Cone is deeply controlled by the simultaneous actions of exogenous and endogenous (e.g. high-temperature fluids circulation) factors. The data analysed in this paper were collected over the Vulcano Island by mean of aerial photogrammetry surveys in 1983 and 1996, before and after the 1988 landslide which affected the northeastern side of the volcanic cone producing a small tsunami in the harbour area [Tinti et al. 1999]. This event was due to the dynamically unstable conditions of the volcano [Rasà and Villari, 1991].

#### Nature of Used Terrain Data

Morphometric analysis of the terrain sub-aerial surface of “La Fossa” Cone of Vulcano Island has been performed starting from an high resolution Digital Terrain Model having a 1X1m grid size (Fig.4).

Elevation data have been derived by an aerophotogrammetric survey performed in September 1996. An accurate GPS control net-

work was established in the area positioning on the ground 22 specially designed aerial targets, used as Ground Control Points [Baldi et al. 2000]. The stereo images, acquired at a scale of 1:5000 [Achilli et al. 1997], where digitalized at a resolution of 1000dpi, corresponding to a ground pixel size of about 12 cm; a 1-meter grid DTM of “La Fossa” Cone has been obtained by the automatic correlation module of Helava System [DPW 710] [Muller et al. 1995].

#### DTM elaboration

Starting from terrain surface grid and by an automatic method has been possible to extract the four main morphometric attributes maps: slope angle, aspect of terrain, plan and profile curvatures. They depict terrain morphologic characteristic and allow to perform, by their interpretation, a detailed analysis of topographic surface planimetric and altimetric variations. Classified digital maps of morphometric parameters of “La Fossa” Cone were prepared. In *Slope Angle Map* image pixels have been grouped in nine classes of ten degrees each. Comparing slope angle map with a traditional contour map (Fig.5 a, b), it is clear that the slope angle visualization map offers an overall view of the slope angle trend over the study area and of its spatial variations.

In *Aspect of Terrain Map* image pixels have been grouped in twelve classes of thirty degrees each (Fig. 6).

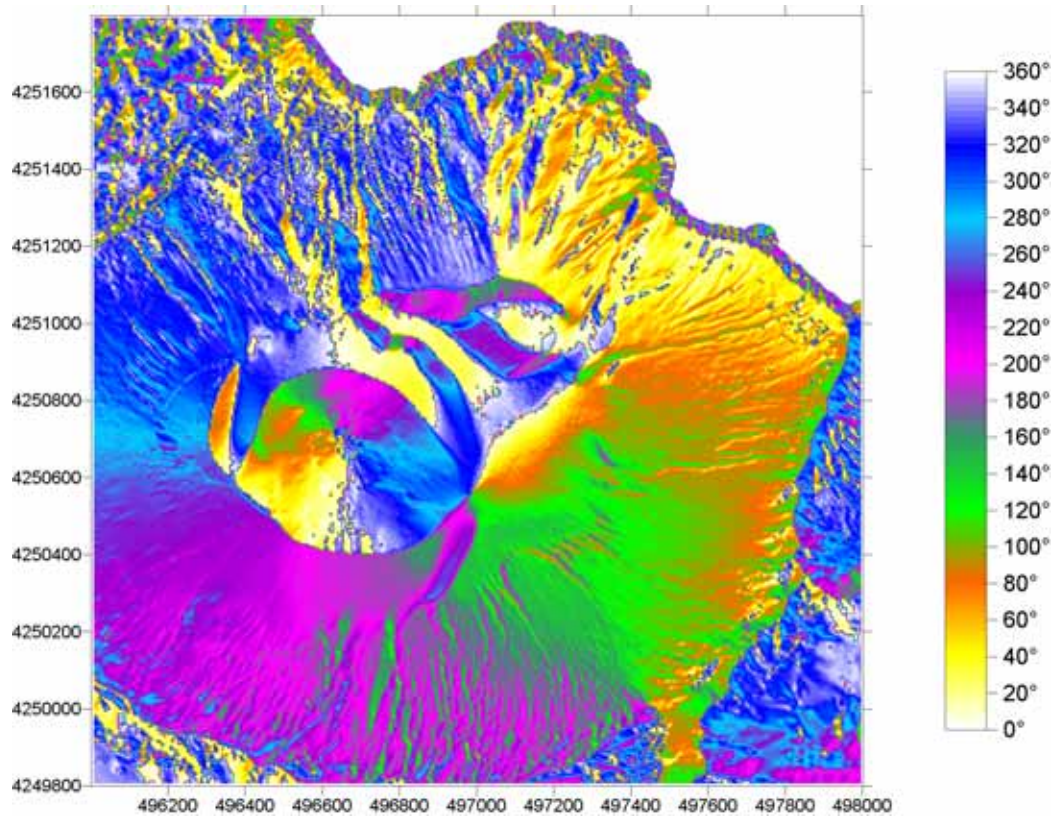


**Figure 6** Aspect of Terrain Map of “La Fossa” Cone’s 1996 DTM.

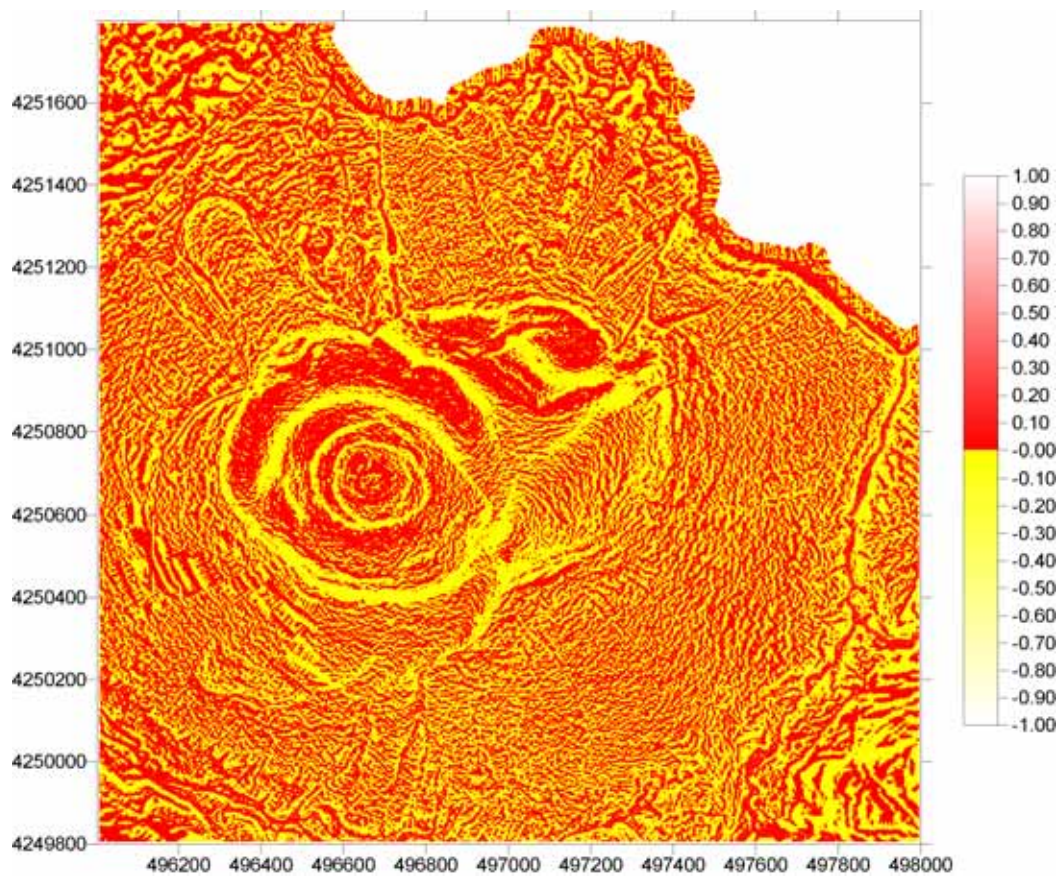


**Figure 7** Profile Curvature Map of “La Fossa” Cone’s 1996 DTM.

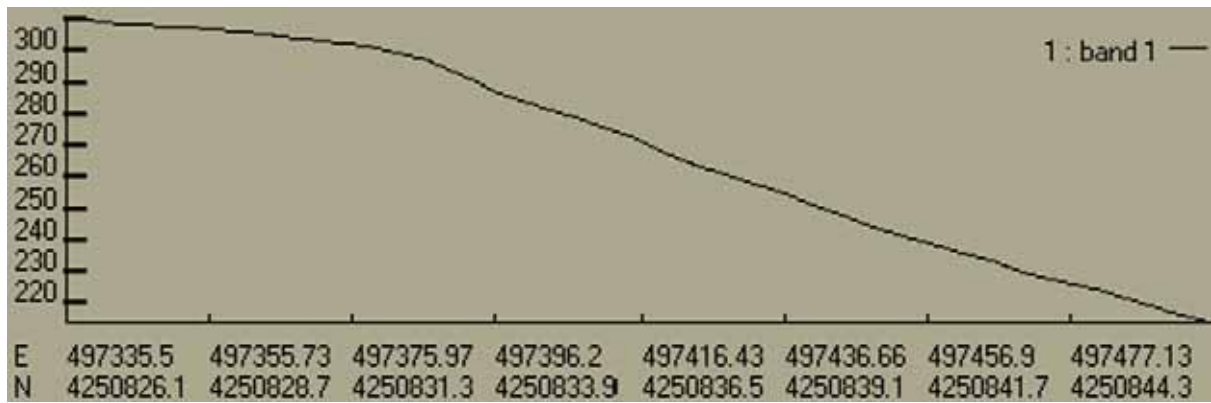


**Figure 8** Traverse section of ESE flank of “La Fossa” Cone: the terrain surface slope angle change correspond to a lithologic boudary.

Aspect of terrain map allows to define crest and drainage lines with the aim to made considerations about gravitative processes directions. In *Profile Curvature Map* image pixels have been grouped in three classes corresponding to concave (jellow areas), convex (red areas) or linear (blue areas) slope surface forms in the gradient direction (Fig.7).

Profile curvature map allows to localize the boundaries between slope surface sectors with concave or convex forms, that can be linked to geologic or geomorphologic boudaries. This is the case of

ESE flank of “La Fossa” Cone, where the passage from convex profile curvature to linear profile curvature (300m m.s.l) corresponds to the lithologic boundary between the upper Pyroclastic doposits of the recent eruptions of Fossa di Vulcano and the lower “Fossa Rossa” ash-tuffs (Fig.8).

In cases of the slope surface submitted to mass movements erosive processes, the boundaries between concave forms and convex forms correspond to erosion/deposition morphologic boudaries.

In the *Plan Curvature Map* image pixels

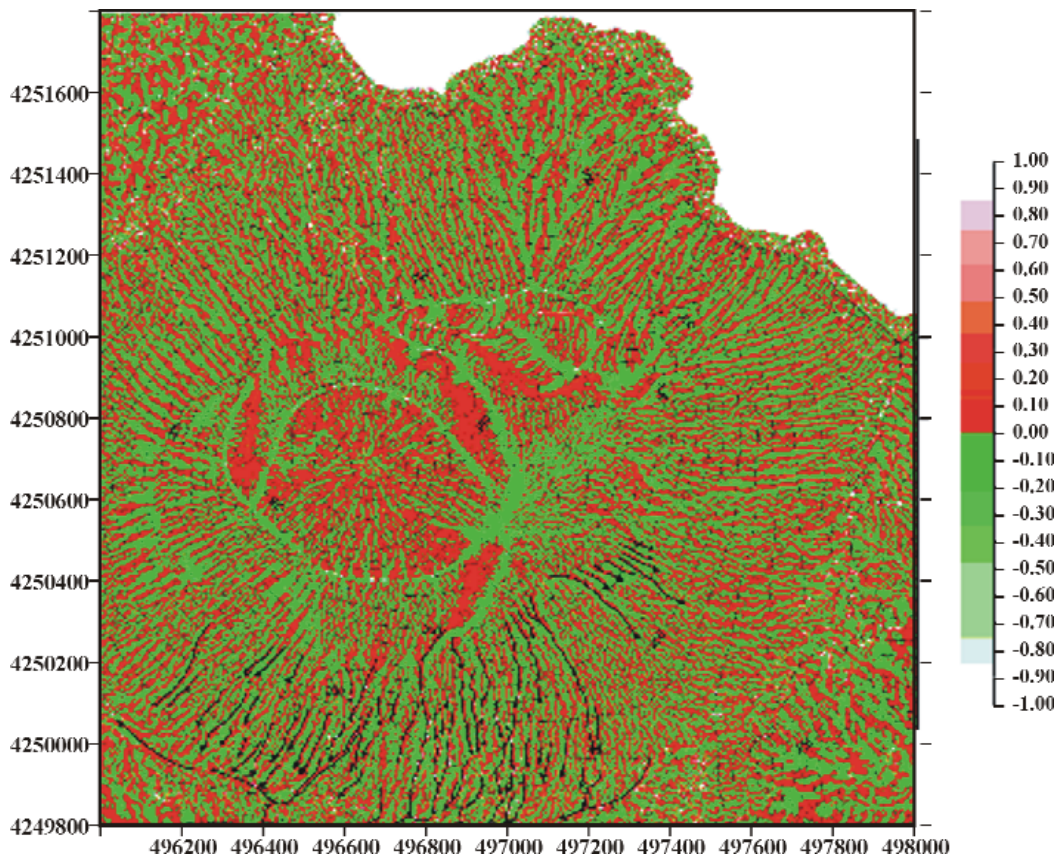


**Figure 9** Plan Curvature Map of “La Fossa” Cone’s 1996 DTM.

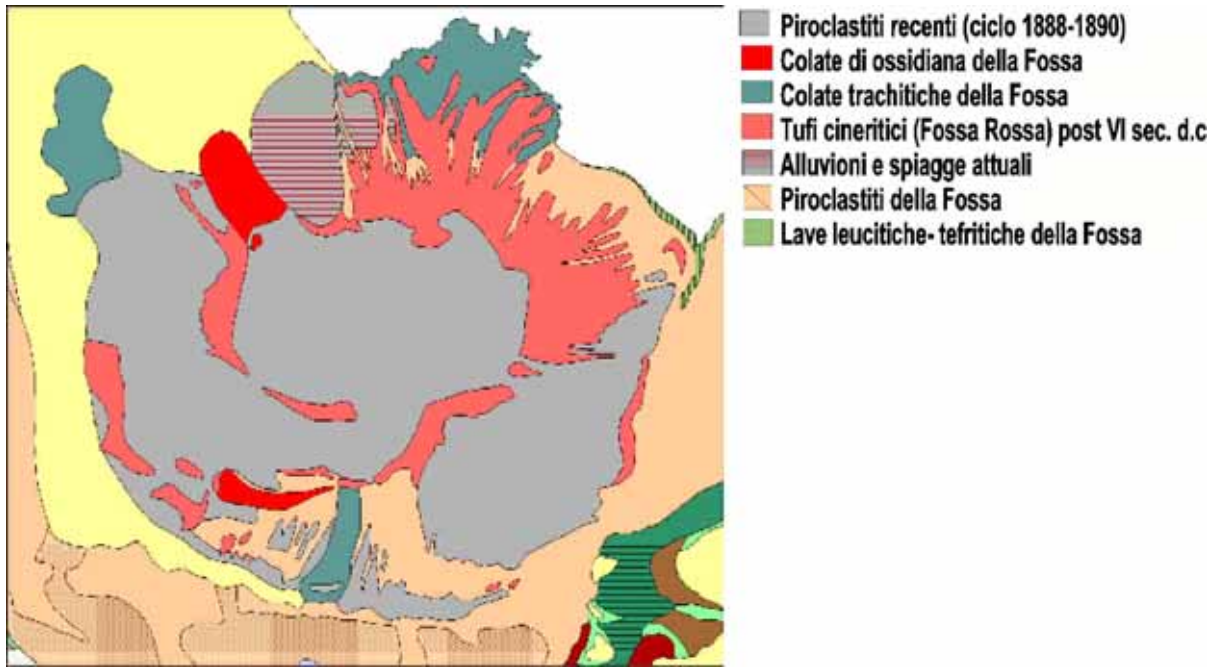


**Figure 10** Lithology Map of “La Fossa” Cone extract by digitalizing Geologic Map of Vulcano Island [Keller, 1970].

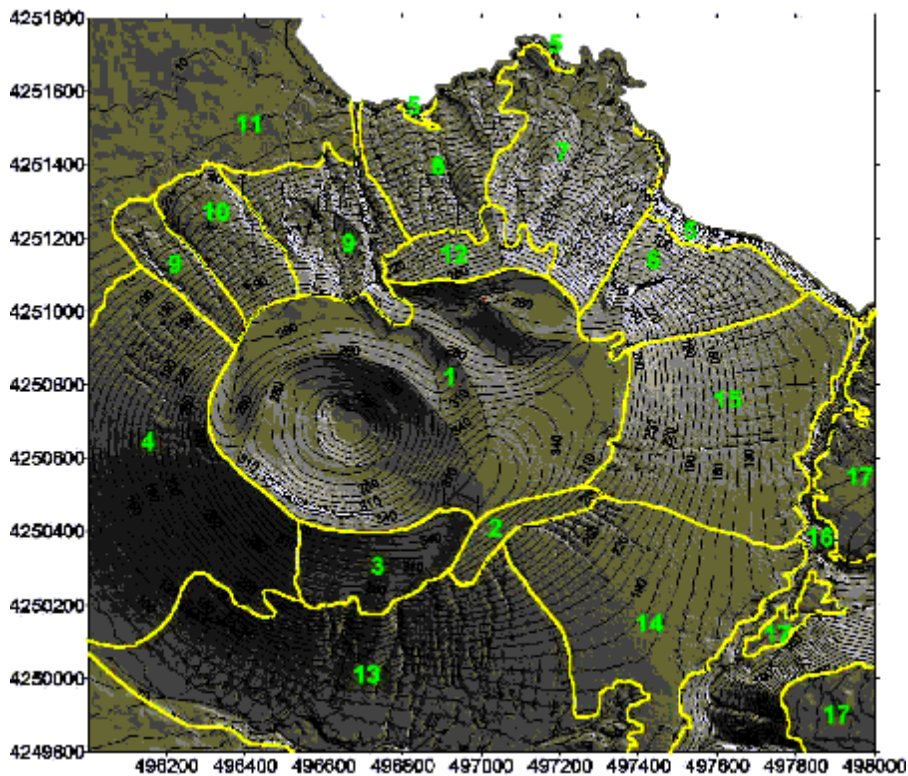


**Figure 11** Terrain Units Map of “La Fossa” Cone’s 1996 DTM.

have been grouped in three classes, respectively corresponding to concave (green areas), convex (red areas) or planar (yellow areas) slope forms in the gradient perpendicular direction (Fig.9). Plan curvature parameter map allows to obtain drainage lines, which corresponds to concave slope surface.

#### Terrain Units Map

The terrain units boundaries have been extracted by a visual interpretation of morphometric parameters maps: the extracted boundaries have been modified integrating the infor-

mations with lithology (Fig. 10), vegetation boundaries (extracted from the digital orthophoto), and morphological features visible on the DTM.

The obtained *Terrain Units Map* evidenced sectors where different topographic fea-

tures prevail (Fig. 11); these informations support the terrain analysis in acting morphodinamic processes evidencing and mapping.

The different terrain units defined in the terrain units map are listed in Tab.1:

	Location	Morphometric characteristics	Note
1	Summit area limited by crater rims	Area formed by sectors with different aspect of terrain; low slope angles, ranging from 0 to 25° locally reaching 50°/75° (N sector of the area, where a steep scarp boards the ridge valley south flank and SW sector of the actually active crater area, where two breaks on slope border a steep scarp); complete lack of vegetative cover and very simple drainage network.	
2		SE aspect of terrain; intermediate slope angles ranging from 25° to 50°; complete lack of vegetative cover; complete lack of linear erosional processes.	
3		Aspect of terrain ranging from WSW to S; low slope angles ranging from 0° to 25°; presence of vegetative cover; complete lack of drainage network.	Area probably interested by the presence of blocks.
4		Aspect of terrain ranging from NW to SW; slope angles ranging from 25° to 50° in the upper sector and from 0° to 25° in the lower sector; lack of vegetative cover in the upper sector and presence of vegetative cover in the lower sector; low intensity linear processes due to elementar rill channels with a drainage pattern from parallel to radial and not hierachically arranged.	
5		Aspect of terrain ranging from N to E; high slope angles ranging from 50° to 75°; complete lack of vegetative cover.	Slope sector affected by wave erosion and gravitative down slope processes.
6		Aspect of terrain ranging from N to ENE; intermediate slope angles, ranging from 25° to 50°, in the southern sector and by high slope angles, ranging from 50° to 75°, in the northern sector; complete lack of vegetative cover; high density channels inflow with a drainage pattern from parallel to radial and drainage lines seldom hierarchically arranged; presence of several discontinuous steep scarps boardering the landslide sector.	Slope sector affected by high intensity areal processes caused by mass-movements such as rock falls and rock slides. The landslide sector seems inserted in a flank delimited by structural discontinuities, interested by water erosion in raining times, that trascend the Fossa cone zone.
7		Aspect of terrain ranging from NNW to ENE; slope angles ranging from 25° to 50° in the upper sector and from 0 to 25° in the lower sector; presence of vegetative cover; high sinuosity and high density drainage lines with a good hierarchic arrangement.	
8		Aspect of terrain ranging from NNW to WNW; slope angles ranging from 25° to 50°; presence of vegetative cover; intermediate linear processes due to drainage channels seldom hierarchically arranged.	
9		Aspect of terrain ranging from N to WNW; high slope angles ranging from 50° to 75°; poor vegetative cover; intermediate drainage density; rill channels have a drainage pattern from parallel to radial and seldom hierarchically arranged. Presence of several steep scarps associated with the Forgia Vecchia crater rims.	
10		Aspect of terrain ranging from WNW to NNE; slope angles ranging from 25° to 50°; poor vegetative cover; very simple and poor drainage network.	
11		Low slope angles ranging from 0° to 25°.	Sectors of human insediaments.
12		Aspect of terrain ranging from NNE to NNW; intermediate slope angles ranging from 25° to 50°; lack of vegetative cover; linear erosional processes.	

13		Aspect of terrain ranging from WSW to S; low slope angles, ranging from 0 to 25°, in the middle-lower sector, and intermediate slope angles, ranging from 25° to 50°, in the upper sector; complete lack of vegetative cover, except for limited zones; very high density rill channels with a drainage pattern from parallel to radial and seldom hierarchically arranged. Presence of a steep scarp coincident with the lower boundary of Palizzi lava flow.	
14		Aspect of terrain ranging from SSE to ESE; low slope angles ranging from 0 to 25°; presence of vegetative cover; elemental rill channels with a radial and not hierarchic pattern.	
15		Aspect of terrain ranging from ESE to NNE; low slope angles, ranging from 0 to 25°, in the middle-lower sector, and intermediate slope angles, ranging from 25° to 50°, in the upper sector; vegetative cover prevailing in the middle sector; rill channels, with a drainage pattern from parallel to radial and seldom hierarchically arranged, in the middle sector (80- 160m m.s.l).	Drainage density is higher than observed in (14).
16	Gorge of Rio Grande	Aspect of terrain ranging from WSW to NNE; high slope angles ranging from 25° to 50°, locally reaching 75°; presence of vegetative cover.	
17		Aspect of terrain ranging from SW to NNE; low slope angles ranging from 0° to 25°; presence of vegetative cover.	

### Unique Condition Units Map

The Unique Condition Units boudaries can be extracted by an authomatic classification procedure based on an iterative cluster analysis in which morphometric attributes are the input parameters. This unsupervised classification method may be adopted to perform landform

monitoring studies, to the eveluation of the presence of potentially unstable sites. This objective may be achieved by comparing dedicated *Unique Condition Units Maps* obtained from a temporal series of DTMs; this comparison allows us to evaluate if a particular sector of the study area has varied its morphometric class as a consequence, for example, of an instability

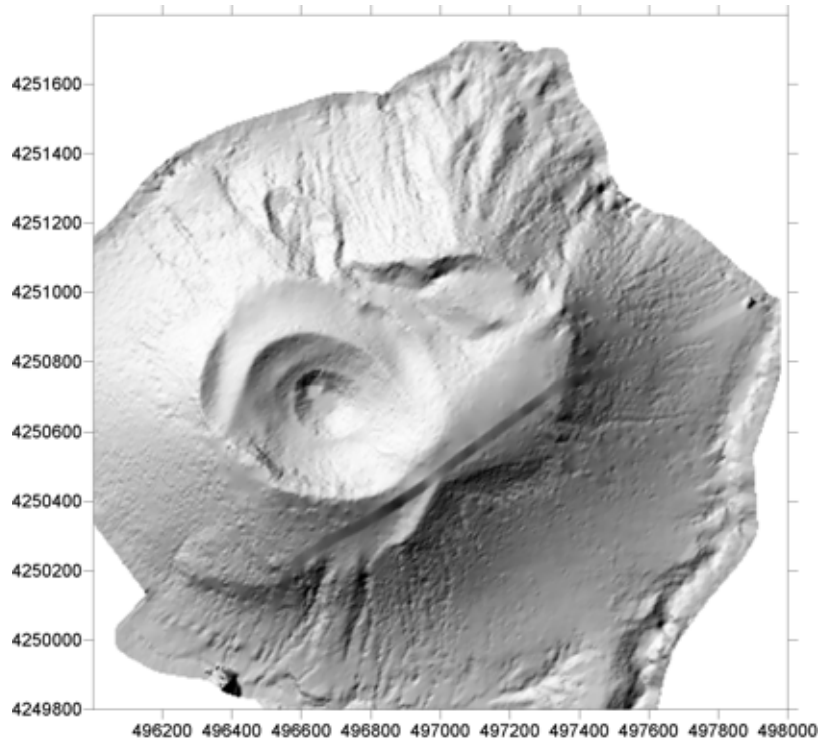
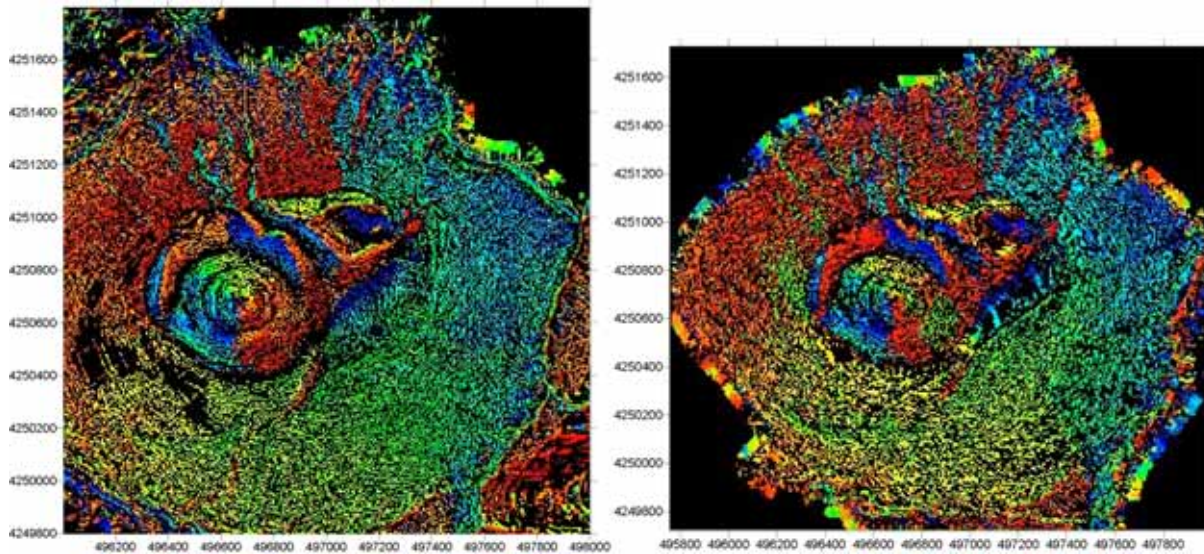


Figure 12 Shaded Relief Representation of “La Fossa” Cone’s 1983 DTM.



**Figure 13** Unique Condition Units Maps of “La Fossa” Cone’s a) 1983 DTM and b) 1996 DTM.

process (e.g. landslide). In this way it is possible to assume if other sectors of the area, with the same initial morphometric characteristics, might be affected by the same instability process. Such final considerations must be supported by different nature data regarding lithology, structural features, rocks geotechnical and site geophysical characteristics.

A morphometric analysis of a 1983 DTM of “La Fossa” Cone has been performed in order to obtain morphometric parameter maps and to study morphometric features of NE flank of “La Fossa” Cone before the 1988 landslide (Fig.12).

Finally, Unique-Conditions-Units Maps from 1983 and 1996 data of “La Fossa” cone have been generated starting from morphometric parameters maps, with the aim to support the study on the identification of terrain instable sectors (Fig.13).

## Conclusions

The availability of high resolution digital terrain models, like those overall view acquirable by aerial photogrammetry technique supported by GPS surveys, allows to perform a detailed morphometric analysis of the terrain physical surface. Topographic attributes visualization maps allow to have terrain surface variations over the study area, and therefore to perform a critic analysis of their spatial trends. Morphometric parameters maps allows to undertake a terrain classification process finalized to the definition of study area’s sectors with

prevalence of specific morphometric characteristics and therefore more likely to be interested by different morphological processes.

The generation of such supervised classification is strongly influenced by the operator. It allowed us to obtain a classification map (*Terrain Units Map*) in which sector’s boudaries have similar geomorphological, geological or structural characteristics. The unsupervised classification procedure, that allows to obtain the Unique Condition Units Map, is characterized by a nearly total objectivity, except for what concern the selection of input parameters. The comparison of UCU maps derived from DTMs acquired in various epochs may support the identification of potentially instable sites. The procedure described in this paper to perform detailed morphometric analysis results to be very adapted in remote and difficult access areas, where the performance of traditional field surveys are greatly limited.

## References

- Anderson, H. and Jackson, J., (1987). The deep seismicity of the Tyrrhenian Sea. *Geophys J. R. Astron Sec.* 91, 613-637.
- Achilli, V., Anzidei, M., Baldi, P., Marsella, M., Mora, P., Targa, G., Vettore, A. and Vittuari, L., (1997). GPS and digital photogrammetry: an integrated approach for monitorino round deformations on a volcanic area. In: *Proc. ISPRS WG VI/3 ‘International Cooperation and Technology Transfer’ Miting, Padova, 1-*

- 5, (Mussio, ed.), L., Crippa, B. & Vettore, A., Politecnico di Milano, Italy.
- Achilli, V., Baldi, P., Baratin, L., Bovini, C., Ercolani, E., Gandolfi, S., Anzidei, M. and Riguzzi, F., (1998). Digital Photogrammetric Survey on the Island of Vulcano. *Acta Vulcanologica*, 10, 1-5.
- Baldi, P., Bonvalot, S., Briole, P. and Marsella, M., (2000). Digital photogrammetry and kinematic GPS applied to the monitoring of Vulcano Island, Aeolian Arc, Italy. *Geophys. J. Int.*, 142, 801-811.
- Baldi, P., Marsella, M. and Vittuari, L., (1998). Airborne GPS performance during a photogrammetric project. In: IAG Scientific Assembly, Rio de Janeiro, Proceedings Series, 118, pp. 343-348, Springer Verlag, Berlin.
- Barberi, F., Gasparini, P., Innocenti, F. and Villari, L., (1973). Volcanism of the Southern Tyrrhenian Sea and its geodynamic implications. *J. Of Geophys Resources*, 78, 5221-5232.
- Barberi, F., Neri, G., Valenza, M. and Villari, L. (1991). 1987-1990 unrest at Vulcano. *Acta Volc.*, 1, 95-106.
- Barringer, J.R.F. and Lilburne, L., (1997). An Evaluation of Digital Elevation Models for Upgrading New Zealand Land Resource Inventory Slope Data. Presented at the second annual conference of GeoComputation '97 & SIRC '97, University of Otago, New Zealand, 26-29 August.
- Beven, K.J. and Kirkby, N., (1979). A physically based, variable contributing area model of basin hydrology. *Hydrological Sciences*, 24, 43-69.
- Beven, K.J. and Moore, I.D., (1992). Terrain analysis and distributed modelling in hydrology: Advanced in hydrological processes. John Wiley & Sons, England, 249 pp.
- Butler, J.B., Lane, S.N. and Chandler, J.H., (1998). Assessment of DEM quality for characterizing surface roughness using close range digital photogrammetry. *Photogrammetric Record*, 16 (92), 271-291.
- Calanchi, N., Romagnoli, C. and Rossi, P.L., (1995). Morphostructural features and some petrochemical data from the submerged area around Alicudi and Filicudi volcanic islands (Aeolian Arc, southern Tyrrhenian Sea). *Mar. Geology*, 123, 215-238.
- Capaldi, G., Guerra, I., Lo Bascio, A., Luongo, G., Pece, R., Rapolla, A., Scarpa, R., Del Pezzo, E., Martini, M., Ghiara, M.R., Lirer, R., Munno, R. and La Volpe, L., (1978). Stromboli and its 1975 eruption. *Bull. Volc.*, 41, 259-285.
- Carrara, A., (1989). Landslide hazard mapping by statistical methods: a "black-box" model approach. *Proceed. Int. Workshop Natural Disasters in Europ.-Mediterr. Countries*, Perugia, June 27-July, 1, 1988, CNR-USNSF, 205-224.
- Carrara, A., Cardinali, M., Detti, R., Guzzetti, F., Pasqui, V. and Reichenbach, P., (1991). GIS technique and statistical models in evaluating landslides hazard. *Heart Surf., Process. And Landforms*, 16, 427-445.
- Carrara, A. and Guzzetti, F., (1995). *Geographical Information Systems in Assessing Natural Hazards*. Kluwer Academic Publishers, Dordrecht, the Netherlands, 353 pp.
- Carrara, A., Cardinali, M., Guzzetti, F. and Reichenbach, P., (1995). GIS-Based technique for mapping landslide hazard. *Accademic Pub., Dordvecht, the Netherlands*, 40 pp.
- Chung, C.F., Fabbri, A.G. and van Westen, C.J., (1995). Multivariate regression analysis for landslide hazard zonation. (Carrara A. and Guzzetti F., ed.), *Geographical Information Systems in Assessing Natural Hazards*, Kluwer Pub., Dordrecht, the Netherlands.
- De Bortoli, S. *Applicazione Di Metodologie Gis Allo Studio Dell'instabilita' Potenziale Dei Versanti In Aree Campione Del Territorio Astigiano (Italia)*. Unpublished thesis. (<http://digilander.iol.it/stefanodb/>)
- Dikau, R., Brabb, E. and Mark, R. K., (1991). Landform classification of New Mexico by computer. U.S. Geological Survey, Open-file Report, 91-634, 15 pp.
- Dikau, R., (1989). The application of the digital relief model to landform analysis in geomorphology. In: Raper, J. (editor). *Three dimensional application in Geographical information system*, 51-77. (Taylor & Francis, London, New York, Philadelphia, ed.).
- Dikau, R., (1990). Geomorphometric landform modelling, based on hierarchy theory. In: *Proceedings of the 4th international symposium on spatial data handling*, pp. 230-239, Zurich.
- Dikau, R., (1990). The application of a digital relief model to landform analysis in geomorphology. In: (Raper, J., ed.). *Three dimensional applications in Geographic Information Systems*. Taylor & Francis, London, 1989, pp. 51-77.
- Elliott, D.L., Wendell, L.L. and Gower, G.L., (1991). An assessment of the available windy land area and wind energy potential in the contiguous United States. Richland, WA, Pacific Northwest Lab. Report PNL-7789, 61 pp.
- Evans, I.S., (1972). *General geomorphometry, deriv-*

- atives of altitude and descriptive statistics. In: (Chorley, R.J., ed.), *Spatial Analysis in Geomorphology*, 17-90 pp., Methuen.
- Evans, I.S., (1980). An integrated system of terrain analysis for slope mapping. *Zeitschrift fur Geomorphologie*, 36, 274-295.
- Fabbri, A., Ghisetti, F. and Mezzani, L., (1980). The Peloritani-Calabria Range and the Gioia Basin in the Calabrian Arc (Southern Italy): relationship between land and marine data. *Geol. Rom.*, 19, 131-150.
- Fabbri, A., Rossi, S., Sartori, R. and Barone, A., (1982). Evoluzione neogenica dei margini marini dell'arco Calabro Peloritano: implicazioni geodinamiche. *Mem. Soc. Geol. It.*, 24, 357-366.
- Florinsky, I.V., (1998). Combined analysis of digital terrain models and remotely sensed data in landscape investigations. *Progress in Physical Geography*, 22, 33-60.
- Guzzetti, F. and Reichenbach, P., (1994). Towards the definition of topographic divisions for Italy. *Geomorphology*, 11, 57-75
- Guth, R., (1995). Slope and aspect calculations on gridded digital elevation models: examples from a geomorphometric toolbox for personal computers. *Zeitschrift fur Geomorphologie*, N.F., Supplemental Band, 101, 31-52.
- Hansen, A., (1984). Landslide hazard analysis. In: Brunsden D., and Prior D.B., (Editors), *Slope instability*. Wiley, New York, 523-602 pp.  
<http://www.lapgis.chs.nihon-u.ac.jp/nogami/measures.html>
- <http://rbonk.host.sk/prj/thesis/node23.html>:  
Introduzione ai parametri morfometrici  
[http://www.geovista.psu.edu/sites/geocomp99/Gc99/067/gc\\_067.htm](http://www.geovista.psu.edu/sites/geocomp99/Gc99/067/gc_067.htm)
- [http://www.geog.ubc.ca/courses/klink/g516/talks\\_2001/slope\\_calculation.html](http://www.geog.ubc.ca/courses/klink/g516/talks_2001/slope_calculation.html)
- Iwahashi J., Watanabe S and Furuya T., (2001)- Landform analysis of slope movements using DEM in Higashikubiki area. *Japan. Computers & Geosciences*, 27 (7), 851-865.
- Keller, J., (1970). Carta Geologica dell'Isola di Vulcano. Scala 1:10000. Litografia Artistica Cartografica. Firenze
- Keller, J., (1980). The island of Vulcano. *Rend Soc. Geol. It Miner. E Petrol.*, 36 (1), 369-414.
- Kokelaar, P. And Romagnoli, C., (1995). Sector collapse, sedimentation and clast population evolution at an active island-arc volcano: Stromboli, Italy. *Bull. Volc.*, 57, 240-262.
- Krcho, J., (1973). Morphometric analysis of relief on the basis of geometric aspect of field theory. *Acta UC, Geogr. Physica*, 1, Bratislava, SPN.
- Krcho, J., (1991). Georelief as a subsystem of landscape and the influence of morphometric parameters of georelief on spatial differentiation of landscapeecological processes. *Ecology /CSFR/*, 10, 115-157.
- Mark, D.M., (1975). Computer analysis of topography: a comparison of terrain storage methods. *Geografiska Annaler*, 57 (A), 179-188.
- Mark, R.K. and Ellen, S.D., (1995). Statistical and simulation models for mapping debris-flow hazard. In: (Carrara A. and Guzzetti F., ed.), *Geographical information systems in assessing natural hazards*. Amsterdam, Kluwer Academic, 93-106 pp.
- Meentemeyer, R.K. and Moody, A., (2000). Automated mapping of conformity between topographic and geological surfaces. *Computers & Geosciences*, 26 (7), 815-829.
- Minár, J., (1998). Georelief and geoecological mapping in large scales. PhD thesis, Dept. of physical geography and geoecology, Faculty of Natural sciences, Comenius University, Bratislava in Slovak.
- Mitasova, H., (1993). Interpolation by Regularized Spline with Tension: II. Application to Terrain Modeling and Surface Geometry Analysis. *Mathematical Geology*, 25, (6), 657-669.  
<http://www2.gis.uiuc.edu:2280/modviz/papers/hmg.rev1.ps>
- Mizukoshi, H. And Aniya, M., (2002). Use of Contour-Based DEMs for Deriving and Mapping Topographic Attributes. *Photogramm. Engin. And Remote Sensing*, 68, (1), 83-93.
- Moore, I.D., Grayson, R.B. and Ladson, A.R., (1991). Digital terrain modelling: a review of hydrological, geomorphological and biological applications. *Hydrol. Processes*, 5, 3-30.
- Moore, I.D., Grayson, R.B. and Ladson, A.R., (1993). Digital Terrain Modelling: a review of hydrological, geomorphological, and biological applications. *Hydrological Processes*, 5, 3-30.
- Muller, S., Helava, U. V. and Devenecia, K., (1995). Softcopy photogrammetric work-station. *Photogrammetric Engineering and Remote Sensing*, 61, 49-56.
- Neri, G., Montalto, A., Patanè, D. and Privitera, E., (1991). Earthquake space-time magnitudo pattern at Aeolian Islands (Southern Italy) and implications for the volcanic surveillance of Vulcano. *Acta Volc.*, 1, 163-169.
- Nogami, M. *Geomorphometric Measures For Digital Elevation Models*. [Http://www.lapgis.chs.nihon-u.ac.jp/nogami/Measures.html](http://www.lapgis.chs.nihon-u.ac.jp/nogami/Measures.html)
- Onorati, G., Pascolieri, M., Ventura, R., Chiarini, V. and Crucillà, U., (1992). The digital elevation

- model of Italy for geomorphology and structural geology. *Catena*, 19, 147-178
- Peschier, J., (1996). Characterisation of Topographic Surfaces on a Triangulated Irregular Network (TIN) <http://www.jarno.demon.nl/gavh.htm>
- Pike, R.J., (1988). The geometric signature-quantifying landslide-terrain types from digital elevation models. *Mathematical Geology*, 20, 491-511
- Pike, R.J., (1993). A bibliography of geomorphometry. Technical report., US Geological survey, Menlo park, California. Open-file report 93-262-A.
- Pike, R. J., (1995). Geomorphometry-progress, practice and prospect. *Zeitschrift fur Geomorphologie/Supplementband, Advances in geomorphometry*, 10, 221-239.
- Pike, R.J., (1998). Web resources compiled for terrain modeling in Eos. *Transactions, American Geophysical Union, Electronic Supplement*. [http://www.agu.org/eos\\_elec](http://www.agu.org/eos_elec).
- Pike R. J., (2000). Geomorphometry–diversity in quantitative surface analysis. *Progress in Physical Geography*, 24 (1), 1-20.
- Rasà, R. and Villari, L., (1988). Geomorphological and morpho-structural investigations on La Fossa Cone. *Acta Vulcanologia*, 1, 127-133.
- Speight, J. G., (1974). A parametric approach to landforms regions. Technical Report 7, Institute of British Geographers, 213-230.
- Tinti, S., Bortolucci, E. and Artigliato, A., (1999). Numerical simulation of the landslide-induced tsunami of 1988 in Vulcano Island, Italy. *Bull. Volc.*, 61, 121-137.
- Unbenannt, M., (1998). Ableitung Und Bewertung Morphometrischer Parameter ausgewählter Hangsegmente im Cottonwood Canyon, Colorado, USA mit Hilfe Digitaler Höhenmodelle. Unpublished Diploma Thesis, Department of Geography, Martin-Luther-University Halle-Wittenberg.
- Unbenannt, M., (1999). Generation and analysis of high-resolution digital elevation models for morphometric relief classification, represented at a cuesta scarp slope on the Colorado Plateau, USA. DFG research project “Hangformensequenzen als Zeugen klimatischen Wandels auf dem Colorado-Plateau, USA”.
- Van Westen, C.J., (1993). Application of Geographic Information System to landslide hazard zonation. ITC-Publication n° 15, ITC, Enschede, 245 pp.
- Weibel, R. and Brandli, M., (1995). Adaptive methods for the refinement of digital terrain models for geomorphometric applications. *Zeitschrift fur Geomorphologie*, N.F., Supplemental Band, 101, 13-30.
- Wise, S.M., (1998). The effect of GIS interpolation errors on the use of digital elevation models in geomorphology. *Landform monitoring, Modelling and Analysis* (S.N. Lane, K.S. Richards and J.H. Chandler, editors), John Wiley and Sons, New York, 139-164 pp.
- Wood, J., (1996). The geomorphological characterisation of digital elevation models. PhD thesis, Department of geography, University of Leicester, Leicester, UK.
- Zevenbergen, L.W. and Thorne, C., (1987). Quantitative analysis of land surface topography. *Earth Surface Processes and Landforms*, 12, 47–56.
- Zhang, X., Drake, N.A., Wainwright, J. and Mulligan, M., (1999). Comparison Of Slope Estimates From Low Resolution Dems: Scaling Issues And A Fractal Method For Their Solution. *Earth Surface Processes and Landforms*, 24, 763-779.
- Zomer, R., Ustin, S. and Ives, J., (2002). Using satellite remote sensing for DEM extraction in complex mountainous terrain: landscape analysis of the Makalu Barun National Park of eastern Nepal. *International Journal of Remote Sensing*, 23 (1), 125-143.

**Analysis of lava flows thermal characteristics by using short wavelength infrared data acquired by spaceborne and airborne sensors: time series of images acquired on Mt. Etna between 1984 and 2001**

Lombardo V., Buongiorno M.F.

Istituto Nazionale di Geofisica e Vulcanologia  
Via di Vigna Murata, 605; 00143, Roma, Italy.  
Tel: +39-06-51860508,  
lombardo@ingv.it, buongiorno@ingv.it

**Abstract**

Short-wave infrared (SWIR) channels acquired by airborne and spaceborne sensors have allowed the characterization of the thermal structure of lava. In this study we assumed the Crisp and Baloga model [1990] to be suitable for Etnean lavas. Thus, we have applied the dual-band technique to retrieve the temperature of the crust, the temperature of the hot cracks and the extension of their relative radiating areas. This work also wants to compare solutions obtained by different sensor datasets. The comparison between spaceborne and airborne sensors allowed us to validate the dual-band technique and suggests further instrumental improvements for next sensors generation. In particular SWIR and TIR channels with a good dynamic range are necessary to solve the dual-band equation system in three components (triple-band) as we observed by means of MIVIS data.

**Introduction**

The thermal model proposed by Crisp and Baloga [1990] for active lava flows considers the thermal flux as a function of the fractional area of two thermally distinct radiant surfaces. Within this model, the larger surface area corresponds to the cooler crust of the flow and the other, much smaller area to fractures in the crust. These cracks are at much higher temperatures than the crust and are closer to the temperature of the molten or plastic flow interior. Interior temperatures for active lava flows are typically about a factor 2-4 higher than that of the crust. Issuing from this model, we use the dual-band technique to retrieve the crust temperature and the hot cracks fractional area for Etnean active lava flows, using satellite short-

wave infrared (SWIR) imagery.

The INGV Remote Sensing Group carries out researches based on optical imaging systems to study active volcanic areas since 1992. The Remote Sensing Group participated to several airborne campaigns with image spectrometers to acquire data on interesting volcanic and tectonically active areas [Salvi et al 1992, Bogliolo et al., 1996, Buongiorno et al., 1999].

In this work we investigate thermal properties of active lava flows by analyzing and comparing LANDSAT TM data set acquired over Mt. Etna between 1984 and 2001 and airborne imaging spectrometer data acquired on Etna during 1996 and 2001 airborne campaigns. In particular the 2001 eruptive event of Mt. Etna gave the opportunity to acquire contemporaneously a large number of optical sensor data both from satellite (ASTER, LANDSAT ETM+, MODIS, HYPERION) and aircraft (MIVIS) useful to compare the sensor performances and validate remote sensing algorithm used to analyze the thermal features of active lava flows. Finally the hyperspectral data were used to define the requirements to observe volcanic phenomena that could be used to develop the next generation of satellite sensors.

**1. Sub-Pixel Temperature Retrieval**

The spectral radiance detected by the sensor is related to the kinetic temperature T by means of the Planck function:

$$R(\lambda) = \frac{\epsilon C_1}{\lambda^5 \pi (\exp(C_2/\lambda T_c) - 1)} \quad \text{Eq. 1}$$

where  $\epsilon$  is the spectral emissivity, estimated by means of sample spectra,  $\lambda$  is the wavelength,  $T_c$  is the crust temperature, and the constants  $C_1$  and  $C_2$  have values  $3.74151 \text{ E-16} [\text{W m}^2]$  and  $1.4388 \text{ E-2} [\text{m K}]$ , respectively. If the target is thermally homogeneous at the scale of the pixel (e.g. the fluid portion of a lava flow at the vent) temperature can be retrieved directly from the Planck equation (fig. 1a). If two distinct temperatures,  $T_h$  and  $T_c$ , characterized by strongly different values (fig. 1b), represent a radiant pixel, the radiance detected by the sensor in one band would be an average, weighted by the fractional area, of the two radiances related to the different temperatures:

$$R_{\text{tot}}\lambda = f_h (R_h\lambda) + (1 - f_h) R_c\lambda \quad \text{Eq. 2}$$

where  $R_{\text{tot}}\lambda$  is the total radiance detected by

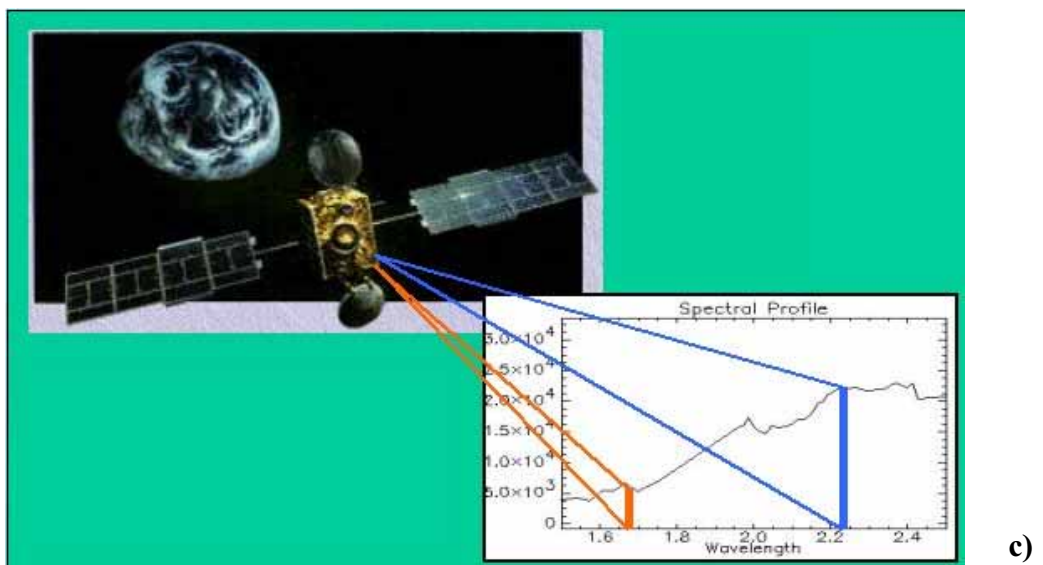
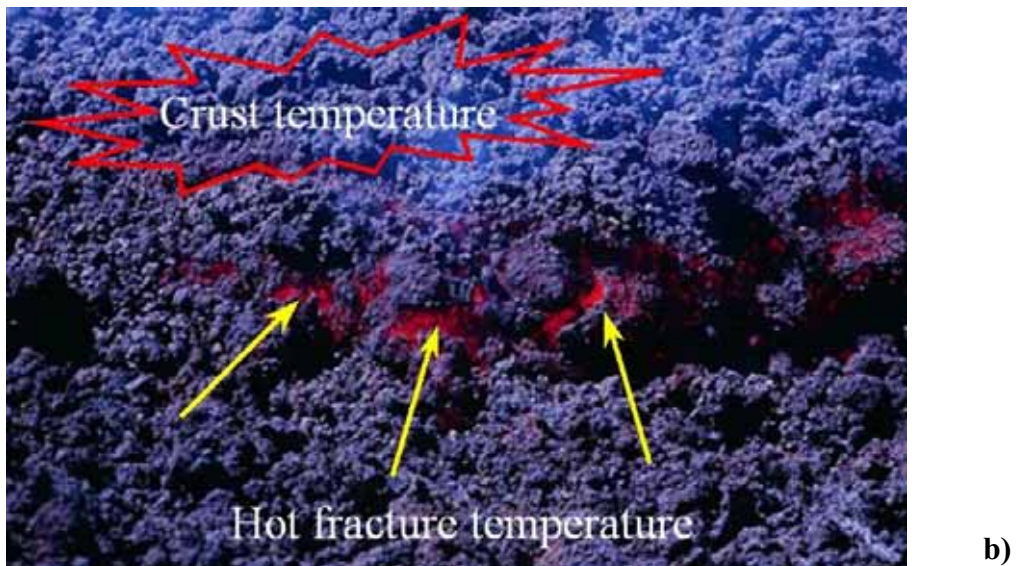
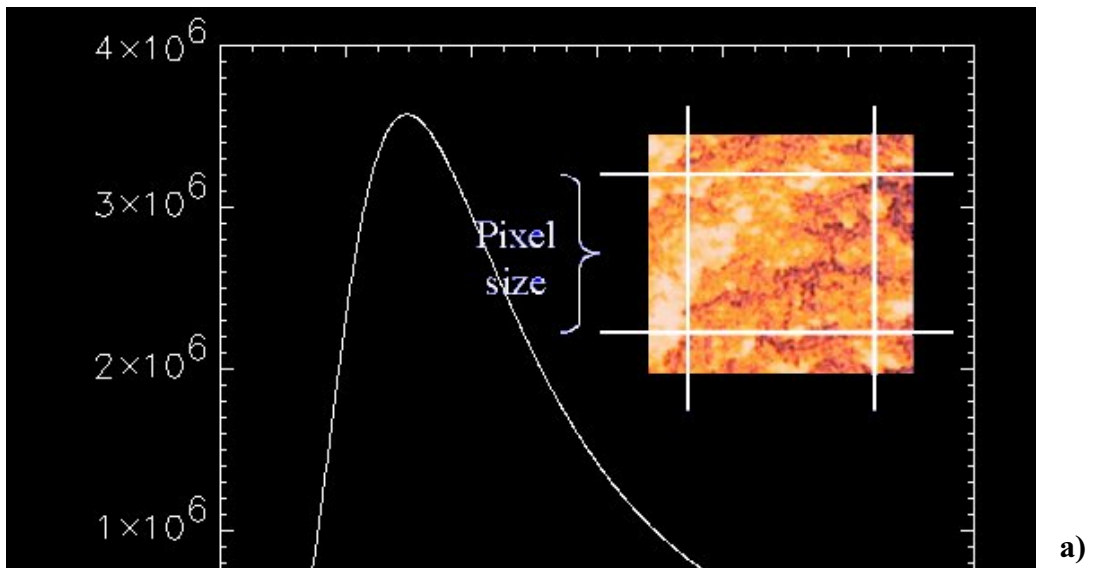


**Figure 1** Flying path of the MIVIS sensor installed on a CASA aircraft over across Mount Etna during the July 2002 eruptive event.

the sensor at the wavelength  $\lambda$ ,  $R_h \lambda$  and  $R_c \lambda$  are the radiances associated to the higher ( $T_h$ ) and lower ( $T_c$ ) temperature contribution, and  $f_h$  is the fractional area of the hot component. Following the Crisp and Baloga [1990] thermal model, we assume the energy flux of the Etnean lava flows as a function of the fractional area of two thermally distinct radiant surfaces. The largest surface corresponds to the coolest crust of the flow, whilst the much smaller area is related to the hot fractures in the crust (fig1b). The dual band technique allows the calculation of the crust temperature ( $T_c$ ) and the fractional area ( $f_h$ ) of the lava flow hot cracks. This method requires the availability of a sensor with two bands within the short wave infrared (SWIR) region of the spectrum (fig. 1c) to calculate the ‘sub-pixel’ temperature of the lower and hot fractions [Dozier, J., 1981; Matson, M. and Dozier J., 1981, Wan Z., Dozier J., 1989]. The dual band equation system can be summarized as follow:

$$\begin{cases} R_{\text{Tot}} \lambda_1 = f_h (R_h \lambda_1) + (1 - f_h) R_c \lambda_1 \\ R_{\text{Tot}} \lambda_2 = f_h (R_h \lambda_2) + (1 - f_h) R_c \lambda_2 \end{cases} \quad \text{Eq. 3}$$

$\lambda_1$  and  $\lambda_2$  indicate the wavelengths of the two bands.

In this system,  $T_c$ ,  $T_h$ , and  $f_h$  represent the three unknown quantities. We assume a value for one of these quantities a priori in order to solve the equation system. The relatively con-

stant inner-core temperature along the whole length of the flow as well as the low heat capacity and very low thermal diffusivity values for Etna lavas suggest that we assume  $T_h$  as boundary condition. Measurements of solidus temperatures [BGVN 24:06, 06/99; BGVN 21:07, 07/96; Calvari et al., 1994, Archambault & Tanguy, 1976; Gauthier, 1973] permit us to assume  $T_h$  equal to 1080°C.

## 2. Hot-Cracks Frequency Distribution

Dual-band technique has been successfully applied by several authors [Dozier, J, 1981; Pieri et al., 1990, Oppenheimer, C, 1991; Oppenheimer et al., C, 1993; Harris et al., 1999; Flynn et al., 2001; Wright et al., 2001] to estimate the surface thermal structure of aa and pohoehoe [Flynn et al, 1994] lava-flows. Following Rothery et al. [1988], Oppenheimer [1991], Flynn et al. [1994], Harris et al. [1998], we apply this two components model using Landsat Thematic Mapper (TM) Bands 5 (1.55-1.75  $\mu\text{m}$ ) and 7 (2.08-2.35  $\mu\text{m}$ ) to solve a system of simultaneous equations 3).

When the dual band system equation is performed on a lava flow, a logarithmic distribution is obtained by plotting  $f_h$  versus  $T_c$ . This trend is observed for a time series of Landsat TM images, when the statistics of the dual band solution highlighted a common behavior for

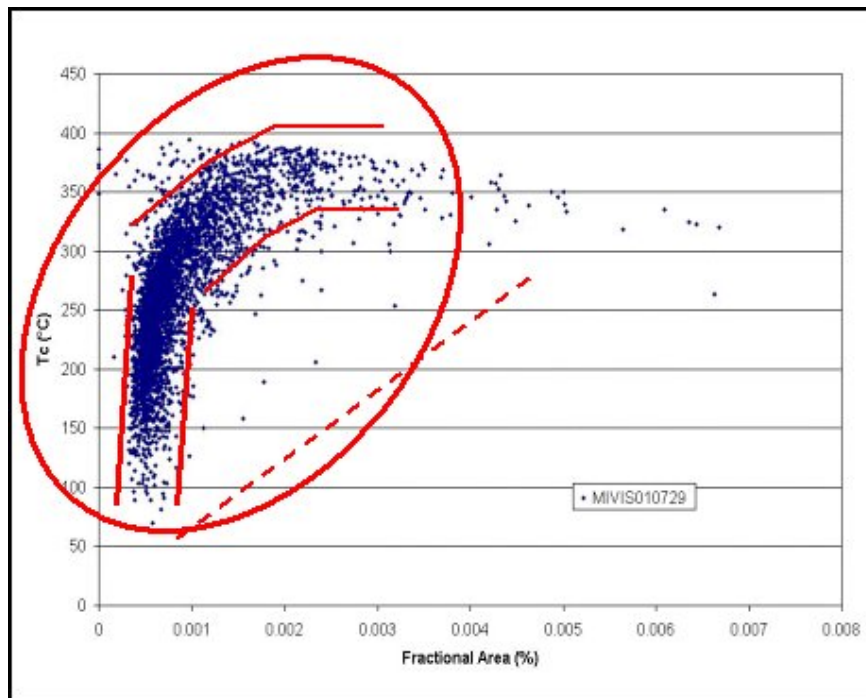


**Figure 2** Geocoded RGB (54,28,13) MIVIS bands; average pixel size is 8x8 m.

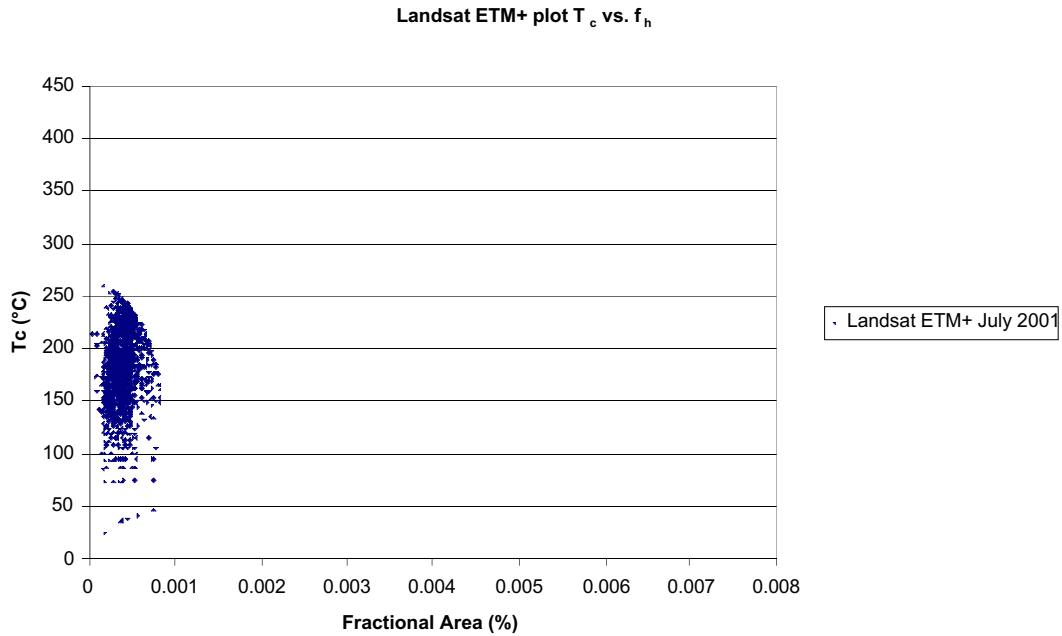


**Figure 3** a) Principal components transformation on the MIVIS thermal infrared bands and integrated temperature mapping of the lava flows. b) Crust temperature distribution retrieved by using the dual-band technique. c) Energy flux calculated for the radiant pixels.

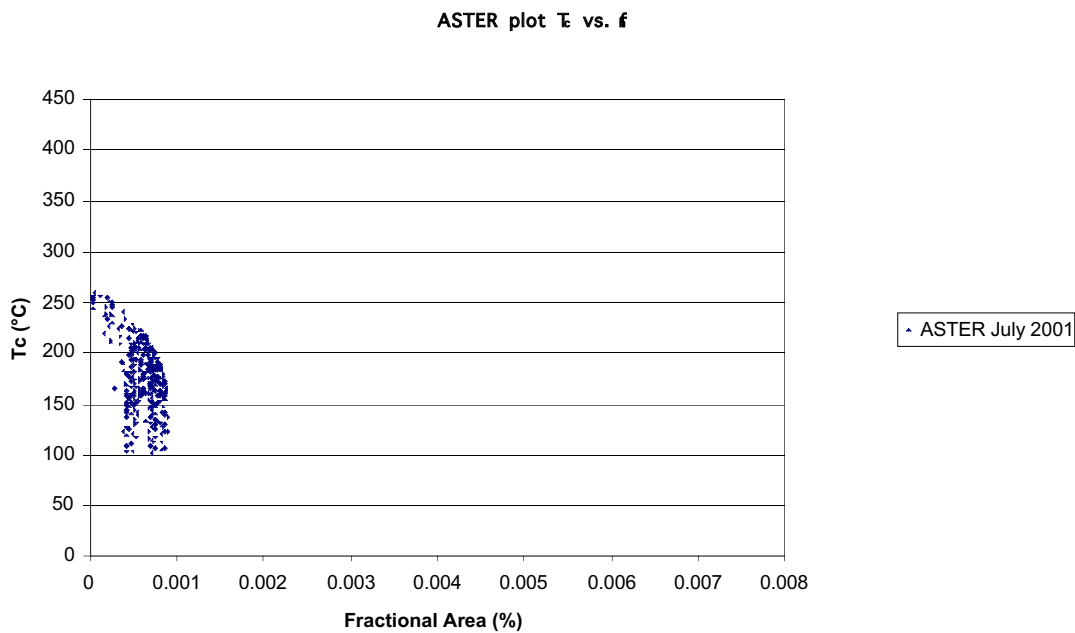


**Figure 4** Energy flux contribution of the distinct active lava flows on 29<sup>th</sup> July 2001.

many distinct eruptive events (fig. 3). This relationship has been supported thanks to the use of a high resolution imaging spectrometer characterized by a wide dynamic range of 15 bits (DAIS 7915) and 12 bits (MIVIS). Such features permit an extended analysis on a large

number of unsaturated samples and return results statistically significant. Fig.2 shows a typical trend for a lava-flow imaged by the MIVIS sensor. Some consideration can be drawn:

1. The non-saturated pixels are not randomly

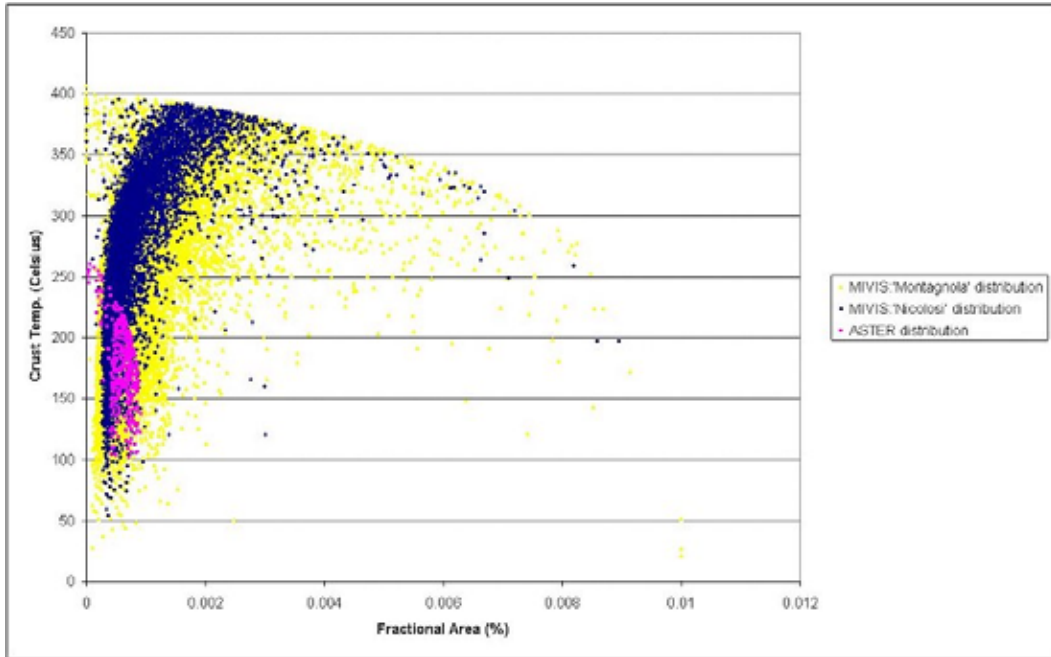


**Figure 5** Effective recorded surface according to different pixel-sizes due to topographic variations.

- distributed, but mainly fall into a well-determined field.
2. This field seems to vary within a narrow range for crust temperature values less than 200 C°
  3. for temperature values greater than 200 C° the pixels distribution tends to bow toward higher values of the fractional area
  4. no points occur below an hypothetical oblique line delimiting the lower-left area of the dis-

tribution.

The shape of this particular fracture distribution is probably related to fluid mechanical aspects of flow emplacement that affect flow velocity and flow heat loss and thus the rate of formation of the surface crust. Here, we use frequency distribution analyses to compare different instruments potentialities.

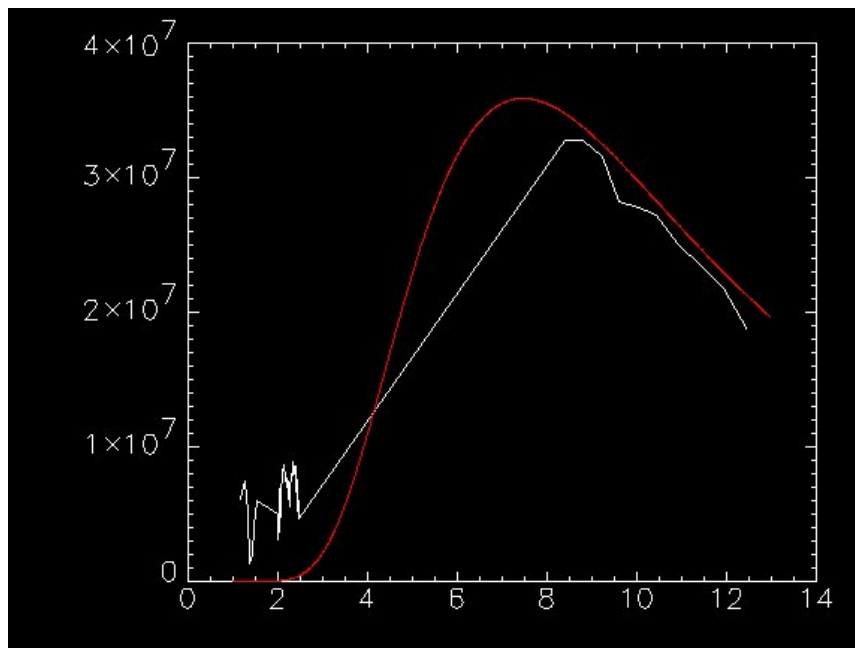


**Figure 5** Effective recorded surface according to different pixel-sizes due to topographic variations.

Sensor	Spatial Resolution	Spec. Channels	Spec. Coverage		Spec.	Details	
<b>ASTER</b>		15	0.52 - 11.65	Bands	lower limit	upper limit	
				#	µm	µm	
	VIS = 15			1	0.52	0.60	
				2	0.63	0.69	
				3	0.76	0.86	
				3B	0.76	0.86	
	SWIR = 30			4	1.60	1.70	
				5	2.145	2.185	
				6	2.185	2.235	
				7	2.235	2.285	
				8	2.295	2.365	
				9	2.360	2.243	
	TIR = 90			10	8.125	8.475	
				11	8.475	8.825	
				12	8.925	9.275	
				13	10.250	10.950	
				14	10.950	11.650	
<b>Landsat ETM+</b>		8	0.45 - 12.50	Bands	lower limit	upper limit	
				#	µm	µm	
	VIS = 30			1	0.45	0.52	
	VIS = 30			2	0.53	0.61	
	VIS = 30			3	0.63	0.69	
	NIR = 30			4	0.78	0.90	
	SWIR = 30			5	1.55	1.75	
	TIR = 90			6	10.40	12.50	
	SWIR = 30			7	2.09	2.35	
	NIR = 30			8	0.52	0.90	
<b>MIVIS</b>	DoFA	102	0.43-12.70 µm	Bands	Lower edge	Upper edge	Bandwidth
				#	µm	µm	µm
				01-28	0.43	0.83	0.02
				21-28	1.15	1.55	0.05
				29-92	1.983	2.478	0.009
				93-102	8.18	12.7	0.34-0.54

**Table 1** a) MIVIS sensor technical details and b) related spectral range.

### 3. Multi-Sensors Comparison

MIVIS sensor is equipped with 72 bands into the range 1.175 µ – 2.473 µ that are potential input in the dual band calculation, and a spatial resolution between 3 and 12 m according to the flight altitude (table 1). It has been tested that band at 1.525 µ and 2.188 µ are the most

performing channels in the dual-band algorithm, therefore they have been chosen for the temperature calculation. These bands were also selected as close as possible to the corresponding two SWIR bands of the Landsat TM and ASTER (1.65 µ and 2.22 µ respectively) to allow a multi-sensor comparison of the retrieved parameters (table 2). The number of radiant pixels

available to perform the dual band system equation, and thus the calculation of  $T_c$  and  $f_h$ , is larger for MIVIS. This is due to its better spatial resolution (Landsat TM is 30 m) and its dynamic range (12 bits versus Landsat TM's 8 bits). Thus, the logarithmic trend observed from the Landsat imagery (fig. 3) is much more evident in the plot derived from MIVIS images (fig. 2). On July 29<sup>th</sup> also ASTER sensor acquired over Mount Etna. The plot  $T_c$  vs.  $f_h$  derived from ASTER data is shown in fig 4. ASTER 8 bits encoding explains why  $T_c$  and  $f_h$  exhibit a range of solutions considerable restricted than MIVIS one (fig 5).

## References

- Archambault, C., and Tanguy, J.C., (1976). Comparative temperature measurements on Mount Etna lavas: problems and techniques. *Journal of Volcanology and Geothermal Research* 1, 113-125.
- Bogliolo M.P., Buongiorno M.F., Salvi S., Teggi S., Pugnaghi S., Abrams M.J., Pieri D.C., Realmuto V.J., Caltabiano, (1996). Ground measurements of physical parameters at Vulcano island and Mount Etna in support of the MIVIS remote sensing campaign "Sicilia-94", Pubblicazione ING 577.
- Buongiorno, M.F., Merucci, L., Doumaz, F., Salvi, S., Bogliolo, M.P., Pugnaghi, S., Teggi, S., Coradini, S., Lombroso, L., Sterni, A., Caltabiano, T. and Carrere, (1999). MVRRS Campaign: MIVIS mission on Sicilian volcanoes and ground measurements. *Quaderni di Geofisica*, Pubblicazione N. 7, 1999, editor: Istituto Nazionale di Geofisica
- Calvari, S., Coltelli, M., Neri, M., Pompilio, M., Scribano, V., (1994). The 1991-1993 Etna eruption: chronology and geological observations. *Acta Vulcanologica* V. 4, 1994, 1-14.
- Crisp, J. and Baloga, S., (1990). A model for lava flows with two thermal components, *J. Geophys. Res.*, 95, 1255-1270.
- Dozier, J., (1981). A method for satellite identification of surface temperature fields of subpixel resolution. *Remote Sensing Environment*, 11:221-229.
- Flynn, L. P., Harris, A.J.L., Wright, R., (2001). Improved identification of volcanic features using Landsat 7 ETM+, *Remote Sensing Environment*, 78:180-193.
- Flynn, L. P., Mouginis-Mark, P. J. and Horton, K. A., (1994). Distribution of thermal areas on an active lava flow field: Landsat observations of Kilauea, Hawaii, July 1991, *Bull. Vulcanol.* 56, 284-296.
- Flynn, L. P., Mouginis-Mark, P. J., (1994). Temperature of an active lava channel from spectral measurements, Kilauea volcano, Hawaii, *Bull. Vulcanol.* 56, 297-301.
- Gauthier, F., (1973). Field and laboratory studies of the rheology of Mount Etna lava, *Philos. Trans. R. Soc. London*, 274, 83-98.
- Global Volcanism Network (GVN), Etna, Smithsonian. *Inst. Bull. Global Volcan. Network*, 06/99 (BGVN 24:06), 1999.
- Global Volcanism Network (GVN), Etna, Smithsonian. *Inst. Bull. Global Volcan. Network*, 07/96 (BGVN 21:07), 1996.
- Harris, A.J.L., Flynn L.P., Rothery D.A., Oppenheimer C. & Sherman S.B., 1999, Mass flux measurements at active lava lakes: implications for magma recycling, *Journal of Geophysical Research*, 104, 7117-7136.
- Harris, A.J.L., Flynn, L.P., Keszthelyi, L., Mouginis-Mark, P.J., Rowland, S.K., and Resing, J.A., (1998). Calculation of lava effusion rates from Landsat TM data, *Bull. Vulcanol.* 60, 52-71.
- Matson, M. and Dozier J., (1981). Identification of subresolution high temperature sources using a thermal IR sensor. *Photogramm. Eng. Remote Sens.*, 47(9):1311-1318.
- Oppenheimer, C., (1993). Thermal distributions of hot volcanic surfaces constrained using three infrared bands of remote sensing data, *Geophysical research letters*, vol.20, no.6, 431-434.
- Oppenheimer, C., (1991). Lava flow cooling estimated from Landsat Thematic Mapper infrared data: The Lonquimay eruption (Chile, 1989), *Journal of Geophysical Research* 96, 21865-21878.
- Pieri, D.C., Glaze, L.S., Abrams, M.J., (1990). Thermal radiance observation of an active lava flow during the June 1984 eruption of Mt. Etna, *Geology*, v.18, p. 1018-1022.
- Rothery, D.A., Francis, P.W. and Wood, C.A., (1988). Volcano monitoring using short wavelength infrared data from satellite, *J. Geophys. Res.*, 93, 7993-8008.
- Salvi, S., Bogliolo, M.P., Ferrari, M.C., Sgavetti, M., Boccolari, M., Campolieti D., Frontero, P., Pugnaghi S., Teggi S. 1992. Ground measurements at the Strait of Messina in support of the Multisensor Airborne Campaign - MAC Europe 1991". ING publication 547, Istituto Nazionale di Geofisica, Rome, Italy
- Tanguy, J.C., (1973). The 1971 Etna eruption: Petrography of lavas, *Philos. Trans. R. Soc. London.*, 274, 45-53.
- Wan, Z., Dozier, J., (1989). Land-surface tempera-

ture measurement from space: physical principles and inverse modelling, *IEEE Transactions on Geoscience and Remote Sensing*, 27(3), 268-277.

Wright, R., Flynn, P.F., Harris, A.J.L., (2001). Evolution of lava flow-fields at Mount Etna, 27-28 October 1999, observed by Landsat 7 ETM+, *Bull. Vulcanol.* 63, 1-7.

## Electromagnetic Characterization of Volcanic Ash

Sandra Costanzo, Giuseppe Di Massa

Dipartimento di Elettronica, Informatica e Sistemistica  
 Università della Calabria  
 87036 Rende (CS), ITALY  
 costanzo@deis.unical.it

### Abstract

An open-ended coaxial probe is designed for making permittivity measurements on volcanic ash. Reference liquids such as water and methanol are used for calibrating the probe, whose input admittance is related to the complex permittivity by Marcuvitz integral. The reflection coefficient of the probe in the presence of volcanic ash samples from Etna volcano, Italy, is measured from 1 to 15 GHz and subsequently processed to retrieve the complex permittivity of the material under test.

### Introduction

The interest for sensing volcanic activity phenomena has increased in the last years as a result of several violent eruptions. Detection of volcanic ash clouds has become an imperative for aviation industry, which suffered high economic costs for repair of equipments damaged by powerful eruptions. Two kinds of remote sensing applications are actually employed for hazard mitigation of volcanic ash. One method senses eruption columns and clouds by meteorological radar systems [Harris et al. 1983], while the other is based on the use of imaging radars for mapping volcanic deposits on the ground [Delene et al. 1996]. A large amount of dielectric data is crucial on a wide range of wavelengths and volcanic ash compositions in order to develop new models and reconstruction algorithms.

In this paper, a method is presented to perform complex permittivity measurements on volcanic ash in a wide microwave frequency band. An open-ended sensor is constructed from a length of semirigid 50  $\Omega$  coaxial line terminated by a large-diameter conductor flange. A proper calibration technique is applied which uses two calibration standards (short and open circuits) together with a reference liquid in order to improve accuracy [Nyshadham et al. 1992].

Measurements of the complex reflection coefficient are performed through a network analyser with the open-ended probe placed against the material under test. Marcuvitz integral for the probe input admittance [Misra et al. 1990] is then applied to retrieve the complex permittivity on ash samples of Etna volcano at microwave frequencies.

### Open-ended coaxial probe

Let us consider the geometry in fig.1, where the open-ended coaxial probe is placed in contact with the material under test. Due to device imperfections, the true reflection coefficient at the reference plane differs from the measured one. It is computed from the knowledge of S-parameters ( $S_{11}$ ,  $S_{22}$ ,  $S_{12}$ ,  $S_{21}$ ) relevant to the equivalent two port network, which in turns are derived from the measured reflection coefficients  $S_i$  in the presence of three standard loads by means of the formula [Nyshadham et al. 1992]:

$$\Gamma_i = \frac{S_i - S_{11}}{S_{21}S_{12} + S_{22}(S_i - S_{11})}, \quad i=1,2,3 \quad (1)$$

where the terms  $\Gamma_i$  are the known reflection coefficients at the reference plane.

Network calibrations are usually performed by short, open and matched terminations. However, this latter condition is very difficult to realize with open-ended sensors, which are calibrated by using good reference liquids such as water and methanol. The dielectric properties of these substances are described by the Cole Cole equation [Nyshadham et al. 1992]:

$$\varepsilon_l = \varepsilon_\infty + \frac{\varepsilon_s - \varepsilon_\infty}{1 + (j\omega\tau)^{1-\alpha}} \quad (2)$$

where  $\varepsilon_\infty$  and  $\varepsilon_s$  are the optical and static permittivity, respectively,  $\tau$  is the relaxation time and  $\alpha$  the distribution parameter. Cole Cole parameters are tabulated for various reference liquids as a function of temperature. A relationship exists between the dielectric properties of the material under test and the input admittance of the coaxial line, as given by Marcuvitz formula [Misra et al. 1990]:

$$Y = G + jB \quad (3)$$

$$G = \frac{Y_o \sqrt{\epsilon}}{\ln\left(\frac{b}{a}\right) \sqrt{\epsilon_c}} \int_0^{\pi/2} \frac{1}{\sin\theta} \left[ J_o\left(k_o \sqrt{\epsilon} b \sin\theta\right) - J_o\left(k_o \sqrt{\epsilon} a \sin\theta\right) \right] d\theta$$

$$B = \frac{Y_o \sqrt{\epsilon}}{\pi \ln\left(\frac{b}{a}\right) \sqrt{\epsilon_c}} \int_0^{\pi} \left[ 2Si\left(k_o \sqrt{\epsilon} \sqrt{a^2 + b^2 - 2ab \cos\theta}\right) - Si\left(2k_o \sqrt{\epsilon} a \sin\left(\frac{\theta}{2}\right)\right) - Si\left(2k_o \sqrt{\epsilon} b \sin\left(\frac{\theta}{2}\right)\right) \right] d\theta$$

In the above expressions,  $a$  and  $b$  are the inner and outer radii of the coaxial line,  $k_o$  is the free-space propagation constant,  $Y_o$  the characteristic admittance of the probe,  $\epsilon$  and  $\epsilon_c$  denote the permittivity of the material under test and the dielectric inside the line, respectively.

Once completed the calibration procedure with short, open and reference liquid terminations, the complex reflection coefficient  $S_M$  can be measured in the presence of the material under test. The true reflection coefficient  $\Gamma_M$  at the reference plane (fig.1) is computed from eq. (1) as:

$$\Gamma_M = \frac{S_M - S_{11}}{S_{21}S_{12} + S_{22}(S_M - S_{11})}$$

The probe admittance is then obtained by the expression:

$$Y_M = Y_o \frac{1 - \Gamma_M}{1 + \Gamma_M}$$

This latter quantity is finally inserted into

eq. (3) for retrieving the unknown complex permittivity  $\epsilon$ .

## Experimental Results

In order to make permittivity measurements on volcanic ash, an open-ended probe of length  $L=28\text{cm}$  has been realized from a  $50\ \Omega$  coaxial line type RS-RG402 with dimensions  $a=0.046\ \text{cm}$ ,  $b=0.1492\ \text{cm}$  and inner dielectric of constant  $\epsilon_c=1.9910$ . The open-ended sensor is terminated in a conductor flange of diameter  $d=3\text{cm}$  (fig.2), which is used to simulate the infinite plane assumption in Marcuvitz formula (3). The correct behaviour of the probe has been tested on water by using methanol as reference liquid. Measurements have been performed on this substance from 1 to 12 GHz and results are shown in figs. 3-4, where the retrieved complex permittivity of water is in good agreement with that given by Cole Cole expression (2). Volcanic ash dielectric data are obtained from the test setup illustrated in fig.5, where compressed ash from Etna volcano are placed against the probe

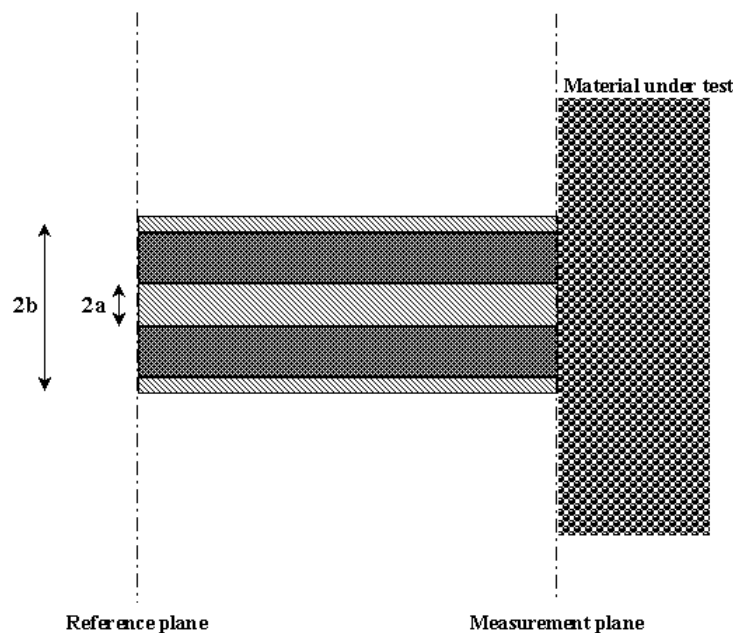


**Figure 1** Open-ended coaxial probe geometry.

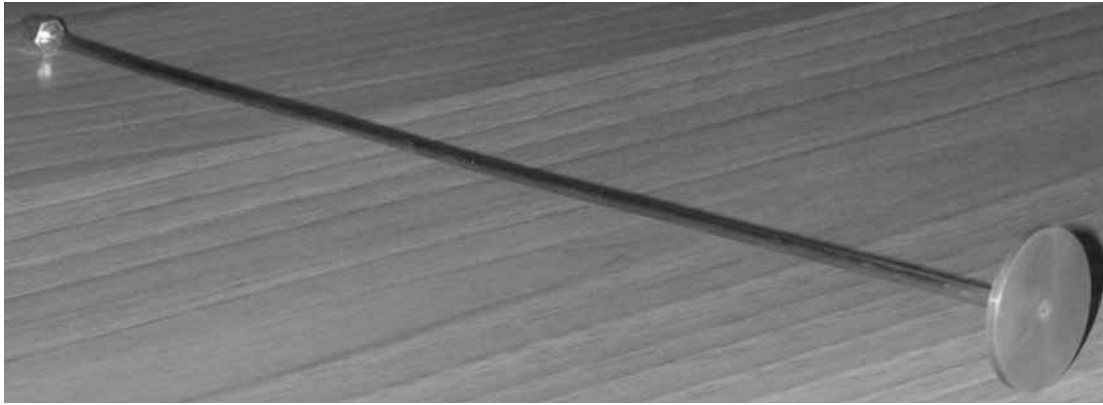


Figure 2 Open-ended sensor terminated with the conductor flange.

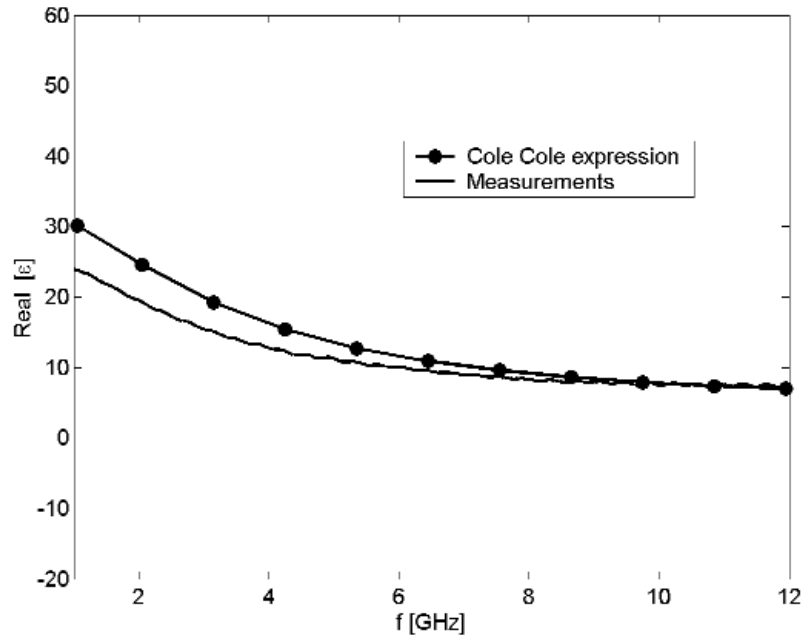


Figure 3 Real part of water permittivity (Methanol as reference liquid).

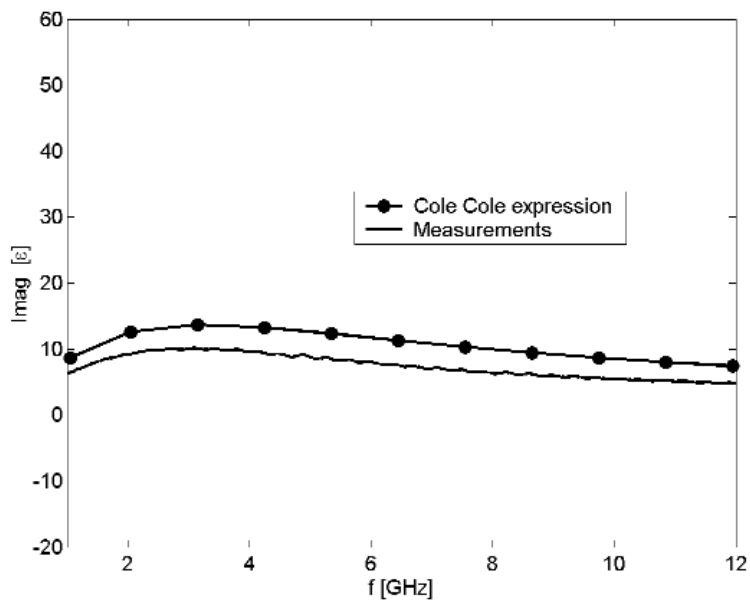
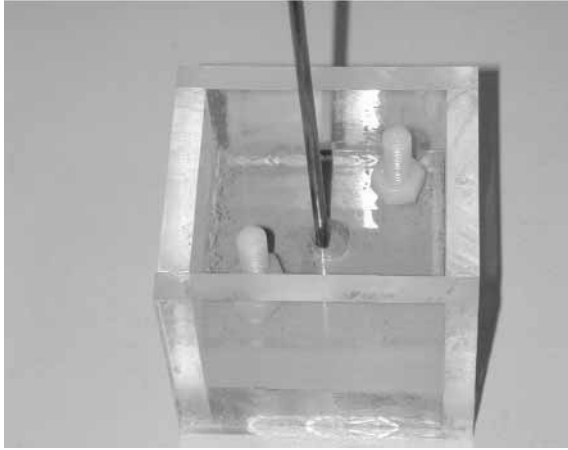


Figure 4 Imaginary part of water permittivity (Methanol as reference liquid).



**Figure 5** Measurement setup for pulverized volcanic ash.

into a plexiglass box. The coaxial probe measurement procedure is then applied to obtain the real and imaginary parts of the complex permittivity, which are reported under figs.6-7.

### Conclusions

Dielectric characterization of volcanic ash is performed by an open-ended coaxial cable technique. Complex permittivity data are retrieved from reflection coefficient measurements on pulverized ash from Etna volcano placed in contact with the open-ended sensor. Measurement uncertainties are significantly reduced by an accurate calibration procedure

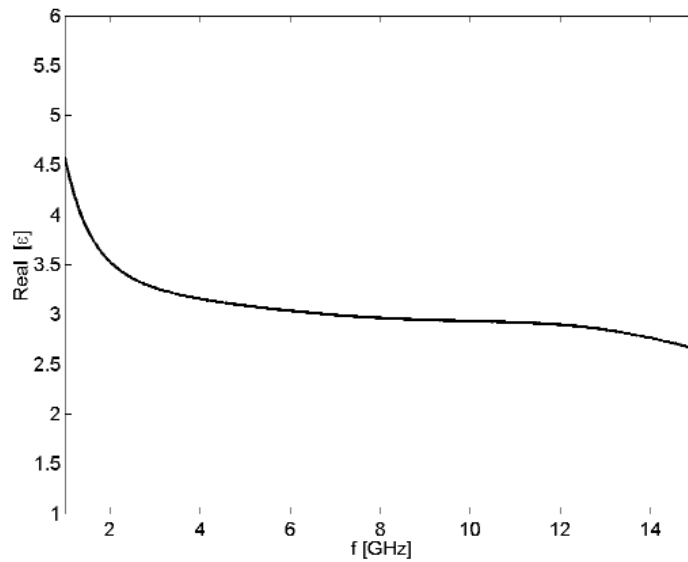


**Figure 6** Real part of Etna volcano ash permittivity (Water as reference liquid).

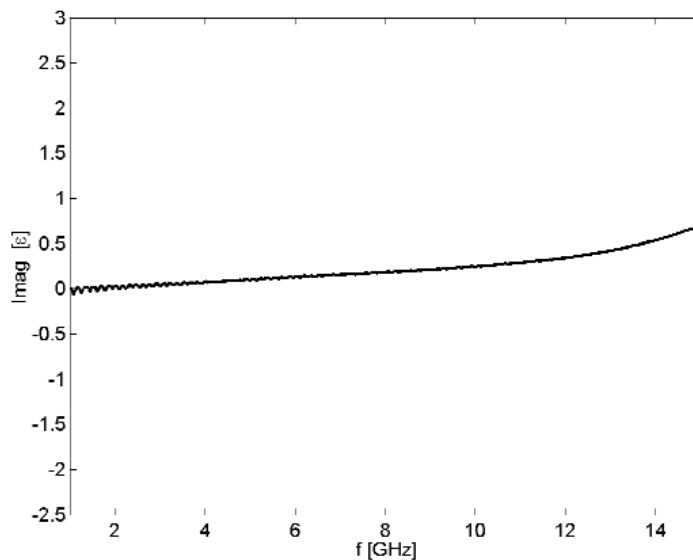


**Figure 7** Imaginary part of Etna volcano ash permittivity (Water as reference liquid).

using a reference liquid as standard with open and short circuits.

## **References**

- Delene, D. J., Rose, W. I. and Grody, N. C., (1996). Remote sensing of volcanic ash clouds using special sensor microwave imager data. *Journal of Geophysical Research*, vol.101, n.B5, May 1996.
- Harris, D. M. and Rose, W. I., (1983). Estimating particle size, concentrations, and total mass of ash in volcanic clouds using weather radar. *Journal of Geophysical Research*, vol.88, n.C15, December 1983.
- Nyshadham, A., Sibbald, C. L. and Stuchly, S. S., (1992). Permittivity measurements using open-ended sensors and reference liquid calibration – an uncertainty analysis. *IEEE Transaction On Microwave Theory and Techniques*, vol.40, n.2, February 1992.
- Misra, D., Chhabra M., Epstein, B. R., Mirotznik, M. and Foster, K. R., (1990). Noninvasive electrical characterization of materials at microwave frequencies using an open-ended coaxial line: test of an improved calibration technique. *IEEE Trans. On Microwave Theory and Techniques*, vol.38, n.1, January 1990.

## Retrieval of tropospheric ash clouds of mt. Etna from AVHRR data

Remitti M<sup>1</sup>, Pugnaghi S.<sup>1</sup>,  
Teggi S.<sup>2</sup>, Parmiggiani F.<sup>3</sup>

<sup>1</sup>Dip. Ingegneria Materiali e Ambiente  
Università di Modena e Reggio Emilia

<sup>2</sup>Dip. Ingegneria Meccanica e Civile  
Università di Modena e Reggio Emilia

<sup>3</sup>ISAC-CNR Bologna

### Abstract

This paper focuses on three eruptive events of the Mt. Etna volcano: July 22nd 1998, April 26th 2000 and the recent eruption of July-August 2001. Such eruptions may be a severe threat to aircraft safety, as in the April 2000 event. From the AVHRR visible images the height of the top of the clouds is estimated, using geometrical methods, knowing both NOAA satellite and Sun positions. The results are then compared with information derived from radio-sounding data etc.. The volcanic ash particles with diameters of 1-10 micron are not detectable by aircraft radar but they may be remotely sensed using thermal infrared data. The well-known algorithm, based on the AVHRR channel 4 and channel 5 brightness temperatures difference [Prata, 1989; Schneider et al. 1994], is here applied to highlight the ash clouds of Mt. Etna volcano. Even though it was

typically used to detect and follow the volcanic clouds of stratospheric eruptions, here it is successfully tested for tropospheric plume too. Some good results of this technique are presented together with some basic problems. This work points out that it could be useful to prepare a procedure to monitor Mt. Etna eruption clouds analysing TIR data. Such a procedure should automatically alert (in real time, using the new Meteosat Second Generation satellite) and indicate the cloud direction on the basis of atmospheric radio-sounded and/or predicted data.

### 1. Introduction

Volcanic ash has various sizes, and different times of residence in atmosphere, mostly depending on particle diameter and altitude reached by the ashes after the eruption. The time of residence of larger particles (radius greater than 100 micron) may be very short (minutes, usually less than an hour), but ashes with radius lower than 10 micron can travel hundreds of kilometres before falling down. Volcanic fallout causes a long list of problems: respiratory problems (for both people and animals), damage to vegetation, agricultural and industrial activities, transport and tourism. In particular, volcanic clouds are a severe threat to aircraft security [Mayberry, 1998]. Very big particles (up to some centimetres) can damage the aircraft structure (windows, wings, ailerons, e.g. the windshields in the April 2000 event) but small particles (less than 10 micron) may be extremely dangerous too. In fact, volcanic fine ash clouds

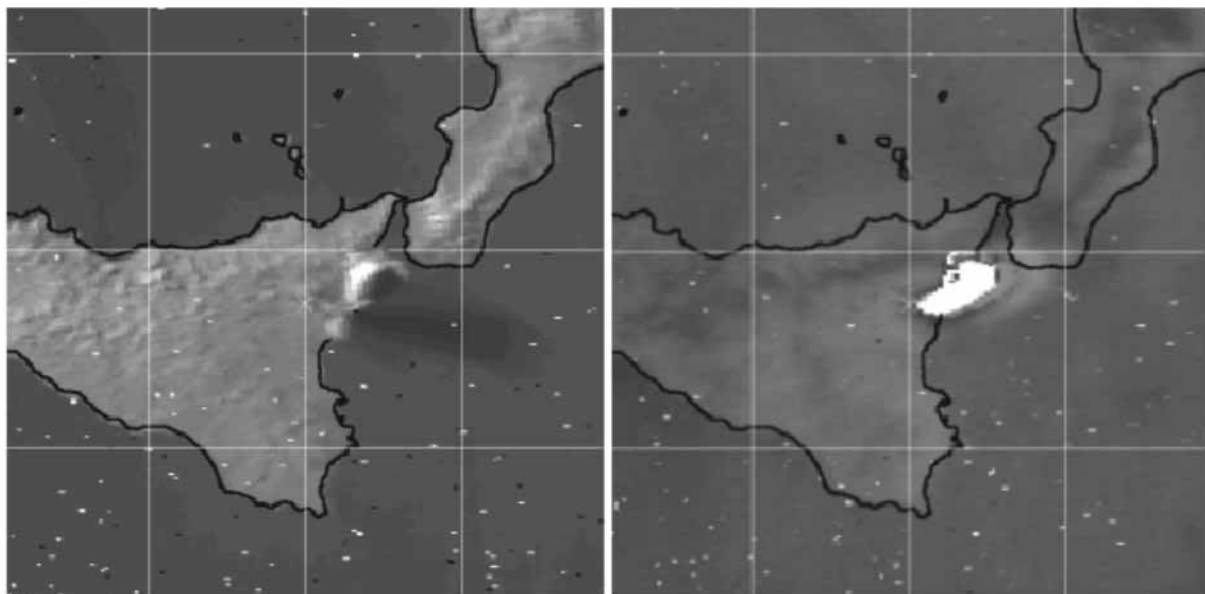


**Figure 1** 22.07.1998 eruption: AVHRR channel 2 (1a, left) and BT-D (1b, right).

can not be detected [Barker, 1990] by aircraft radar (so they are totally undetectable during night or in low visibility flights) and they are often undistinguishable from meteorological ones. Flying inside these clouds causes loss of power and rapid engine stop, due to volcanic ash structure. Volcanic ashes, differently of the sand, are generally described as glassy, with an amorphous disordered structure, and their melting point is low enough that even during the short time they are in hot turbine section melting can take place. High operational temperature of turbo engines tends to create an accumulation of melted ceramic-like deposit on the turbine surfaces, causing airflow reduction, compressor stall and then engine stop [Barker, 1990].

The international airport of Catania (Italy) provided traffic for more than four millions of passengers during year 2000 [SAC, 2002]; it is very close to the top of Mt. Etna volcano (about 30 km) and ash falling down during eruptive events is always dangerous (e.g. the airport was closed for many days during July/August 2001 eruption). The eruptions of Mt. Etna represent a serious problems for the whole air traffic above the Eastern-Central Mediterranean Sea too. This area, crossed by many air routes, is usually the portion interested by the volcanic ash clouds with small particle sizes; in fact, due to the general circulation, the typical wind direction at the volcano top is from North-Northeast.

Ground observations are not sufficient to organically monitor volcanic clouds, and they are exposed to the same problems as aircraft ones (night flights, meteorological clouds); instead, satellite observations represent an useful tool to track ash movements and to prevent planes encountering hazardous particles. A specific procedure, which uses different information, should be prepared. This procedure will have to be an integrated system to take into account: the dimensions of volcanic particulate matter, the altitude of the volcanic cloud, the forecasted dynamic of atmosphere, data from all the available satellites above area and, of course, the different air routes and their altitudes.

In this paper the algorithm based on the channel 4 and channel 5 of the Advanced Very High Resolution Radiometer (AVHRR, aboard NOAA polar orbiting satellites) brightness temperature difference is used. This method, previously tested only on stratospheric eruptions, is here verified for the typically tropospheric eruptions of Mt. Etna volcano. This work focuses on volcanic particles with diameters of

few (1-10) micron only [Watson and Oppenheimer, 2000]. Analysing the Thermal Infrared (TIR) data, related to the three aforementioned Mt. Etna eruptions, some positive results and some problems connected with the volcanic cloud detection are reported. Other informations, derived from sun-satellite relative positions and from atmospheric radio-sounding data, are also included.

## **2. Procedure**

Schneider et al. [Schneider et al. 1994], on the basis of the works of Prata [Prata, 1989], developed a procedure to detect volcanic ash clouds from AVHRR-TIR data [NOAA, 2000]. The proposed algorithm allows to identify volcanic clouds and to discriminate them from meteorological ones.

Starting from AVHRR raw data, the visible (VIS; channel 1: 0.58-0.68  $\mu\text{m}$ ) and the near infrared (NIR; channel 2: 0.725-1.0  $\mu\text{m}$ ) calibrated images (percent albedo), are obtained using a linear relationship determined prior to launch [Lauritson et al. 1979]. The infrared AVHRR data (channel 3: 1.58-1.64  $\mu\text{m}$ ; channel 4: 10.3-11.3  $\mu\text{m}$ ; channel 5: 11.5-12.5  $\mu\text{m}$ ) are converted to radiances with a linear relationship based on the measurements associated with cold space (at about 3 K) and with an onboard black-body (at about 300 K) [Lauritson et al. 1979; NOAA, 2000]; using the inverse Planck function the radiances are then converted to brightness temperatures. Finally, using the Terascan software package [SeaSpace, 2002] and satellite tracking information, images may be rectified, registered and Earth-located.

Schneider et al. state that AVHRR channel 4 minus channel 5 Brightness Temperature Difference (BTD) can be used to detect the volcanic clouds. In fact, eruptive clouds present a negative BTD [Prata, 1989; Schneider et al. 1994; Wen and Rose, 1993; Wen and Rose, 1994; Schneider et al. 1999], while meteorological clouds, as most of the earth's surfaces (water, land, snow, etc.), generally have positive BTD [Yamanouchi et al. 1989].

Due to the larger refractive index for silicates in the channel 4 region than in the channel 5 region, volcanic clouds absorption of energy from the underlying surface is greater in the channel 4 than in the channel 5 [Schneider et al. 1994] and this results in a negative BTD. It can be derived from the following simplified radiative transfer equation:

$$L_i \approx e^{-\tau_i \mu} B(T_s) + (1 - e^{-\tau_i \mu}) B(T_c) \quad (1)$$

where  $L_i$  is radiance at the sensor,  $\tau_i$  is the cloud optical thickness,  $\mu=1/\cos(\theta)$  and  $\theta$  is the viewing angle,  $T_s$  and  $T_c$  are surface and cloud temperatures.

For transparent meteorological clouds, equation (1) gives a positive BTD; for opaque meteorological clouds the radiance measured at the sensor is the cloud emission only and this results again in a positive BTD [Schneider et al. 1994]. For volcanic clouds, the magnitude of the negative brightness temperature difference depends on the optical thickness of the cloud, the amount of water, volcanic ash and sulfuric acid in the cloud, the size of the particles, their size distribution and the temperature contrast between the cloud and the underlying surface (meteorological clouds, land or water) [Prata, 1989; Wen and Rose, 1994]. In great stratospheric eruptions, opaque volcanic clouds can have positive BTD [Schneider et al. 1994; Krotkov, 1999; Kerdiles and Diaz, 1996; Holasek and Rose, 1991], which inhibits discrimination.

### Studied Cases

In this paper images related to three eruptive events are presented: the July 22<sup>nd</sup> 1998, the

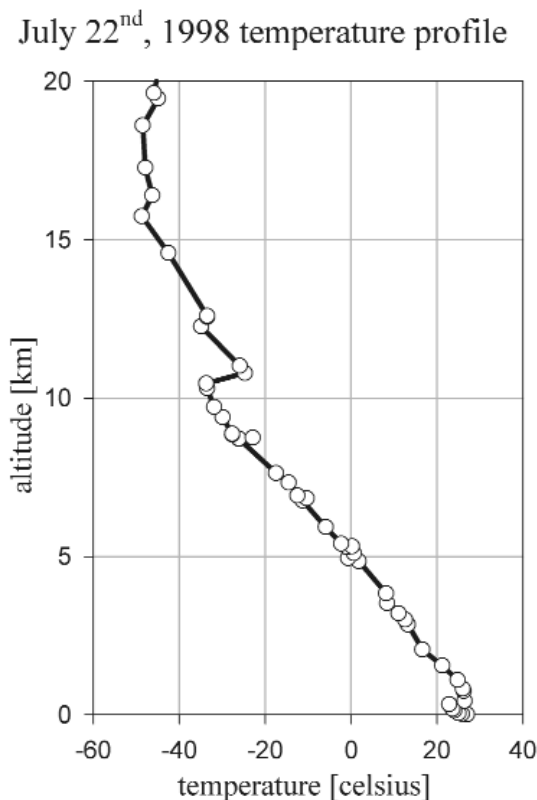


Figure 2 22.07.1998 temp. profile.

April 26<sup>th</sup> 2000 and the recent eruption of July-August 2001.

Mt. Etna volcano erupted many times during the last decade [Behncke, 2002] but only few satellite remotely sensed volcanic cloud images were collected: this is mainly due to the clouds' low altitude, the short time extension of the events and the few polar orbiting satellites passes above the volcano (about two/three passes per day). Most of the eruptions have an altitude lower than 8-10 km and the produced volcanic clouds have a short time of residence in atmosphere (from minutes to a few hours). During the last two years numerous images of Mt. Etna eruptions were collected: this is due to the presence of more than one hundred eruptive events, some of them with significant ash injection in atmosphere, and to the three contemporaneous active NOAA satellites.

In next paragraphs "visible channel" definition will be indifferently used for ch. 1 (VIS) or ch. 2 (NIR), referring to channels that sense mostly Sun radiance reflected by Earth, in opposition to "infrared channels" (ch. 3, ch. 4 and ch. 5, mostly thermal emission).

### JULY 1998

The 22<sup>nd</sup> July 1998 eruption produced a large ash cloud, causing the Catania airport to close and significant ash falling (1 cm at Torre del Filosofo, 1 mm at Catania) in the downwind area (south of the sommital craters, [Behncke, 2002]).

Cloud altitude, which brings information about eruption energy, is estimated measuring the ash cloud shadow. Geometrical study has to consider Sun and satellite positions, Earth curvature, pixel dimensions (depending on column numbers and on earth curvature again) and cloud deformation due to the 2D-image effect. A long (about 100 km) cloud shadow, due to low Sun elevation (the image was taken at 17.28 GMT) can be seen in Fig. 1a. This was an excellent condition to evaluate a cloud top altitude of about 15 km (i.e. a cloud vertical extension of more than 11 km).

Lowest brightness temperature in the plume is about  $-60$  °C; this value is not seen in the vertical profile measured at Trapani (Fig. 2). The difference between the AVHRR thermal map and the atmospheric data is due to the partially adiabatic expansion caused by fast vertical motion [Holasek et al. 1996; Schneider et al. 1999], which can cause the noticed 10 °C difference of temperature.

Fig. 1b shows the BTD map obtained from the TIR AVHRR data for the considered

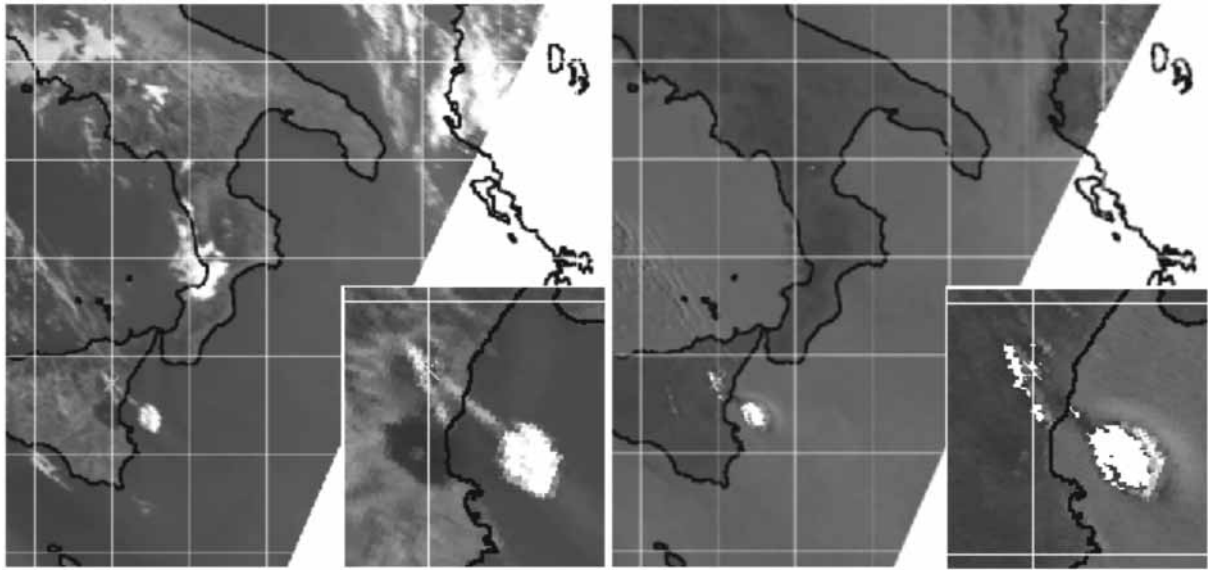


**Figure 3** 26.04.2000 eruption: AVHRR a 2 (3a and 3b) and BTM (3c and 3d).

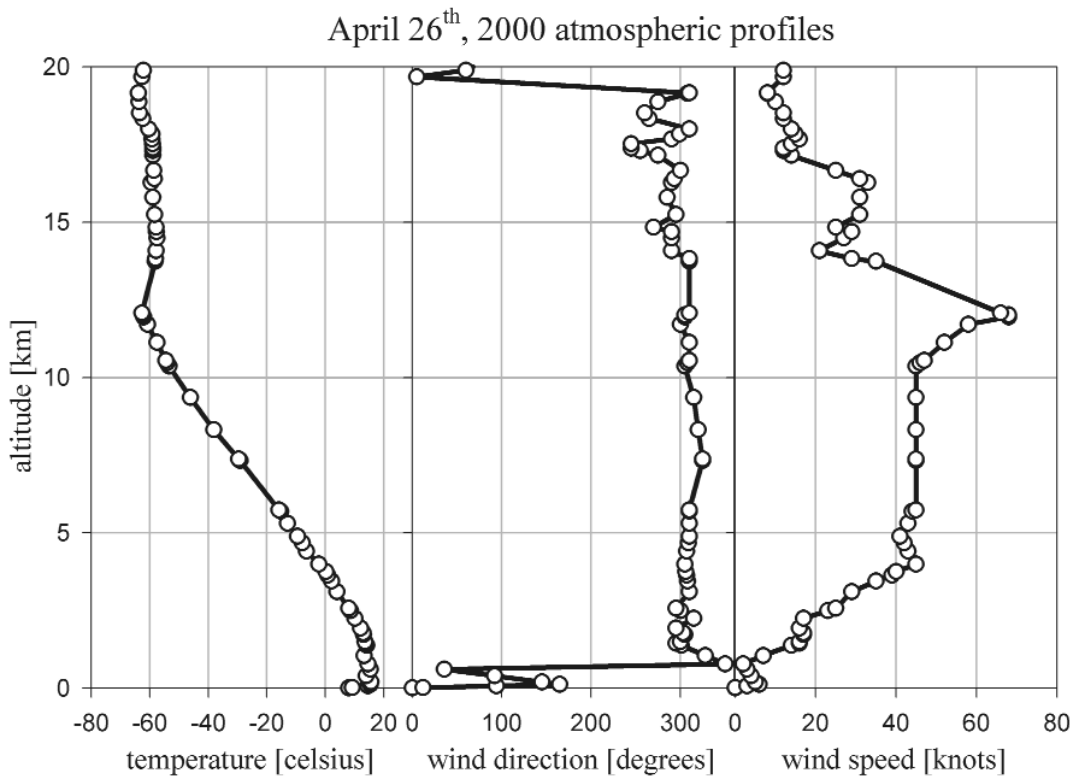


**Figure 4** 26.04.2000 atmospheric profiles.

eruption. The highlighted pixels (white) have negative BTM (most of them have  $BTM < -1^{\circ}C$ ) and entirely identify the volcanic cloud, including close to the craters (identified by the cross) portion of cloud (part not clearly seen in visible image). Non-volcanic pixels show positive values, typically  $BTM > 1^{\circ}C$ .

In Meteosat images from 17.00 to 19.30 GMT the volcanic cloud and its temporal evolution are identifiable, but the spatial resolution is very poor (the image is unusable for detailed location of ashes) and there is no visible shadow.

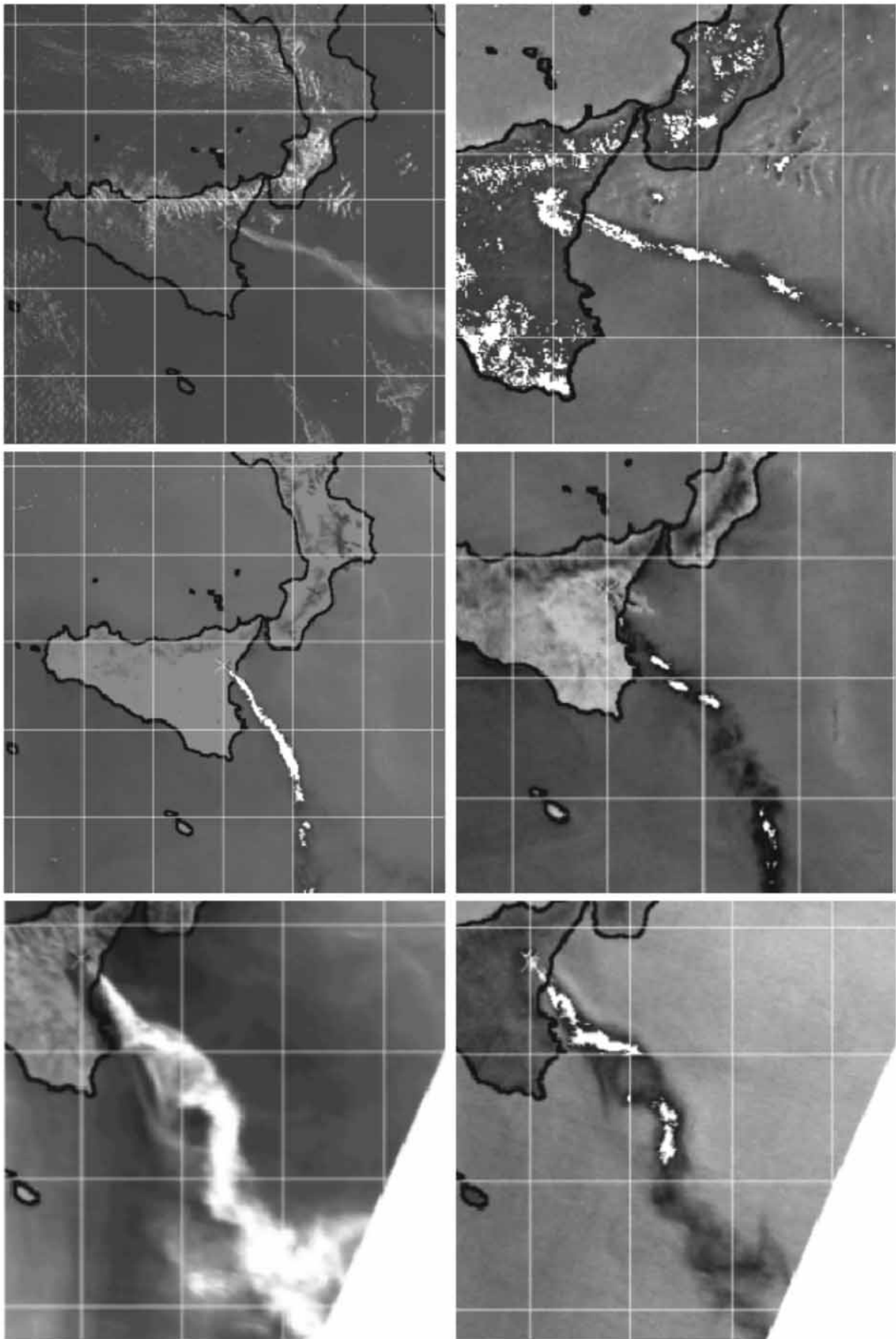


**Figure 5** July 1998 eruption, AVHRR channel 2 (5a and 5e) and BTM (5b, 5c, 5d, 5f).

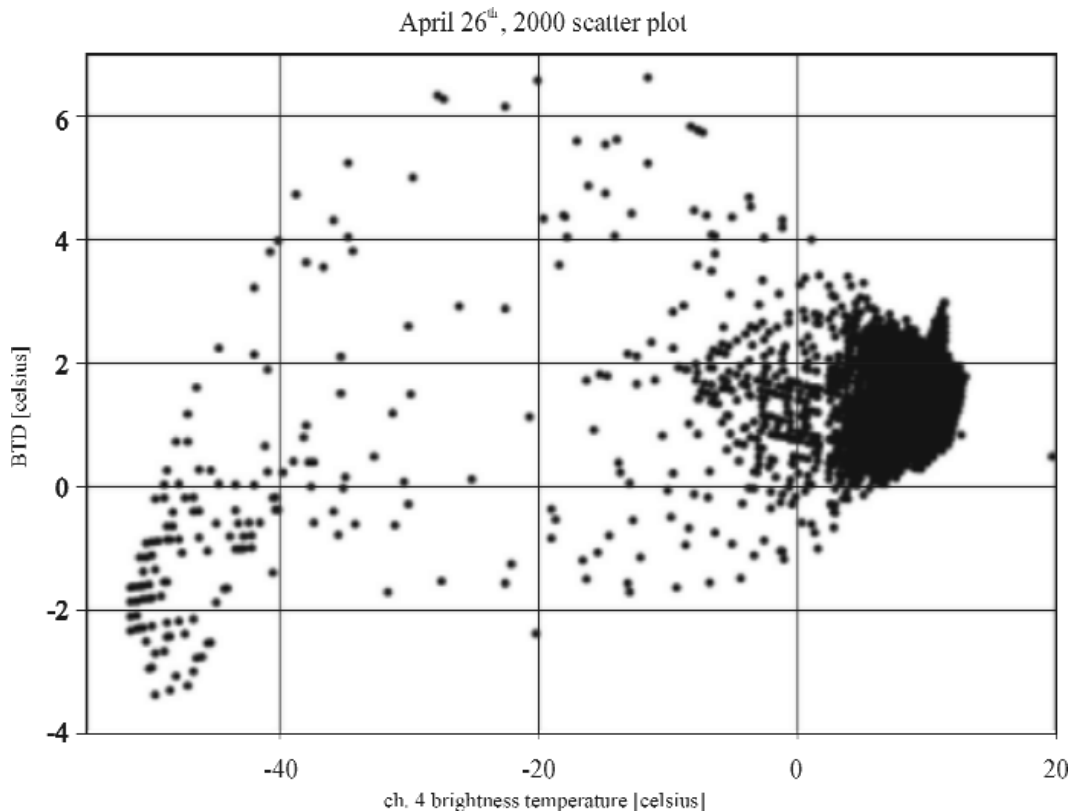


**Figure 6** 26.04.2000 scatter plot.

#### APRIL 2000

The 26<sup>th</sup> April 2000 eruption caused the first accident due to an aircraft encountering Mt. Etna volcanic cloud. Shortly after the end of the main paroxysmal phase an Airbus of the AirEurope company, which had departed from the Fontanarossa international airport of Catania heading to Milano, entered the fallout zone of the plume at an altitude of about 1000 m, receiving windshield and engine damage, and was forced to return immediately to the airport [Behncke, 2002].

In NOAA image (Figs. 3), taken at the same accident time (05.38 GMT), the ash cloud is clearly identified, both in VIS (3a and 3b) and in BTM map (3c and 3d, white pixels have  $BTM < 0$  °C).

BTM procedure seems to work correctly: in fact, besides the volcanic cloud identification, difference values for sea, land and all meteorological clouds in the image (South Tyrrhenian Sea, Apennines, Balkans), are positive, as theoretically forecast.

The cloud top altitude, measured using shadow technique in visible image, results about 8 km. The brightness temperature of the top, derived from the TIR image, results -50 °C, in good agreement between previous value and

temperature profile (Fig. 4a), taking into account of the undercooling.

Wind speed profile data (Figs. 4b and 4c) and space/time evaluation from image (for the central part of cloud about 63 km covered in 45 minutes) are in good reciprocal agreement (wind speed is about 23.5 ms<sup>-1</sup>), and profile direction (wind from NW) matches with image.

#### JULY-AUGUST 2001

From July 18<sup>th</sup> to August 10<sup>th</sup> 2001 Mt. Etna volcano had a strong activity, with unusual and complex eruptions [Behncke, 2002]. The three active NOAA satellites recorded many images, with large plume extension and high quantity of ashes injected in atmosphere, causing long interruptions in Catania airport operations.

In Fig. 5a (image taken July 21<sup>st</sup>, at 04.45 GMT; channel 2) the volcanic plume is clearly visible.

In BTM map (Fig. 5b) derived from TIR (channels 4 and 5) data, most volcanic cloud pixels are identified (white area in Fig. 5b), but also some land pixels show negative BTM: this is a typical effect noticed using images remotely sensed during night or early morning (i.e. with low solar heating).

In Fig. 5c (image taken July 23<sup>rd</sup>, at 12.42 GMT) volcanic cloud pixels are correctly identified using difference procedure (white area has negative BTM), even though in VIS channels (not shown) the plume is transparent and not very well defined. In the bottom part of the image there is a plume split: TIROS Operational Vertical Sounder (TOVS) elaboration, used to determine wind direction, give an approximate height of about 3 km for the larger part of the plume (south heading, high ash contents) and a height of about 5 km for the smaller component (south-east heading, high transparency, probably gaseous plume); this result is in good agreement with DWD air masses modelling [DWD, 2001].

In Fig. 5d (image taken July 23<sup>rd</sup>, at 15.18 GMT, after an eruption characterized by successive explosions) only some parts of the plume have a negative BTM (white pixels). There is no information to verify if positive BTM pixels of the plume are gaseous (not containing ash) or if it is a procedure failure [Simpson et al. 2000]: in the algorithm works correctly, the plume is describable as a series of ash clouds inserted in continuous gas emission.

In figures 5e and 5f (image taken July 24<sup>th</sup>, at 05.19 GMT) the volcanic plume is clearly seen in visible channels (Fig. 5e) and partially detected by BTM map (Fig. 5f). Once again the BTM procedure alone results insufficient to completely describe the volcanic emissions.

## Conclusions

In this preliminary work the analysis of three Mt. Etna eruptive events is reported.

The altitude of the volcanic cloud top is estimated using different methodologies (shadow geometry, brightness temperature, radiosoundings data and TOVS elaborations) resulting in good reciprocal agreement. The brightness temperature difference (BTM) algorithm, previously used by Schneider et al. to study stratospheric eruptions (as Mt. Spurr [Kroktov et al. 1999] or Redoubt [Schneider and Rose, 1994] ones) is here applied to the Mt. Etna plumes. Some positive results of this procedure have been presented together with some basic problems.

Algorithm good working for tropospheric plumes is a significant results, even if, in some cases, the BTM is lightly negative or even positive (in particular in presence of 5-10  $\mu\text{m}$  particles size). Fig. 6 shows the April 23<sup>rd</sup> 2000 scatter plot, computed using the channel 4 bright-

ness temperature (x-axis) and the BTM (y-axis). The plume pixels are characterized by lowest values both in BTM ( $-3.5 < y < 0$  °C) and channel 4 ( $-55 < x < 30$  °C), and these values suggest that mainly particles of about 3-5  $\mu\text{m}$  are present [Wen and Rose, 1993].

In some images volcanic clouds detection procedure is ineffective, with most volcanic pixel having positive BTM, particularly in low temperature contrast (winter or night eruptions, low altitude eruptions) or in high presence of large particles cases; in other images, negative BTM does not correspond to volcanic pixels, erroneously highlighting land during night or some meteorological clouds.

AVHRR radiometers aboard NOAA polar orbiting satellites provide very good images, but they are obviously unsuitable for a real time monitoring of volcanic eruption clouds. On the other hand active geostationary satellite (Meteosat) has a poor geometrical resolution and only one channel in the (8-14  $\mu\text{m}$ ) atmospheric window. The new European geostationary satellite (MSG, Meteosat Second Generation), will have two thermal infrared channels (at 10.8 and 12.0  $\mu\text{m}$ ), suitable for previously described integrated procedure application, and will provide, each 15 minutes, images with a spatial resolution of 1 km. Therefore SEVIRI radiometer aboard MSG seems to be an ideal instrument to monitor, detect and track Mt. Etna volcanic ash clouds [ESA, 2002].

## References

- Ackerman, S. A., (1997). Remote sensing aerosols using satellite infrared observations. *Journal of Geophysical Research*, 102-14, pp. 17069-17079.
- Barker, M., (1990). Aviation and the effects of Volcano Ash. url: <http://www.nw.faa.gov/releases/volash.html>.
- Behncke, B., (2002). Etna decade volcano, Sicily. url: <http://www.geo.mtu.edu/~boris/ETNA.html>.
- DWD, (2001). Quarterly Report of the Operational NWP-Models of the Deutscher Wetterdienst, 27. url: [www.dwd.de](http://www.dwd.de).
- ESA, (2002). MSG satellite. url: <http://www.esa.int/msg/home.html>.
- Holasek, R. E., Self, S. and Woods, A. W. (1996). Satellite observations and interpretation of the 1991 Mount Pinatubo eruption plumes. *Journal of Geophysical Research*, 101-12, pp. 27635-27655.
- Holasek, R.E. and Rose, W.I., (1991). Anatomy of

- 1986 Augustine Volcano eruptions as recorded by multispectral image processing of digital AVHRR weather satellite data. *Bulletin of Volcanology*, 53, pp. 420-435.
- Kerdiles, H. and Diaz, R. (1996). Mapping of the volcanic ashes from the 1991 Hudson eruption using NOAA-AVHRR data. *International Journal of Remote Sensing*, 17-11, pp. 1981-1995.
- Krotkov, N. A., Torres, O., Seftor, C., Krueger, A. J., Kostinski, A., Rose, W. I., Bluth, G. J. S., Schneider, D. J., and Schaefer, S. J., (1999). Comparison of TOMS and AVHRR volcanic ash retrievals from the August 1992 eruption of Mt. Spurr. *Geophysical Research Letters*, 26-4, pp. 455-458.
- Lauritson, L., Nelson, G. J., Porto, F. W., (1979). Data extraction and calibration of TIROS-N/NOAA radiometers. NOAA Technical Memorandum NESS 107.
- Mayberry, G. C., (1998). Volcanic and ash clouds and aircraft safety. url: <http://www.seaspace.com>.
- NOAA, (2000). NOAA KLM user's guide. url: <http://perigee.ncdc.noaa.gov/docs/klm/index.htm>.
- Prata, A. J., (1989). Infrared radiative transfer calculation for volcanic ash clouds. *Geophysical Research Letters*, 11-16, pp. 1293-1296.
- Prata, A. J., (1989). Observations of volcanic ash clouds in the 10-12 m window using AVHRR/2 data. *International Journal of Remote Sensing*, 10, 751-761.
- SAC, (2002). Aeroporto Fontanarossa. url: <http://www.aeroporto.catania.it>.
- Schneider, D. J., Rose, W. I., Coke, L. R., Bluth, G. J. S., Sprod, I. E. and Krueger, A. J., (1999). Early evolution of a stratospheric volcanic eruption cloud as observed with TOMS and AVHRR. *Geophysical Research Letters*, 104-4, pp. 4037-4050.
- Schneider, D. J., Delene, D. J., Rose, W. I. and Wen, S., (1994). Remote sensing of volcanic eruption clouds using AVHRR. url: <http://www.geo.mtu.edu/volcanoes/research/avhrr/>
- Schneider, D.J. and W.I. Rose, (1994). Observations of the 1989-90 Redoubt Volcano eruption clouds using AVHRR satellite imagery. In: *Proceedings of the First International Symposium on Volcanic Ash and Aviation Safety*, U.S. Geological Survey Bulletin 2047, pp. 405-418.
- SeaSpace, (2002). Terascan online help. url: <http://www.seaspace.com>.
- Simpson, J. J., Hufford, G., Pieri, D. and Berg, J., (2000). Failures in detecting volcanic ash from a satellite-based technique. *Remote Sensing Environment*, 72, pp. 192-217.
- Watson, I. M. and Oppenheimer, C., (2000). Particle size distributions of Mount Etna's aerosol plume constrained by Sun photometry, *Journal of Geophysical Research*, 105-8, pp. 9823-9829.
- Wen, S. and Rose, W. I., (1993). Retrieval of sizes and total masses of particles in volcanic clouds using AVHRR infrared band. url: [http://www.geo.mtu.edu/volcanoes/research/avhrr/rad\\_transfer](http://www.geo.mtu.edu/volcanoes/research/avhrr/rad_transfer).
- Wen, S. and Rose, W. I., (1994). Retrieval of sizes and total masses of particles in volcanic clouds using AVHRR bands 4 and 5. *Journal of Geophysical Research*, 3-99, pp. 5421-5431.
- Yamanouchi, T., Suzuki, K. and Kawaguchi, S., [1989] Detection of clouds in Antarctica from infrared multispectral data of AVHRR. *Journal of the Meteorological Society of Japan*, 65, pp. 949-962.

## Estimation of the SO<sub>2</sub> flux of the eruption plume of the Mt. Etna volcano using MIVIS and ASTER data

<sup>1</sup>Pugnaghi Sergio, <sup>2</sup>Teggi Sergio, <sup>1</sup>Corradini Stefano,  
<sup>1</sup>Medici Pietro, <sup>1</sup>Lombroso Luca

<sup>1</sup>Dip. Ingegneria Materiali e Ambiente  
Università di Modena e Reggio Emilia

<sup>2</sup>Dip. Ingegneria Meccanica e Civile  
Università di Modena e Reggio Emilia

### Abstract

In this paper two procedures to estimate the SO<sub>2</sub> flux emitted from Mt. Etna volcano are shortly described. These procedures are based on the atmospheric simulations performed using MODTRAN 3.5 radiative transfer code. The first procedure, named *LUT-procedure* [see Teggi et al. 1999], inverts the radiative transfer equation minimizing the square differences of the experimental and simulated radiances at the sensor. The second procedure is based on the *Split-Window* technique (i.e. it uses two bands with different absorption characteristics). The Split-Window permits a direct (and fast) determination of the SO<sub>2</sub> columnar abundance of the volcanic plume, but at least two of the four parameters of the algorithm depend on the state of the atmosphere (temperature and precipitable water). Considering four years of radio soundings carried out at midday at Trapani WMO station, a seasonal trend of the above mentioned parameters have been obtained. The quoted procedures have been applied to aircraft (MIVIS) and spacecraft (ASTER) remotely sensed images and the SO<sub>2</sub> abundance maps have been obtained; for ASTER data the shown results are quite preliminary. Knowing the wind speed at the craters altitude the SO<sub>2</sub> flux has been also computed.

### 1. Introduction

Volcanic eruptions emit large amounts of sulfurous gas and fine ash particles into the atmosphere; this changes the worldwide climate affecting the atmosphere composition and the energy balance of the Earth. According to Rose (1977) the dominant component of a volcanic aerosol is particles of acid; mainly sulfur dioxide (SO<sub>2</sub>), which rapidly converts to sulfuric acid. Volcanic aerosols partly screen the Earth's surface from sunlight, leading to worldwide

cooling [Duaton and Christy, 1992]. Again sulfuric acid droplets can catalyze the chemical reactions that destroy ozone; the effect of the 1991 Mt Pinatubo eruption on the 1992 ozone "hole" over Antarctica [Bhartia et al., 1993] has been seen. Carbon dioxide (CO<sub>2</sub>) is one of the most important greenhouse gases and the volcanic contribution should be accounted for. For example, Mt Etna (Italy) is currently the leading source of CO<sub>2</sub> [Allard et al., 1991].

Volcanic emissions are not limited to eruption events. Stoiber et al. (1987) suggested that at least 6.8 million tones/year of sulfur were produced by volcanoes which are actively degassing but non-eruptive. The knowledge of the SO<sub>2</sub> emission is important because in many cases it is used as a reference [Francis et al., 1998; Ferrara et al., 2000] to estimate other gases. Volcanic gases are important indicators of magmatic processes and it has been seen that the trend of the flux of the SO<sub>2</sub> volcanic emission may be used to predict volcanic eruptions [Caltabiano et al., 1994]. Nowadays remote techniques are used to measure volcanic gas emission [Francis et al., 1998]. One remote technique, COSPEC [Caltabiano and Romano, 1988], is widely used to estimate the emission rate of sulfur dioxide.

One of the objectives of the European Project *Mitigation of Volcanic Risk by Remote Sensing (MVRRS) techniques*, led by Peter Francis, was the estimation of the SO<sub>2</sub> columnar abundance from the Thermal Infrared (TIR) remotely sensed data.

In this paper the results obtained analyzing the Multispectral Infrared and Visible Imaging Spectrometer (MIVIS) [Bianchi et al., 1996] data, taken during the *Sicily-97* campaign (deployed during the MVRRS project activities), will be shown. The preliminary results derived from a TIR image remotely sensed by the Advanced Spaceborne Thermal Emission and Reflection Radiometer (ASTER) [Yamaguchi et al., 1998; Abrams, 2000] aboard Terra satellite will be also shown.

### 2. MIVIS and ASTER radiometers

During the *Sicily-97* campaign [Buongiorno et al., 1999], deployed from 11 to 17 June 1997, the MIVIS images were taken at about 10.00 (local standard time). The MIVIS [Bianchi et al., 1996] sensor has four spectrometers and a total of 102 bands. The first spectrometer (VIS) has 20 channels in the range of 0.431-0.833 μm, the second (NIR) has 8 chan-

nels in the range of 1.150-1.550  $\mu\text{m}$ , the third (SWIR) has 64 channels in the range of 1.985-2.479  $\mu\text{m}$  and the fourth (TIR) has 10 channels in the range of 8.21-14.70  $\mu\text{m}$ . The spectral response functions of the filters are known and the weighted average wavelengths of the ten TIR channels used in this work are reported in Table 1. The first three channels (93, 94, 95) in Table 1 are affected by  $\text{SO}_2$  absorption/emission. The MIVIS has an instantaneous field of view of 2 mrad but the detector signals are sampled every 1.64 mrad along the scan. The total field of view, corresponding to 755 pixels, is  $\pm 35.55$  degrees. During the campaign the MIVIS altitude was around 6000 m asl; the geometric resolution at the surface (2000-3000 m asl) was better than 10 m/pixel.

Terra, the first Earth Observing System satellite, launched on December 18, 1999, is a quasi-polar and sun-synchronous satellite orbiting at about 705 km from the Earth surface with 16 days mapping cycle. ASTER [Abrams, 2000] is one of the Terra instruments that will acquire high-resolution images. ASTER has a total of fourteen channels: three in the visible and near infrared (VNIR: 0.52-0.86  $\mu\text{m}$ ), six in the short-wave infrared (SWIR: 1.60-2.43  $\mu\text{m}$ ) and five in the thermal infrared (TIR: 8.125-11.65  $\mu\text{m}$ ) regions. The field of view is 2.44 degrees corresponding to 60 km swath width; the instantaneous field of view (IFOV), in the TIR channels at nadir, is 127.8  $\mu\text{rad}$ , which means a ground resolution of about 90 m. The VNIR and SWIR channels have a ground resolution of about 15 and 30 m respectively. The spectral response functions of the filters are known and the weighted average wavelengths of the five TIR channels used in this work are reported in Table 2.

### 3. Inversion procedures

The first approach to try to estimate Mt. Etna  $\text{SO}_2$  emission by means of the MODTRAN code were made using the Thermal Infrared

Multispectral Scanner (TIMS) data [Realmuto et al., 1994]. The second approach was performed using the data remotely sensed during the first (July 1994) MIVIS flight [Teggi et al., 1999]. Realmuto et al. [1997] carried out their tests on Kilauea Volcano, Hawaii too.

Sulfur dioxide has absorption/emission bands in the portion (about 8.3-9.3  $\mu\text{m}$ ) of the atmospheric window. The presence of these bands permits to detect the  $\text{SO}_2$  plume of Mt. Etna volcano and also to quantitatively estimate its abundance. Figure 1 shows the effect of a volcanic plume, located at 3300 m asl, 100 m thick and with a constant  $\text{SO}_2$  abundance of 10 ( $\text{g m}^{-2}$ ), on the transmittance of the atmospheric layer 0-6000 m asl (i.e. from sea surface to MIVIS altitude). The gray curve is without plume while the black one was obtained assuming the aforementioned plume. The radio sounding data measured at Trapani (WMO station 16429) on 29<sup>th</sup> July 2001 at 12:00 GMT were inputted in MODTRAN 3.5 radiative transfer code to compute the two mentioned curves. The five spectral functions reported in figure 1 are the normalized response functions of the five ASTER-TIR channels. Clearly the second channel is that mostly affected by  $\text{SO}_2$  and the fourth and the fifth channels are completely transparent to  $\text{SO}_2$ .

#### 3.1 LUT-procedure

In the framework of the MVRRS Project was developed a semi-automatic procedure to invert the radiative transfer equation (1). The inversion is based on a series of Look-Up Tables (LUTs) containing the results of the simulations performed using MODTRAN 3.5 code.

$$L = [\varepsilon \cdot B(T_s) + (1 - \varepsilon) \cdot L_d] \cdot \tau + L_u \quad (1)$$

$L$  is the spectral radiance at the sensor;  $\varepsilon$  is the spectral surface emissivity;  $B(T_s)$  is the Planck function at the surface temperature  $T_s$ ;  $L_d$  is the atmospheric down-welling flux reflected

Channel	93	94	95	96	97	98	99	100	101	102
$\lambda$ ( $\mu\text{m}$ )	8.38	8.74	9.17	9.56	10.01	10.42	10.92	11.41	11.89	12.41

**Table 1** MIVIS TIR channels: weighted average wavelengths.

Channel	10	11	12	13	14
$\lambda$ ( $\mu\text{m}$ )	8.29	8.64	9.08	10.66	11.29

**Table 2** ASTER TIR channels: weighted average wavelengths.

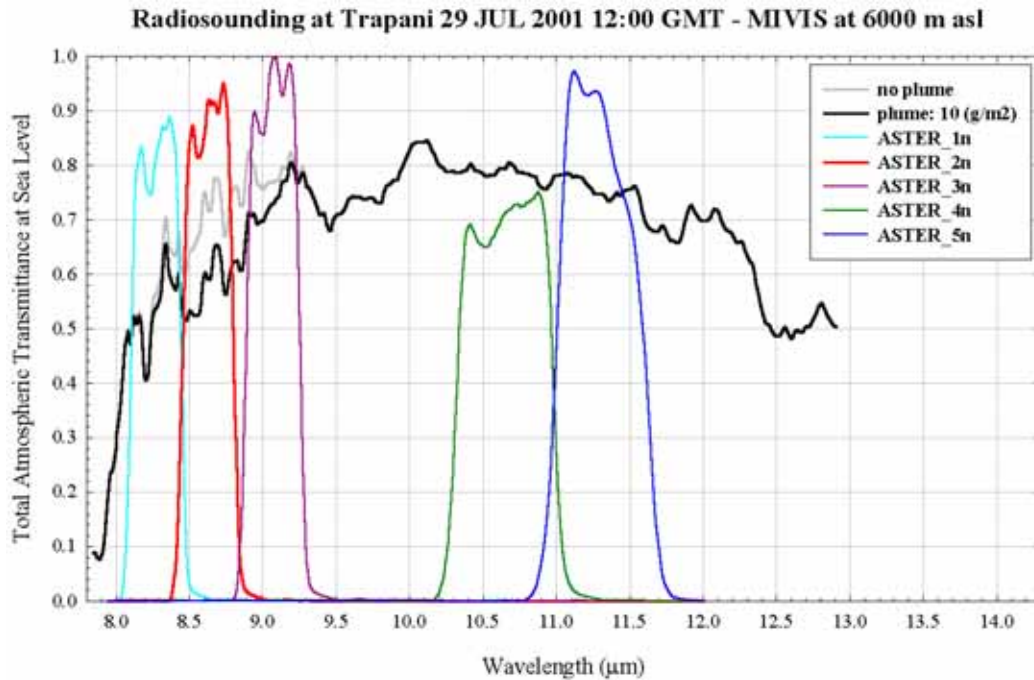


**Figure 1** Gray curve is the transmittance of the layer (0-6000 m) of atmosphere in the 8-14  $\mu\text{m}$  atmospheric window; the black one is the same but with the presence of an  $\text{SO}_2$  plume of  $10 \text{ g m}^{-2}$  located at 3300 m asl and 100 m thick. The other curves are the spectral response functions of the ASTER-TIR channels.

from the surface;  $\tau$  is the atmospheric transmittance from the surface to the sensor;  $L_u$  is the upwelling atmospheric radiance towards the sensor (path radiance).

Each LUT contains the simulated values of the three atmospheric terms of the radiative transfer equation (1): atmospheric transmittance, down-welling irradiance and path radiance. These tables were derived using the measured atmospheric vertical profiles; that is a set of tables for each MIVIS flight was computed. The simulations performed to compute the values of the atmospheric terms of the LUTs take into account different plume geometries and  $\text{SO}_2$  abundances and all the possible geometries between the surface pixel and the radiometer MIVIS. In particular were considered three different plume geometries (laminar, ground based and ground based with the top at constant altitude) and 31  $\text{SO}_2$  abundances in the range 0-15 ( $\text{g m}^{-2}$ ) at steps of 0.5 ( $\text{g m}^{-2}$ ). The pixel-radiometer geometries incorporate 23 pixel altitudes (1000-3200 m asl, step 100 m) and 9 viewing angles (0-40 degrees, at steps of 5 degrees).

The *LUT-procedure* determines the  $\text{SO}_2$  abundance at each pixel of each TIR MIVIS image using the LUTs of the specific flight and performing the following steps:

1. A spectral emissivity map is obtained from

each MIVIS image itself using SNM (Spectrum Normalization Method) [Realmuto, 1990] assuming  $\epsilon_{\text{max}}=0.97$ . To refine the emissivity estimation, the  $\beta$  spectrum and the MMD (Min-Max Difference) method suggested by Gillespie et al. (1998) is used. Since the spectral emissivity cannot be estimated under the plume (the first three channels are affected by  $\text{SO}_2$ ) a mean spectral emissivity, from different top (2000-3000 m asl) areas located outside the plume, is manually derived.

2. Using the last (not affected by  $\text{SO}_2$ ) seven MIVIS channels the surface temperature of each pixel is derived using the aforementioned emissivity.
3. Finally, a weighted least-squares fit between the MIVIS data and the simulated radiances at the sensor is done. The simulated radiances are estimated by means of the surface emission term ( $\epsilon B(T_s)$ ) and the atmospheric terms, contained in the LUTs. The best result indicates the  $\text{SO}_2$  abundance.

A Digital Elevation Model (DEM) registered to the image is requested by the *LUT-procedure*.

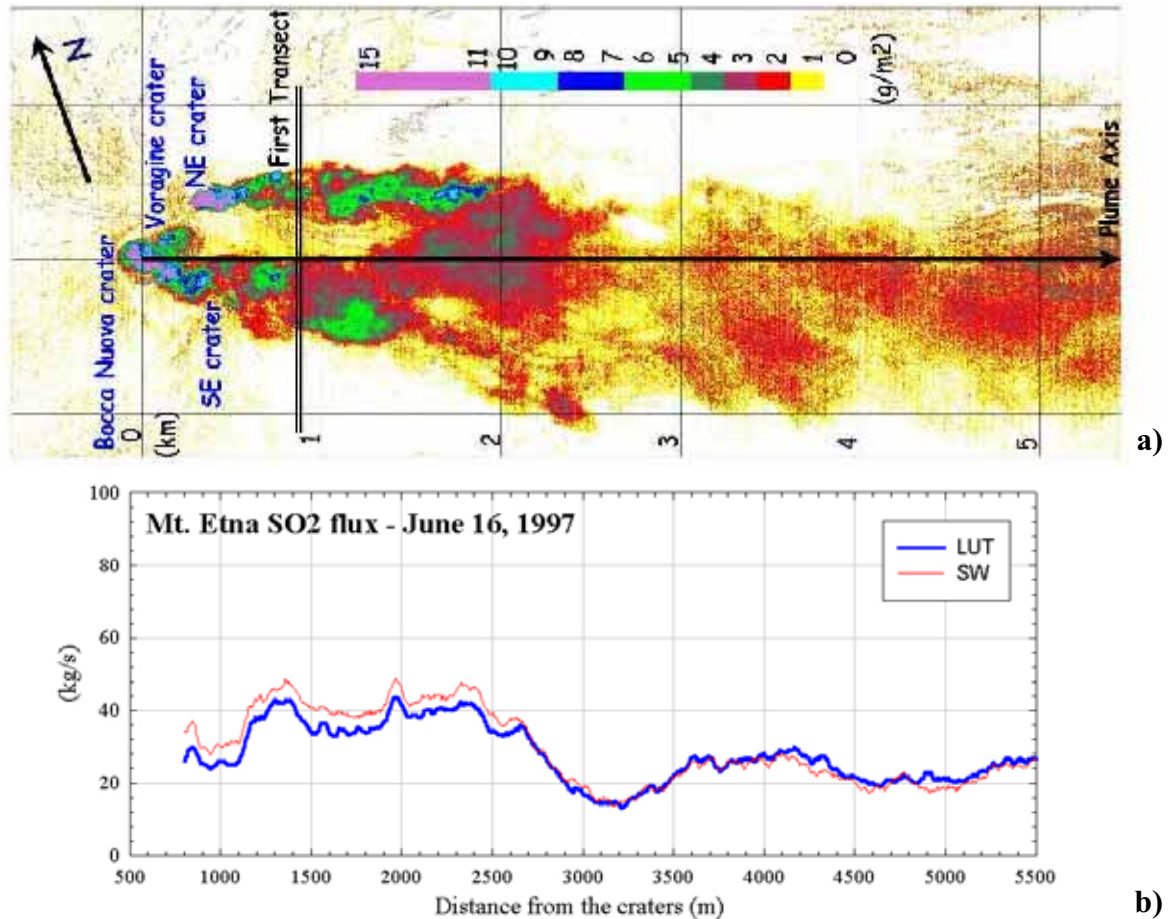


**Figure 2** (a) is the *split-window* SO<sub>2</sub> map derived from MIVIS-TIR channels 94 and 96 (see Tab. 1). (b) is the SO<sub>2</sub> flux emitted from Mt. Etna computed from (a) knowing the wind speed at the plume altitude (3300-3400 m asl); the two curves are for the two described LUT (thick) and SW (thin) procedures.

### 3.2 Split-Window

The split-window (SW) technique, developed at the end of 1970s, is based on the difference in atmospheric absorption at two different wavelengths. Its use is simple over the ocean where the temperature is quite uniform and the emissivity is close to unity and nearly constant over the whole 8-14 μm window. Over land, in particular for bare soil, the spectral emissivity variation becomes important, providing additional complications for the use of the SW. For these reasons this algorithm was initially used to estimate Sea Surface Temperature (SST) from AVHRR on board NOAA series satellites [Prabhakara et al., 1974; McMillin, 1975; Deschamps and Phulpin, 1980; McClain et al., 1985]. More recently the technique has been used to compute Land Surface Temperature (LST) [Price, 1984; Becker and Li, 1990; Prata, 1993], surface emissivity [Schmugge et al., 1991] and precipitable water [Andersen, 1996; Oettle et al., 1997].

In this paper an algorithm is presented, based on the split-window technique and derived by the LUTs quoted previously, to estimate the SO<sub>2</sub> abundance in the plume of Mt. Etna volcano. The SO<sub>2</sub> abundance is computed using equation (2) derived expanding all the radiances of equation (1):  $L(T_b)$ ,  $L_d(T_a)$ ,  $Lu(T_a)$ ,  $B(T_s)$  around a sort of “atmospheric temperature”  $T_a$ ;  $T_b$  is the brightness temperature. Only the first term (the linear term) of the expansion was considered. Using two different channels (let us say channel  $x$  and channel  $y$ ) is possible to eliminate the surface temperature  $T_s$  and obtain the following equation ( $x$  is the channel affected by SO<sub>2</sub> and  $y$  is the channel transparent to SO<sub>2</sub>)

$$S = k_0 + k_1 \cdot \ln \left( \frac{\epsilon_x \cdot T_{b,y} - T_a + k_2}{\epsilon_y \cdot T_{b,x} - T_a} \right) \quad (2)$$

$T_{b,x}$  and  $T_{b,y}$  are the brightness temperatures of

channels  $x$  and  $y$  respectively;  $\varepsilon_x$  is the emissivity of channel  $x$  and  $\varepsilon_y$  is the emissivity of channel  $y$ ;  $k_0$ ,  $k_1$ ,  $k_2$  and  $T_a$  are the parameters of the algorithm. Finally  $S$  is the  $\text{SO}_2$  columnar abundance in ( $\text{g m}^{-2}$ ).

(3)

$$k_0 = \frac{\delta_y - \delta_x}{\alpha}; \quad k_1 = \frac{1}{\alpha}; \quad k_2 = \varepsilon_y \cdot \tau_y \cdot (\Delta T_x - \Delta T_y)$$

$\Delta T$  ( $x$  or  $y$ ) is a little bit complex expression, with the dimension of a temperature, depending from different variables and with a small value (some K degrees). It is important to underline that  $\Delta T_x$  and  $\Delta T_y$  have similar values so their difference is very small.

To compute the sulfur dioxide of the Mt. Etna plume using equation (2) it is necessary to know the spectral emissivity of the surface; this may be done exactly as aforementioned at step 1). Then the four parameters of the algorithm are obtained fitting a set of radiances at the sensor computed with equation (1) using all the atmospheric terms contained in the LUTs and assuming a good thermal contrast between surface and plume (20-40 K). Only a plume with the base at constant altitude (Mt. Etna top altitude) and with a constant thickness (100 m) was considered for this algorithm. The use of this algorithm is simple, fast and do not need the registration of the DEM to the remotely sensed image.

At least  $k_0$  and  $k_2$  parameters obtained by the quoted fit (see relationships (3)), and of course  $T_a$  depend on the thermodynamic state of the atmosphere. This means that the parameters have to be computed every time; of course, this is requested by the *LUT-procedure* too.

Figure 2a is the  $\text{SO}_2$  map obtained applying *split-window* technique to the MIVIS TIR channels 94 and 96 (see Tab. 1); channels 94 is affected by  $\text{SO}_2$ , channel 96 is not. Figure 2b is the  $\text{SO}_2$  flux emitted from Mt. Etna computed from the  $\text{SO}_2$  columnar abundance map of Fig. 2a knowing the wind speed at the plume altitude (3300-3400 m asl).

#### 4. Seasonal trend of the *Split-Window* parameters

ASTER, like Thematic Mapper (TM) is able to see a point on the Earth surface each 16 days (i.e. its period is 16 days); this should be a suitable period to monitor  $\text{SO}_2$  emission of Mt. Etna. The aim of the research is to prepare an automatic procedure to be used together with a

spacecraft radiometer like ASTER.

To do this using SW algorithm means to know the four parameters  $k_0$ ,  $k_1$ ,  $k_2$  and  $T_a$ , but they depend on the state of the atmosphere. A first approximation is the determination of a set of climatologic parameters; a better approximation can be obtained modifying the climatologic parameters on the basis of few ground meteorological measurements.

To verify these assumptions four years (1997-2000) of radio sounding carried out at Trapani station at 12:00 GMT were collected. From these data twelve monthly typical atmospheric profiles were estimated and inputted in MODTRAN code; the obtained simulations were used to compute twelve sets of SW parameters. In figures 3a, b, c, d are reported the seasonal trend of  $k_0$ ,  $k_1$ ,  $k_2$ , and  $T_a$  respectively. As expected,  $T_a$  has a seasonal trend with a maximum during the summer season (July) and a minimum in winter (February). As seen in relationships (3)  $k_0$  and  $k_2$  have a seasonal dependence ( $k_0$  has the stronger one, it is indicated by the more precise trend). Finally, as relationships (3) indicate and as Fig. 3b shows,  $k_1$  may be considered about constant. In the four figures 3 the up and down triangles indicate the parameter values for 12<sup>th</sup> and 16<sup>th</sup> June 1997 respectively (MVRRS Sicily-97 campaign); the square indicates the results obtained for 29<sup>th</sup> July 2001.

The solid lines in figures 3a, 3c, 3d are the fits of the monthly typical parameters obtained using the first two harmonics of a Fourier expansion with one-year period. The solid line in figure 3b is the average of the  $k_1$  monthly values.

On 29 July 2001 at 10:00 GMT above Mt. Etna there was a typical cloud due to the presence of the volcano (orography, water vapor emission, solar heating of the surface etc.); it partially cover the plume exactly where the surface pixels have an altitude in the range used in the described procedures. The ASTER image taken on July 29 practically was the first available ASTER image of Mt. Etna with the wished characteristics. The SW procedure was stressed to detect, at least qualitatively, as much as possible the  $\text{SO}_2$  plume. Two different sets of parameters were computed: the first was related to the usual 2000-3000 m altitude range while the second was related to the range 0-3000 m. The values are reported in table 3. ASTER channels 11 and 14 (i.e. the second and fifth of the TIR range) were here used. Channel 11 is the ASTER channel mainly affected by  $\text{SO}_2$  (like channel  $x$  in equation 2); channel 14 is transparent to  $\text{SO}_2$  (like channel  $y$  in equation 2). The

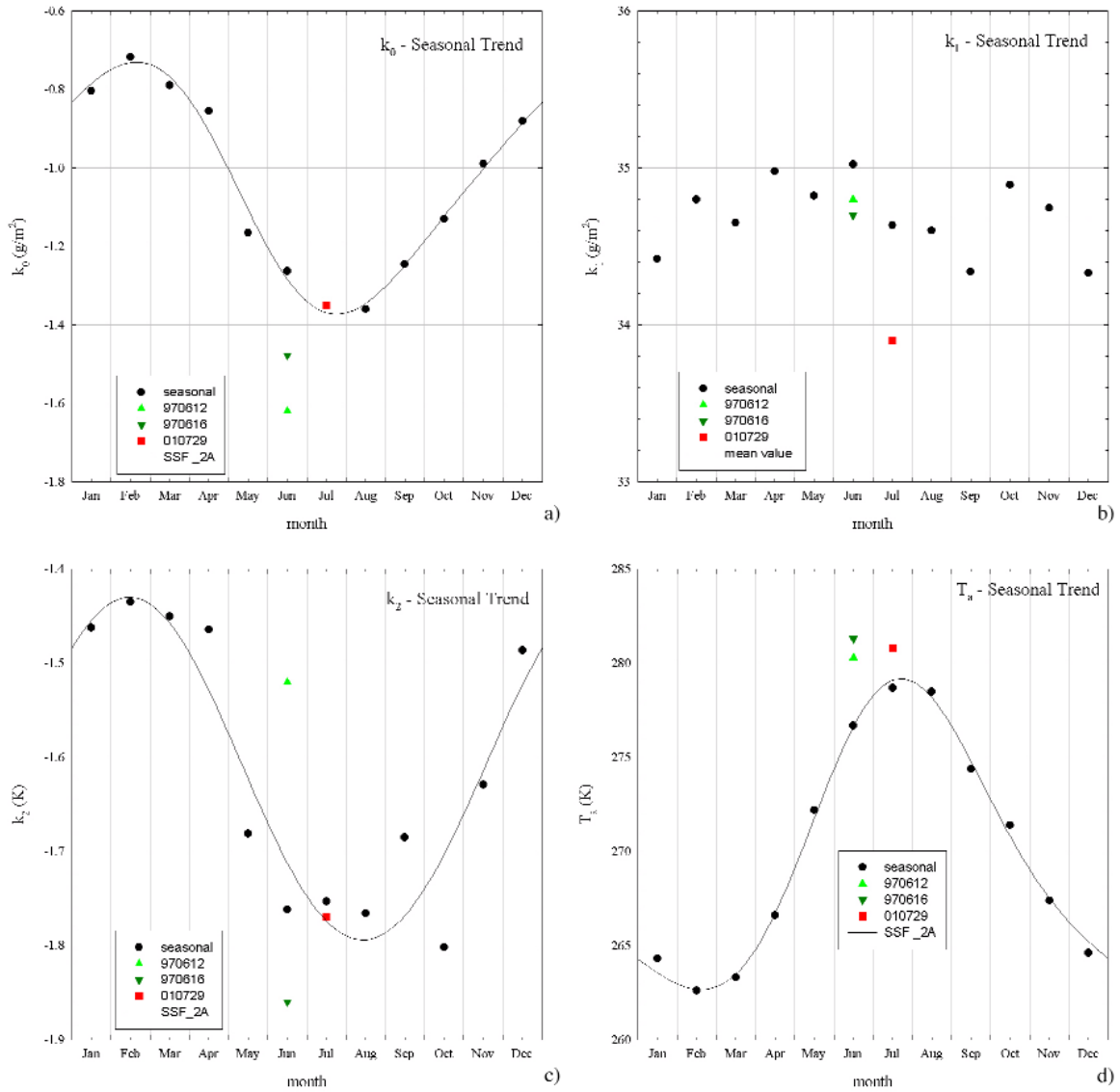


**Figure 3** Seasonal trend of *Split-Window* parameters computed using four years of Trapani station radio soundings: (a) is  $k_0$ ; (b) is  $k_1$ ; (c) is  $k_2$ ; (d) is  $T_a$ . The thin solid line (a, c, d) is a Fourier expansion considering two harmonics. The thin solid line in (b) is the mean value. In the four figures, the up and down triangles indicate the values obtained for June 12 and 16, 1997 respectively; the square is for July 29, 2001.

following emissivity values were used [Medici, 2000]:  $\varepsilon_{11}=0.95$ ;  $\varepsilon_{14}=0.97$ .

The parameters of the range 0-3000 m may only be used in qualitative approach; the main reasons are the following: 1) the used spectral emissivity (valid for the summit volcanic area) is not valid for vegetation and so on; 2) SW algorithm have to consider the additional strong effect of the first 2000 m of atmosphere; 3) the atmospheric characteristics of the first 2000 m closed to Mt. Etna may be quite different respect to the measured ones (close to Trapani); 4) the sea pixels have a surface temperature lower than land surface temperature; 5)

from the volcano summit to the seaside the plume geometry changes.

The  $\text{SO}_2$  plume obtained from a zoom of the two consecutive ASTER images (same swath, remotely sensed on 29 July 2001) using the SW-algorithm (0-3000 altitude range parameters) is shown in figure 4. The central line was assumed like plume axis. The two external lines indicate the plume width used to compute the  $\text{SO}_2$  flux (not reported here). Not far from the vents it can partially seen the effect of the presence of the aforementioned cloud (centered about at raw 650 and column 420); part of the clouds is outside the plume width line.

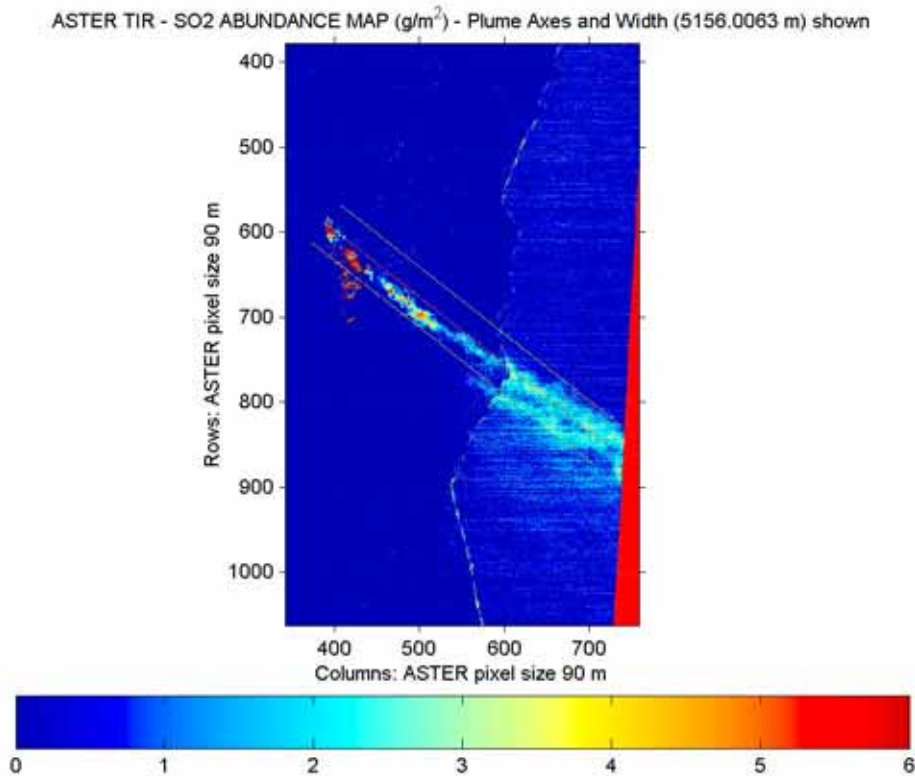


**Figure 4** Zoom of the SO<sub>2</sub> map obtained from two consecutive ASTER images taken on July 29, 2001 at about 10 GMT. The bar at the bottom suggests the SO<sub>2</sub> abundance in the plume (this is the first not yet validated result).

	$k_0$ (g m <sup>-2</sup> )	$k_1$ (g m <sup>-2</sup> )	$k_2$ (K)	$T_a$ (K)	SD (g m <sup>-2</sup> )
2000-3000 m altitude range	-1.35	33.9	-1.77	280.8	0.14
0-3000 m altitude range	-1.54	33.3	-1.74	280.6	0.30

**Table 3** ASTER-29 July 2001-SW parameters for two altitude ranges.

## 5. Conclusions

It has been presented two procedures to estimate the SO<sub>2</sub> abundance in the plume of Mt. Etna. These procedures [Teggi et al., 1999 and Pugnaghi et al., 2002] were initially prepared for MIVIS radiometer; here the *SW-procedure* has been used to analyse two consecutive ASTER images. The preliminary results reported here are part of the study carried out in the GNV 2000-2003 Framework Project # 13: “Development and application of remote sensing methods for the monitoring of active Italian volcanoes”.

The two procedures need the MODTRAN simulations performed with the measured atmospheric vertical profiles as input data. They can-

not automatically works for MIVIS radiometer but, with some assumptions, they can be used in real time for a space radiometer like ASTER. A first set of (let say) *climatologic* parameters has been shown for ASTER. They were obtained using four years of radio soundings (about 1500) carried out at Trapani at 12 GMT. Now eleven years of data (more than 14000 profiles) have been collected. Finally, part of the task aims to understand if few ground meteorological measurements, may be used to improve the result obtained from the *climatologic data set*.

## Acknowledgments

This work was in part funded by GNV 2000-

2003 Framework Project # 13 “Development and application of remote sensing methods for the monitoring of active Italian volcanoes”, task 5.1 Volcanic gases emissions and in part by the Italian Space Agency (ASI).

## References

- Abrams M, (2000) The Advanced Spaceborne Thermal Emission and Reflection Radiometer (ASTER): data products for the high spatial resolution imager on NASA's Terra platform. *Int J Remote Sensing* 21 (5): 847-859
- Allard P, Carbonelle J, Dajlevic D, Le Bronec J, Morel P, Robe MC, Maurenas JM, Faivre Pierret R, Martin D, Sabrouk JC, Zeltwoag P, (1991) Eruptive and diffuse emissions of CO<sub>2</sub> from Mount Etna. *Nature* 351: 387-391
- Andersen HS, (1996) Estimation of precipitable water from NOAA AVHRR data during the Hapex Sahel experiment. *Int J Remote Sensing* 17 (14): 2783-2801
- Becker F, Li ZL, (1990) Towards a local split window method over land surfaces. *Int J Remote Sensing* 11: 369-393
- Bhartia PK, Herman J, McPeters RD, (1993) Effect of Mount Pinatubo aerosols on total ozone measurements from backscatter ultraviolet (BUV) experiments. *J Geophys Res* 98: 18547-18554
- Bianchi R, Cavalli RM, Fiumi L, Marino CM, Pignatti S, (1996) Airborne remote sensing: Results of two years of imaging spectrometry for the study of the environmental problems. In: Spitterieds (eds) *Remote Sensing*. Balkema, Rotterdam The Netherlands pp 269-273
- Buongiorno MF, Bogliolo MP, Caltabiano T, Carrere V, Corradini S, Merucci L, Pugnaghi S, Salvi S, Sterni A, Teggi S, (1999) MVRRS Campaign: MIVIS mission on Sicilian volcanoes and ground measurements. *Ist Naz di Geofisica, Rome, Italy, Pub n 7*, pp 1-90
- Caltabiano T, Romano R, (1988) Messa a punto di metodologie di misura con apparecchiatura COSPEC del flusso di SO<sub>2</sub> da vulcani attivi italiani. *Boll GNV* 4: 133-145
- Caltabiano T, Romano R, Buretta G, (1994) SO<sub>2</sub> flux measurements at Mt Etna, *J Geophys Res* 99 (D6): 809-819
- Deschamps PY, Phulpin T, (1980) Atmospheric correction of infrared measurements of sea surface temperature using channels at 3.7, 11 and 12 mm. *Boundary Layer Meteorology* 18: 131-143
- Duuton EG, Christy JR, (1992) Solar Radiative forcing at selected locations and evidence for global lower tropospheric cooling following the eruptions of El Chichon and Pinatubo. *Geophys Res Lett* 19: 2313-2316
- Francis P, Burton M R, Oppenheimer C, (1998) Remote measurements of volcanic gas compositions by solar occultation spectroscopy. *Nature* 396 (6711): 567-570
- Ferrara R, Mazzolai B, Lanzillotta E, Nucaro E, Pirrone N, (2000) Volcanoes as emission source of atmospheric mercury in the Mediterranean basin. *Science of the Total Environment* 259 (1-3): 115-121
- Gillespie A, Rokugava S, Matsunaga T, Cothorn J S, Hook S, Kahle A, (1998) A temperature and emissivity separation algorithm for Advanced Spaceborn Thermal Emission and Reflection Radiometer (ASTER) images. *IEEE Trans Geosc Remote Sens* 36 (4): 1113-1126
- Medici P, (2000) Stima del Contenuto Colonnare di SO<sub>2</sub> del Plume dell'Etna da Immagini Telerilevate nell'Infrarosso Termico dal Radiometro ASTER a Bordo del Satellite Terra. Thesis, Modena and Reggio Emilia University, Modena (Italy) pp 1-195
- McClain EP, Pichhel WG, Walton CC, (1985) Comparative performance of AVHRR Based multichannel sea surface temperature. *J Geophys Res*, 90: 11587-11601
- McMillin LM, (1975) Estimation of sea surface temperature from two infrared window measurements with different absorption. *J Geophys Res* 80: 5113-5117
- Ottle C, Outalha S, Francois C, LeMaguer S, (1997) Estimation of total atmospheric water vapor from split window radiance measurements. *Remote Sensing Environ* 61 (3): 410-418
- Prabhakara C, Dalu G, Kunde VG, (1974) Estimation of sea surface temperature from remote sensing in the 11 to 13 mm window region. *J Geophys Res* 79: 5033-5044
- Prata AJ, (1993) Land surface temperature derived from the AVHRR and ATSR, 1, theory. *J Geophys Res* 89 (D9): 16689-16702
- Price JC, (1984) Land surface temperature measurements from the split window channels of the NOAA7 AVHRR. *J Geophys Res* 89: 7231-7237
- Pugnaghi S, Teggi S, Corradini S, Buongiorno MF, Merucci L, Bugliolo MP, (2002) Estimation of SO<sub>2</sub> abundance in the eruption plume of Mt. Etna using two MIVIS thermal infrared channels: A case study from the Sicily 1997 Campaign. In press on *Bulletin of Volcanology*
- Realmuto VJ, (1990) Separating the effects of temperature and emissivity: Emissivity spectrum normalization – 2<sup>nd</sup> Thermal Infrared Multispectral Scanner (TIMS) Workshop. In: EA Abbot (eds), *JPL Publ* 90 55: pp 310-316

- Realmuto VJ, Abrams MJ, Buongiorno MF, Pieri DC, (1994) The use of multispectral thermal infrared image data to estimate the sulfur dioxide flux from volcanoes: A case study from Mount Etna, Sicily, July 29, 1986. *J Geophys Res* 99: 481-488
- Realmuto VJ, Sutton AJ, Elias T, (1997) Multispectral thermal infrared mapping of sulfur dioxide plumes: A case study from the East Rift Zone of Kilauea Volcano, Hawaii. *J Geophys Res* 102: 15057-15072
- Rose WI, (1977) Scavenging of volcanic aerosol by ash: atmospheric and volcanological implications. *Geology* 5: 621-624
- Schmugge TJ, Becker F, Li ZL, (1991) Spectral emissivity variations observed in the airborne surface temperature measurements. *Remote Sensing Environ* 35: 95-104
- Stoiber RE, Williams SN, Huebert B, (1987) Annual contribution of Sulphur dioxide to the atmosphere by volcanoes. *J Volcanol Geotherm Res* 33: 1-8
- Teggi S, Bogliolo MP, Buongiorno MF, Pugnaghi S, Sterni A, (1999) Evaluation of SO<sub>2</sub> emission from Mt Etna using diurnal and nocturnal MIVIS TIR remote sensing images and Radiative transfer models. *J Geophys Res* 104 (B9): 20069-20079
- Yamaguchi Y, Kahle A, Tsu H, Kawakami T, Pniel M, (1998) Overview of Advanced Spaceborne Thermal Emission Reflection Radiometer (ASTER). *IEEE Trans on Geoscience and Remote Sensing* 36: 1062-1071

## Aerosol Optical Characteristics of Volcanic Plume Retrieval by Means of Remote Sensing Techniques: the Case of Mt. Etna Studied Using the MIVIS Airborne Multispectral Image Spectrometer

Spinetti C. and Buongiorno M.F.

Istituto Nazionale di Geofisica e Vulcanologia, Roma

### Abstract

The European Community funded the 'Mitigation of Volcanic Risk by Remote Sensing Techniques' (MVRSS) Project to mitigate volcanic risk in populated areas, particularly to study and monitor the tropospheric volcanic plumes by means of remote sensing techniques. In the frame of this project a field measurement campaign was organized on Mt. Etna and Eolian Island in June 1997. During this campaign digital images were collected with the Airborne Multispectral Image Spectrometer (MIVIS) together with ground-based measurements. The MIVIS instrument is an image spectrometer that acquires data in 102 spectral channels from visible to thermal infrared. In July 2001 a new MIVIS airborne campaign was organized during the Etna eruption to compare the optical characteristics of the volcanic plume during both a quiescent and an active status of the volcano.

In the present paper MIVIS images were used to retrieve the aerosol optical characteristics of the Etna volcanic plume in the visible channels. The 6S (Second Simulation of the Satellite Signal in the Solar Spectrum) radiative transfer model has been used to model the atmosphere parameters for the selected MIVIS images. An inversion algorithm has been developed, it is based on radiative transfer equations and applied to the upwelling radiance values calculated from the raw image data (DN) measured by the sensor, to retrieve the aerosol optical thickness ( $\tau^a$ ) of the volcanic plume. The inversion procedure takes into account the spectral albedo of the surfaces under the plume and the topographic effects on the reflected radiance, due to the surface orientation and elevation. The ground spectral reflectances were estimated both by field spectra-radiometers measurements, executed during the 1997 campaign, and by laboratory measurements performed on rock samples collected in the field. The result of the inversion procedure is the  $\tau^a$  spatial distribution

of Etna plume. In the wavelength range 454 – 474 nm an average value of  $\tau^a=0.1$  and  $\tau^a=1$  has been retrieved for effusive and for explosive

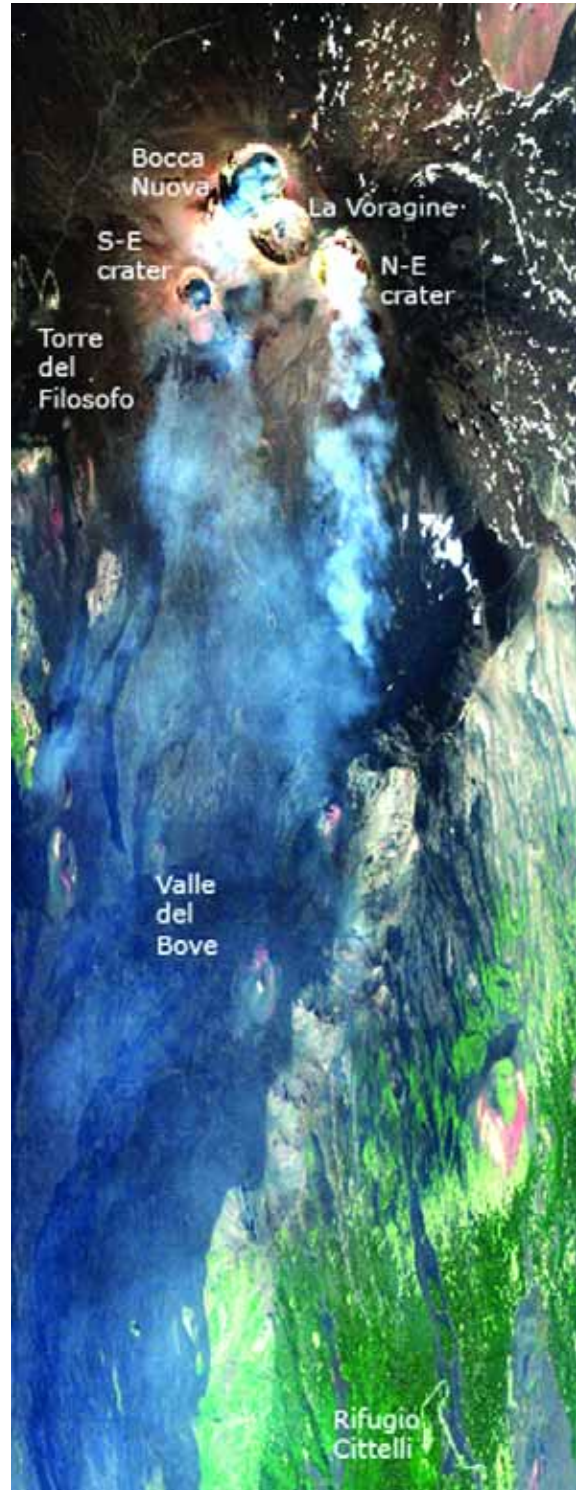


**Figure 1** MIVIS image Etna June 16<sup>th</sup> 1997 calibrated in Radiance RGB composition. Flight altitude 6000 m. Pixel resolution ranges to 4x4 m<sup>2</sup> at summit craters to 11x11 m<sup>2</sup> at the sea level.

plume, respectively. Finally, a multispectral analysis performed on 'Sicily 1997' data, permits to retrieve the Ångström parameters  $\alpha$  and  $\beta$ . The particle size was dominated by particles with an effective radius  $<1$  micron for the particular effusive plume close to the N-E Crater.

## 1. Introduction

Tropospheric volcanic plumes represent a visible indicator of volcanic activity. Exsolving from magma, plumes consist in a turbulent mixture of gases, solid particles and liquid droplets, emitted at high temperature continuously from summit craters, fumarolic fields or during eruptive episodes. Water vapor represents 70% – 90% of volcanic gases and the main gaseous components are  $\text{CO}_2$ ,  $\text{SO}_2$ ,  $\text{HCl}$ ,  $\text{H}_2$ ,  $\text{H}_2\text{S}$ ,  $\text{HF}$ ,  $\text{CO}$ ,  $\text{N}_2$ ,  $\text{CH}_4$  [Bardintzeff, 1998]. Volcanic ash, aqueous and acid droplets and solid sulphur-derived particles represent other plume components. Volcanic particles and liquids droplets suspended in the atmosphere are defined as volcanic aerosols; typical size is in the range  $10^{-2} \mu\text{m} - 10 \mu\text{m}$  [Sparks et al., 1997].

Volcanic emissions are important in the field of volcanism, transporting information from magma to the atmosphere [Amman et al., 1992] and in the field of environment. Volcanic gases and aerosols have important climatic and environmental effects [Fiocco et al., 1994]. Different volcanic activities, such as volcanic eruption, volcanic clouds and plumes, inject into the atmosphere volcanic aerosol with different altitudes, latitudes and residence times.

Aerosols are radiatively active, since they are able to modify the atmospheric radiative field, depending on their altitude, residence time and on their concentration. They scatter the incoming short-wave solar radiation and absorb the outgoing long-wave radiation. Moreover, they play an important role on acid rain formation and they are destructive to the environment contaminating local water supplies [Jaeschke et al., 1982].

Previous studies of volcanic aerosol tend to focus on large-scale emissions into the stratosphere [Fiocco et al., 1994; Hansen et al., 1992], while the radiative effects of the tropospheric volcanic aerosols are little modeled and poorly quantified.

The remote sensing data analysis permits to obtain continuous information to characterize variable atmospheric components, such as volcanic aerosols, while field measurements allows to obtain often only few observations.



**Figure 2** MIVIS image Etna July 29<sup>th</sup> 2001 calibrated in Radiance RGB composition.

Moreover, some volcanic sites are inaccessible and hazardous and the remote sensing represents the only possible investigation technique that permits a fast, large-scale and above all safe measurements of the volcanic emissions.

## **2. Data Set**

The data were acquired in the framework of the 'Mitigation of Volcanic Risk by Remote Sensing Techniques' (MVRSS) project, funded by the European Community, on the 'Sicily 1997' MVRSS campaign and on the '2001 MIVIS mission'.

In order to obtain the aerosol optical characteristics of Mt. Etna volcanic plume, high-resolution hyperspectral remote sensed images of two different status of the volcano were used. The images of the effusive plume were acquired during the 'Sicily 1997' field measurements campaign [Buongiorno et al., 1999] while the images of the explosive plume were acquired during the 2001 Etna eruption by means of the Airborne Multispectral Image Spectrometer (MIVIS).

The MIVIS instrument, owned by CNR - LARA Project and operated by the Compagnia Generale Riprese Aeree (CGR), represents a second generation imaging spectrometer developed for environmental remote sensing studies [Bianchi et al., 1994]. It is a Daedalus AA5000 electro-optical scanner with 102 spectral channels simultaneously sampled and recorded. The 4 spectrometers collect the radiation reflected by the surface in the spectral range (0.4÷2.5) microns and (8÷12) microns (see Table 1).

### **2.1. The 'Sicily 1997' MVRSS Campaign**

In the period 11 - 17 June 1997, the airborne campaign took place over Etna, Vulcano and Stromboli. The period was chosen to have suitable weather conditions since the solar irradiance is near to its yearly maximum, the expected relative humidity is low and the expected wind direction is N-W prevalently. These factors allow the acquisition of good quality images since the area under the plume is well illuminated and, especially in the early morning, the formation of orographic clouds is limited.

The time weather conditions were as expected: the sky was cloudless during the entire week, except for the 17<sup>th</sup>. A temperature mean value of  $(12.5 \pm 1.5)$  °C, a low relative humidity of  $35\% \pm 5\%$  (except for the 17 June when relative humidity was 42%), a pressure of  $(723 \pm 3)$  hPa, a wind speed between 11 to 20 m/s and wind direction of about 300 degree North, has been measured at Torre del Filosofo meteorological station (2920m a.s.l. height).

During the campaign, the 3 observed volcanoes presented different activity levels. Mt. Etna was in a quiescent period after 1996 erup-

tion. It showed a major degassing activity in the N-E crater, a minor one in Bocca Nuova crater and same episodes of lava fountains in the S-E and La Voragine craters. Stromboli (924m a.s.l. height) showed small eruptions of ashes and lava with a frequency of 2-3 episodes per hour. Volcano (390m a.s.l. height) presented fumarole fields and gas emissions located in the Fossa crater.

Images of Etna plume were taken by 3 flight lines having a radial arrangement, one along the plume axis oriented on E-S-E direction and two along each side. Most of the ground-based measurement sites were located on the south-eastern flank of the volcano, covered also by an additional flight line. The platform altitude was about 6500m a.s.l. and the corresponding ground resolution ranged from 4 to 13 m, depending on orography and aircraft altitude.

Different ground-based measurements, derived from atmospheric, radiometric and spectral data, were taken simultaneously to the flights, and are reported in Table 2.

### **2.2. The '2001 MIVIS Mission'**

During the 2001 Etna eruption the INGV (Geodesy and Remote Sensing Laboratory of Rome) organized an airborne campaign with the MIVIS instrument in order to acquire high-resolution images on the explosive volcanic plume and on the active lava flow that was heading towards Nicolosi town.

The campaign was executed on July 29<sup>th</sup> 2001 after a quick notice from NASA that had scheduled the acquisition of the ASTER sensor on TERRA satellite in that date. The MIVIS acquired 8 flight lines in a radial arrangement crossing over the summit area. The flight lines covered the entire Etna structure with an approximately area of 40 by 40 km. The flight altitude was 6400m a.s.l. and the corresponding ground resolution ranged from 6 to 12 m depending on the surface elevation.

In that period Mt. Etna presented a complex eruption involving a summit and a flank activity. The eruption started on July 17<sup>th</sup> and continued until August 9<sup>th</sup> 2001, for 24 days of total explosive activity. The most spectacular products are the large pyroclastic cones that grew at about 2500 and 2100m elevation. Particularly, the day of Mivis flight, the various fissure systems located on the S and NE flanks of the volcano at 2900, 2700 and 2100m elevation, presented activity with a lava eruption rates moderately high, about  $16 \text{ m}^3$  per second [Behncke, 2001]. Some of the flank activities

Optical port	Spectral Range	Number of channels	Spectral resolution
1 (VIS)	431-833 nm	20	20 nm
2 (NIR)	1.150-1.550 $\mu\text{m}$	8	50 nm
3 (SWIR)	1.985-2.479 $\mu\text{m}$	64	9 nm
4 (TIR)	8.210-12.700 $\mu\text{m}$	10	340-540 nm

**Table 1** MIVIS spectral bands characteristics [Bianchi et al., 1994].

Ground-based measurements	Type of data	Use in the MIVIS data analysis
Atmospheric vertical profiles with onboard balloon Radiosonde.	Pressure, Temperature, Relative humidity, Wind direction and speed.	Modelling of the atmospheric parameters.
Sun-photometric measurements with 2 sun-photometer located in different places.	Total atmospheric optical thickness, Aerosol optical thickness and Ångstrom turbidity parameters.	Modelling of the atmospheric optical characteristics.
Radiometric measurements with spectroradiometer.	Atmospheric radiance	Modelling of the atmospheric radiative contributes.
Meteorological station at Torre del Filosofo.	Pressure, Temperature, Relative humidity, Solar radiation flux and Wind direction and speed.	Modelling of the atmospheric parameters at the ground level.
VIS-IR spectra and Rock sampling for laboratory analyses.	Spectra of volcanic rock, vegetation and terrain.	Ground truth for surface reflectance

**Table 2** MVRSS ‘Sicily 1997’ campaign ground based measurements [Buongiorno et al., 1999].

were unusually violent, with strong phreatomagmatic and magmatic explosions and abundant emission of pyroclastics. A dense ash plume drifted hundreds of kilometers away, mostly to the SE, causing heavy ash falls in Catania city and surroundings.

### 3. Image Processing

Before starting the data analysis, 3 steps had to be followed [Spinetti et al., 2001]. First step was the selection of a single digital image for each data set with the following criteria:

- the plume should be well contained in the image;
- the signal-to-noise ratio should be large;
- cloudless conditions should be present.

The image satisfying these criteria was acquired on the first flight line during the '2001 Mivis mission', with an aircraft trajectory of about 176 North degree. In Figure 1 the selected image is showed. For the 'Sicily 1997' MVRSS campaign, the image satisfying the criteria and have simultaneous ground-based measurements (atmospheric photometric measurements and vertical profile) was acquired on June 16<sup>th</sup>, with an aircraft trajectory about 87 North degree. In Figure 2 the selected image is showed.

Second step in image processing is the radiometric calibration of the raw images data; it means the conversion of the digital numbers (DN) into radiance values, obtained by multiplying pixel by pixel each DN by the calibration factor [Bianchi et al., 1994].

Third step is the definition of the optical path geometry from the ground to the sensor. To this purpose the images were co-registered to a Digital Elevation Model (DEM) of Mt. Etna, in order to define the corresponding elevation and inclination of the ground represented on each image pixel.

### 4. Inversion Technique

The method used to retrieve the aerosol optical thickness is based on the hypothesis of cloudless sky and plane parallel atmosphere. With these assumptions, radiance measured by a remote sensor in the atmosphere is given by the following radiative transfer equation for monochromatic radiation and no surface emission [Spinetti et al., 2002]:

$$\rho^* = \rho_a + \rho_a^p + \rho' \cdot \frac{T_u^p \cdot T_d^p}{1 - \langle \rho \rangle \cdot S} + \langle \rho' \rangle \cdot \frac{T_u^p \cdot T_d^p}{1 - \langle \rho \rangle \cdot S} \quad (1)$$

where:

$$\rho^* = \frac{\pi \cdot L}{F_0 \cdot \mu_s}$$

is the apparent reflectance at the sensor;  $L$  is the radiance at the sensor,  $F_0$  is the extraterrestrial solar flux and  $\mu_s = \cos \theta_s$  is the cosine of the solar zenith angle;

$$\rho_a = \rho_a(\theta_s, \theta_v, \phi_s, \phi_v)$$

is the atmospheric path reflectance;  $\theta_s$  is the solar zenith angle and  $\theta_v$  is the viewing angle;  $\phi_s$ ,  $\phi_v$  are the solar and view azimuth angle, respectively;

$$\rho_a^p = \rho_a^p(\theta_s, \theta_v, \phi_s, \phi_v)$$

is the radiation scattered into the optical path by the plume;

$$\rho' = \frac{\rho}{1 - \langle \rho \rangle \cdot S} T_d(\vartheta_s) \cdot T_u(\vartheta_v)$$

$\rho$  is the surface reflectance;  $\langle \rho \rangle$  is the environmental reflectance;  $S$  the atmospheric spherical albedo;  $T_d(\theta S)$  is the downward total transmittance in the path from top of the atmosphere (TOA) to the surface;  $T_u(\theta V)$  is the upward total transmittance in the path from the ground to the sensor;

$$\langle \rho' \rangle = \frac{\langle \rho \rangle}{1 - \langle \rho \rangle \cdot S} T_d(\vartheta_s) \cdot T_u(\vartheta_v)$$

$T_d(\theta S)$  and  $T_u(\theta V)$  are the downward and the upward plume transmittance, respectively, function of volcanic aerosol optical thickness.

In the single-scattering approximation  $\rho_a^p$  the plume path reflectance is given by:

$$\rho_a^p(\theta_s, \theta_v, \phi_s, \phi_v) = \rho_m^p + \frac{\omega_0 \cdot P(\psi_s)}{4(\mu_s + \mu_v)} \left\{ 1 - \exp \left[ - \frac{\tau_a + \tau_a}{\mu_s + \mu_v} \right] \right\} \quad (2)$$

$\rho_m^p = \rho_m^p(\theta_s, \theta_v, \phi_s, \phi_v)$  is the molecular scattering path reflectance,  $\omega_0$  single-scattering albedo,  $P(\psi_s)$  phase function and  $\tau_a$  the volcanic aerosol optical thickness;  $\mu_v$  and  $\mu_s$  are cosines of the view and illumination directions, respectively.

In order to invert the equation (1) and extract the aerosol optical thickness  $\tau_a$ , it is necessary to estimate the atmospheric terms for each pixel of the MIVIS image. To this purpose, the 6S (Second Simulation of the Satellite Signal in the Solar Spectrum) radiative transfer code [Vermonte et al., 1997] has been used. The

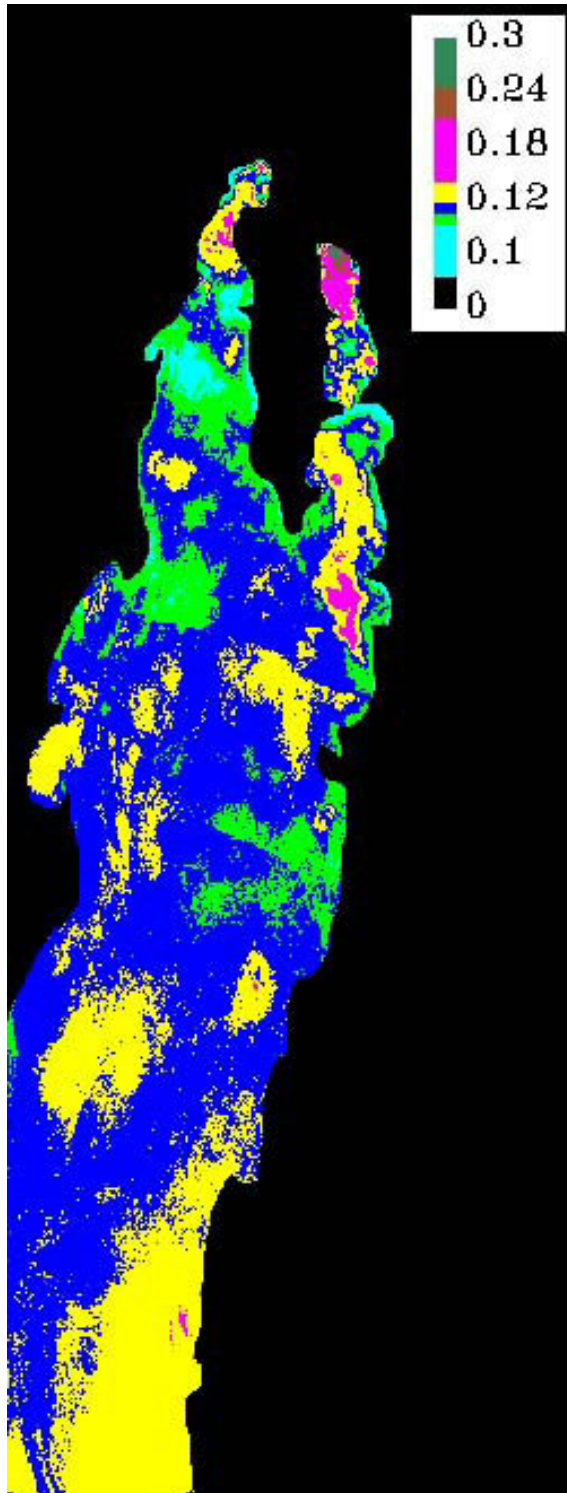


**Figure 3** Resulting map of effusive volcanic plume aerosol optical thickness ( $\tau^a$ ) in false colours for June 16<sup>th</sup> 1997. Average value of spatial distribution  $\tau^a=0.1$ .

Digital Elevation Model (DEM) was used to take into account the elevation of each pixel for a correct estimation of atmospheric transmittance in the inversion procedure. Moreover, the inversion procedure needed the knowledge of

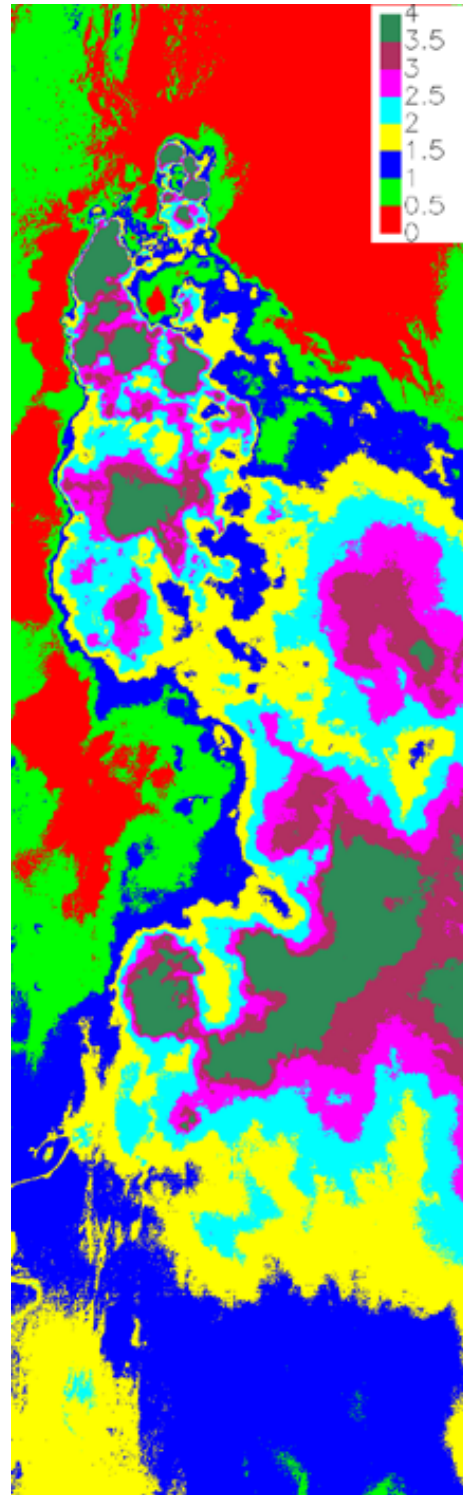


**Figure 4** Resulting map of explosive volcanic plume aerosol optical thickness ( $\tau^a$ ) in false colours for July 29<sup>th</sup> 2001. Average value of spatial distribution  $\tau^a=1$ .

the surface albedo and the ground inclination of each pixel respect to the sun and sensor relative positions. The ground albedo measurements show a low reflectance of basaltic lava  $<0.1$ . The ground inclination was obtained from the

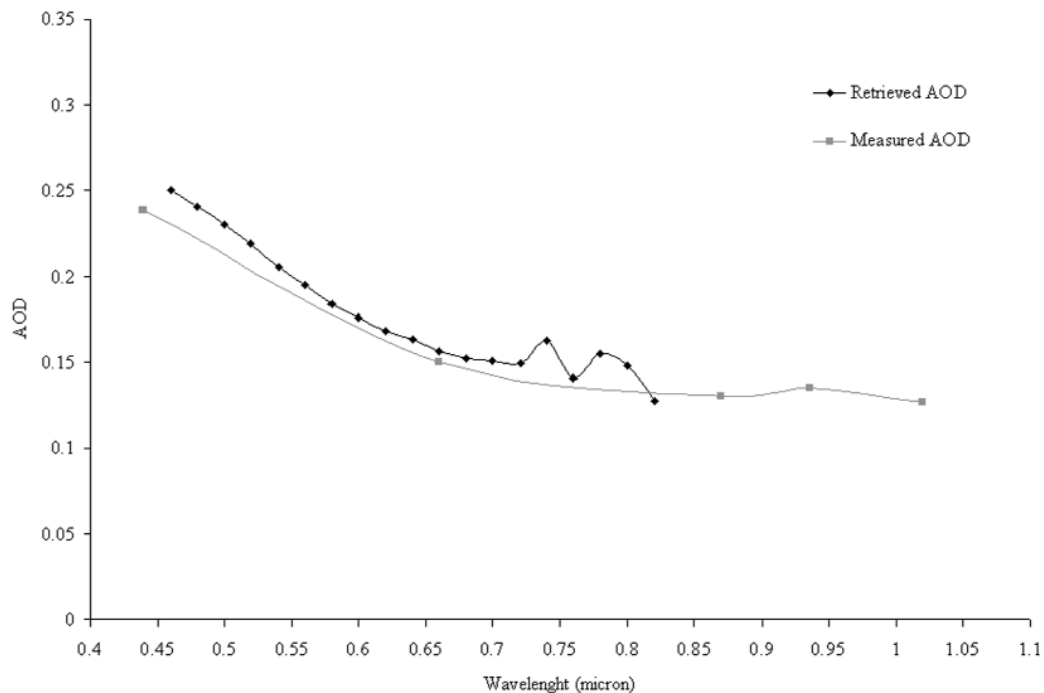


**Figure 5** Blue solid line indicate the  $\tau^a$  measured by sun-photometer (October 26<sup>th</sup> 1997) and red solid line indicate  $\tau^a$  obtained from the inversion procedure of MIVIS data (June 16<sup>th</sup> 1997).

shadow digital model (Shaded Relief) using the DEM and the geometrical factors of the source, such as solar zenith and azimuth angles [Horn et al., 1989].

The necessary condition is represented by the low reflectance of the surface [Kaufman et al., 1997]. This condition is respected for the selected image acquired on June 16<sup>th</sup> 1997, in that date the surface under the plume was cool basaltic lava rock. To invert the July 29<sup>th</sup> 2001 Mivis image, the equation (1) has been approximated considering only the atmospheric and plume path reflectance terms. The approximation is justified by the absence of transparency of the plume that prevented the remote sensing signal from crossing the explosive plume and causing its reflection.

Before inverting equation (1), a digital mask has been applied to the image in order to isolate the pixels belonging to the plume.

## 5. Results and Future Developments

The inversion procedure has been applied to the spectral MIVIS images in the range 454 – 832 nm. The maps in Figure 3 and in Figure 4 show the results of the inversion, indicating the spatial distribution of volcanic aerosol optical thickness in the wavelength range 454 – 474 nm. For the effusive plume (map in Figure 3)

the  $\tau^a$  values range from a minimum of 0.1 in the far part of the plume, to a maximum of 0.3, close to the summit craters. Conversely, the map in Figure 4 shows the spatial distribution of volcanic aerosol optical thickness for the upper part of the thick explosive plume, with the  $\tau^a$  values that range from a minimum of 0.5 to a maximum of 4. As deduced from the map the higher values of  $\tau^a$  are in various part of the plume corresponding to the different flank eruptions.

Spectral trend of  $\tau^a$  has been obtained for each pixel inverting the June 16<sup>th</sup> 1997 spectral images. It is possible to compare the  $\tau^a$  obtained with photometric measurements [Oppenheimer, 1998] choosing pixels of the spectral images corresponding to a zone containing the plume situated in North East Crater. In figure 5 the trend is reported and shows a rather good agreement with sunphotometric measurements as long as the Ångström equation. In the near infrared the signal is probably influenced by gaseous presence and the Ångström equation is not respected. Considering only the plot corresponding to the visible range, a value of  $\alpha=1.186$  for Ångström exponent and a value of  $\beta=0.09$  for turbidity coefficient has been retrieved, according with the measured range values of Ångström parameters  $\alpha=(0.13\div 2.42)$  and  $\beta=(0.001\div 0.14)$ . To the a value is possible to deduce that the particle size distribution was dominated by particles with an effective radius

<1 micron for the particular effusive plume close to the N-E Crater. However, this is a preliminary result, because the direct optical measurements across the plume are not simultaneous. The inversion method is not completely validated, because, as most of the inverse problems, requires input information on atmospheric parameters simultaneously. In a volcanic zone these parameters are not easy available due to the hazard and difficult to acquired ground based measurements under the plumes. However, the comparison with the sunphotometric measurements taken in Torre del Filosofo in October 1997 [Oppenheimer, 1998] is significant, assuming similar aerosol burden in this two periods. This is a reasonable assumption because Mt. Etna had similar quiescent conditions in June and in October 1997.

The MVRRS project foresees to install a ground-based photometer instrument that will takes atmospheric and plume data continuously. These data will be the ground truth for developing and validating the remote sensing techniques.

The future work will regard the development of a suitable methodology, combining remote sensing data, ground based data and atmospheric modeling to systematically study the volcanic plumes characteristics.

### Acknowledgments

The work was developed during a PhD on Remote Sensing, University of Rome "La Sapienza". The work was carried out at INGV, partially funded by GNV and ASI. The European Community (MVRSS project, Contract n. ENV4-CT96-0288) funded the MIVIS 1997 campaign.

### References

- Amman, M., Scherrer, L., Mueller, W., Burtscher, H. and Siegmann, H.C., (1992). Continuous monitoring of ultrafine aerosol emissions at Mt. Etna. *Geophysical Research Letters*, Vol. 19, No. 13, pp. 1387-1390, July 6, 1992.
- Bardintzeff, J.M., (1998). *Volcanologie*. 2<sup>e</sup> édition, Dunod Editeur.
- Behncke, B., (2001). *Italy's Volcanoes: the Cradle of Volcanology*. Università di Catania. Web site <http://boris.vulcanoetna.com/>
- Bianchi, R., Marino, C.M. and Pignatti, S., (1994). Airborne hyperspectral remote sensing in Italy. *Proceedings of the European Symposium on Satellite Remote Sensing* (Rome, Italy, September 26-30, 1994), EUROPTO Series, SPIE, Vol. 2318, pp. 29-37.
- Buongiorno, M.F., Bogliolo, M.P., Caltabiano, T., Carrere, V., Corradini, S., Merucci, L., Pugnaghi, S., Salvi, S., Sterni, A. and Teggi, S., (1999). MVRRS Campaign: MIVIS mission on Sicilian volcanoes and ground measurements. *Quaderni di Geofisica n.7*. Pub. Ist. Naz. Di Geofisica, Rome, Italy.
- Fiocco, G., Fua', D. and Visconti, G., (1994). The Mount Pinatubo Eruption Effects on the Atmosphere and Climate. *NATO ASI Series, Series 1: Global Environmental Change*, Vol. 42.
- Hansen, J., Lacis, A., Ruedy, R., Sato, M., (1992). Potential climate impact of Mount Pinatubo eruption. *Geophysical Research Letters*, Vol. 19, pp. 215-218, 1992.
- Horn, B.K.P. and Brooks, M.J., (1989). *Shape for shading*. The MIT Press, Cambridge.
- Jaeschke, W., Berresheim, H., Georgh, H., (1982). Sulfur emission from Mount Etna. *Journal of Geophysical Research*, Vol. 87, No. C9, pp. 7253-7261, August 20, 1982.
- Kaufman, Y.J., Tanre', D., Remer, L.A., Vermote, E.F., Chu, A., Holben, B.N., (1997). Operational remote sensing of tropospheric aerosol over land from EOS moderate resolution imaging spectroradiometer. *Journal of Geophysical Research*, Vol. 102, No. D14, pp. 17,051-17,067, July 27, 1997.
- Oppenheimer, C., (1998). RDT Programme Environment And Climate, MVRSS Mitigation of Volcanic Risk by Remote Sensing, Second Term Scientific Progress Report of Contract n. ENV4-CT96-0288.
- Sparks, R.S.J., Bursik, M.I., Carey, S.N., Gilbert, J.S., Glaze, L.S., Sigurdsson, H. and Woods A.W., (1997). *Volcanic plumes*. Wiley editor.
- Spinetti, C., Buongiorno, M.F., Lombardo, V. and Merucci, L., (2002). Retrieval of Aerosol Optical Thickness in Volcanic Plumes by means of the Airborne Multispectral Image Spectrometer (MIVIS): a case study from Mt. Etna, Sicily, June 1997. *Special issue of Annali di Geofisica* (in press).
- Vermote, E., Tanre', D., Deuze', J.L., Herman, M. and Morcrette, J.J., (1997). *Second Simulation of the Satellite Signal in the Solar Spectrum 6S. User Guide Version 2*, July 1997.

## A Tool for Spatial Data Exploitation Vulcano Island

Baldi P.<sup>1</sup>, Fabris M.<sup>2</sup>, Marsella M.<sup>3</sup>,  
Monticelli R.<sup>3</sup>, Signoreto V.<sup>3</sup>

<sup>1</sup>Physic Department, Università di Bologna

<sup>2</sup>D.A.U.R., Università di Padova

<sup>3</sup>D.I.T.S., Università di Roma "La Sapienza"

### Abstract

In the framework of the research activities devoted to monitoring deformation phenomena, photogrammetric surveys at 1:5.000-1:10000 scale were carried out on Vulcano Island in 1993, 1996 and 2001. Large scale digital map products (Digital Elevation Models and orthophotos) were extracted to be used for multi-temporal analysis of morphological changes occurred in the past. In order to display, query, summarize and organize data the collected spatial and image data, a software dedicated to georeferenced data management (ELA) was developed. The ELA Software and a collection of raster and vector data related to Vulcano Island (included in a CD-ROM available to the research community) are described in this work.

Copies of the CD-ROM can be obtained from the authors by sending an e-mail to [maria.marsella@uniroma1.it](mailto:maria.marsella@uniroma1.it).

### 1. Introduction

In the framework of the research activities devoted to the use of multi-temporal reconstruction of the ground surface (Digital Elevation Model) for monitoring crustal deformation phenomena, high resolution images of the Vulcano Island were collected by means of aero-photogrammetric surveys carried out in 1993, 1996 and 2001 (Achilli et al., 1997, 1998). Low altitude photogrammetric data of the "La Fossa" cone and its surrounding area (at a scale of 1:5.000) were acquired during the three surveys; 1996 images at a scale of 1:10000, covering the entire island, are also available.

All the images, obtained by film camera, were digitized at a resolution of 1000 dpi, corresponding to a ground pixel resolution of about 12.5 centimetres for images at a scale of

1:5000. After performing the standard images orientation procedure, the automatic correlation module of the digital Photogrammetric Workstation DPW 770 Helawa was used; a manual editing procedure was adopted in highly vegetated areas, where the matching procedure identifies 3D points, like those on the top of canopy, which should not be included in the DEM. A 10-meter grid DEM and an orthophoto of the entire island were generated. For the cone area, where images at a larger scale (1:5000) were acquired, a 5-meter grid DEM was produced. A higher spatial resolution DEM (1X1m grid) was extracted for the north-eastern flank of the cone (*Forgia Vecchia*) and its surrounding area (Baldi et al., 1998, 2000, 2002).

Vulcano Mount is located in the Thyrrenian Sea (Italy), approximately 15 miles off the north-eastern coast of Sicily. Under a morphological point of view, Vulcano can be divided into four main structural units: Southvulcano, *La Fossa* of Vulcano, *Lentia* Mountains and *Vulcanello* Peninsula.

- **Southvulcano**, the oldest part of the island, was a stratovolcano whose caldera's central part collapsed forming the *Caldera del Piano*. Actually the morphology is represented by a circular cone truncated, at 300-400m above sea level, by the plain of Vulcano Piano.
- **La Fossa of Vulcano** is an active crater, which arises from sea level up to 390m forming a steep cone. La Fossa of Vulcano is nested into a circular depression (*Caldera della La Fossa*), which represents the latest stage of the *Caldera del Piano* evolution: a multiple caldera collapse continuously migrating from SE to NW.
- **Lentia Mountains** represents the rocky hills group forming the western edge of *Caldera La Fossa*.
- **Vulcanello Peninsula** appeared as an island in 183 B.C. and got connected with Vulcano as a consequence of sand accumulation phenomena around 1550 A.D [Keller, 1980].

Vulcano activity (last eruptive process took place in 1888-1890) is characterized by eruptions separated by long low activity intervals. The systematic monitoring of the volcano activity allowed the observation of a persisting fumarolic activity with variations in the outgoing gases chemical composition, of a low seismic activity and of the creation of new fractures [Barberi et al., 1991].

## **2. Why a CD-ROM of Vulcano Island?**

Vulcano Island is a populated volcanic island, which was affected by its last eruptive process only in 1888-1890. Furthermore, in 1988 the northeastern side of its cone was affected by a landslide, which produced a small tsunami in the harbour area [Tinti et al., 1999]. The event was caused by the dynamically unstable conditions of the volcano [Rasà and Villari, 1991]. The availability of high resolution digital terrain models in areas affected by relevant crustal deformations phenomena, large instability phenomena or lava flows, allows the performance of a detailed morphologic analysis of the terrain physical surface, by the evaluation of elements such as mass balance, deformation vectors, morphometric parameters, and the extraction of morphological features. The monitoring of surface deformation phenomena through the analysis of temporal series of high resolution DEMs turns out to be an useful supporting activity to georeferenced databases and as a basis for hazard and risk studies.

## **3. The contents of the CD-ROM**

This CD-ROM consists of the ELA Software and of a collection of raster and vector data related to Vulcano Island. The installation file (setup.exe) is located in the directory named "Software" of the CD-ROM. ELA is a geographic data management software useful to display, query, summarize and organize georeferenced spatial and image data. Spatial and image data of Vulcano Island represent the core of the CD-ROM. Spatial data are geographic data in which the geometric location of geographic features, along with attribute information describing what these features represent, are stored. Also known as digital map or digital cartographic data, locational data are stored in a vector or raster format. Corresponding attribute data are stored as sets of tables geographically related to the features they describe. Image data include ortophotos. Like spatial data, image data are georeferenced. The full set of ready-to-use data of Vulcano Island can be used to create maps in ELA or as a data source for further analyses carried out in using other software. ELA allows the use of image data, ARC/INFO coverages, ESRI shape files and CAD drawings but also many other formats such as SDE and TIN. Spatial and image data are thematically organized into different layers, or themes; there is one theme for each set of geographic features

(i.e. streams, elevation, and buildings were stored as a separate spatial data sources in order to make it easier the management and manipulation of data). A layer is a set of geographic data representing all the features in a particular ground surface feature class. Layers have a number of properties, displayed in the Table of Contents, that control the way it is displayed on the map; layer properties can be manipulated by specifying the range of scales at which the layer will be drawn on the map, by applying different classification techniques or by typing in user-defined classes. The purpose of classification is twofold: to make the process of understanding a map easier and to put in evidence non self-evident features about the area you're mapping. Each layer in a map is associated to a table where attributes about the geographic features it contains are stored. A layer's attribute table contains one record for each feature in the layer. The only layers that do not have attribute tables are layers representing image data. The active layers on the screen are listed in the Table of Contents. On the visualized map, whose scale may be observed on the toolbar. ELA software allows the performance of simple measurement operations (distances, areas and perimeters of polygons or circles) and the determination of the altimetric and planimetric coordinates of points. Moreover, ELA implements the possibility to draw and save control points, supplying a table of their altimetric and planimetric coordinates, and to graph profile, supplying its diagram and a table of the altimetric and planimetric coordinates of the points. Eventually, ELA can save the map to a project or export the map in .BMP and .EMF formats. A detailed user guide about the software functionalities, can be accessed clicking the appropriate button on the toolbar.

## **4. The Vulcano Island Files**

Spatial and image data of Vulcano Island are contained in the "Vulcano" directory. They are subdivided into eight subdirectories named "Cartography", "Dtm0101", "Dtm8305", "Dtm9605", "Dtm9610", "Flight", "Land" and "Ortophoto" (Table 1).

All the datasets are georeferenced in the same reference frame. The image data of the collection, with the .tif, .jpg and .ecw extensions, represent the Vulcano Island topographic map, the ortophotos and the DEM's elevation (contour lines), slope, aspect and hill shade representations of the island and of the volcano's

VULCANO		
DIRECTORIES	FILES	EXTENSIONS
Cartography	ctr90	.tif
Dtm0101	dtm0101_asp; dtm0101_dem; dtm0101_hil; dtm0101_slp;	.tif; .jpg;
Dtm8305	dtm8305_asp; dtm8305_dem; dtm8305_hil; dtm8305_slp;	.tif; .jpg;
Dtm9605	dtm9605_asp; dtm9605_dem; dtm9605_hil; dtm9605_slp;	.tif; .jpg;
Dtm9610	dtm9610_asp; dtm9610_dem; dtm9610_hil; dtm9610_slp;	.tif; .jpg;
Flight	flight	.shp
Land	buildings; coast; streams; streets	.shp
Ortophoto	Op00_1m_col; Op01_35cm_col; Op96_15cm_bn; Op96_1m_bn; Op00_1m_col_lr; Op01_35cm_col_lr; Op96_15cm_bn_lr; Op96_1m_bn_lr;	.ecw

**Table 1** Directories and files of the Vulcano Island’s CD-ROM.

cone. The “Layer properties” button on the toolbar gives the properties of each image visualized on the screen, such as the dataset filename, the layer extent (Emin, Emax, Nmin, Nmax) and the layer attribute data. DEM’s slope and aspect representations are coloured images subdivided into different zones according to different slope and aspect ranges; the colors table and the number of classes of the images may be changed by “layer style” button of the toolbar. DEM’s elevation has been represented by contour lines, whose properties (colour, classes, mode) may be changed by taking part on the options contained in “layer style” table. The spatial data of the collection, with the .shp extension, include streets (main and secondary roads), buildings, catchments lines, coastline and flight plane.

**Additional Information**

The work was carried out in the frame of the research activities of task 2 (Application Of Digital Terrain Models To Volcanology) of the GNV project n°13 “Development And Application Of Remote Sensing Methods For The Monitoring Of Active Italian Volcanoes” to which have contributed the following research units: UNIRM (M. Marsella), UNIBO (P. Baldi), UNIPD (V. Achilli), INGV-CT (G. Puglisi).

ELA is made by I.A.T. Ingegneria srl, a company specialized in services and solution for creating and managing spatial data in information systems.

**References**

Achilli V., Anzidei M., Baldi P., Marsella M., Mora P., Targa G., Vettore A., Vittuari L. (1997). *GPS and Digital Photogrammetry: an Integrated Approach for Monitoring Ground Deformations on a Volcanic Area*. In: Atti del Convegno ISPRS WG VI/3 “International cooperation and technology transfer” - 3- 7 Febbraio 1997- Padova. XXXII, 1-6.

Achilli V., Baldi P., Baratin L., Bonini C., Ercolani E., Gandolfi S., Anzidei M., Riguzzi F., (1998). *Digital photogrammetry survey on the island of Vulcano*. Acta Vulcanologica, 10,1,1-5.

Baldi P., Marsella M., Vittuari L., (1998). *Airborne GPS Performance during a Photogrammetric Project*. IAG Proceedings series Springer Verlag, 118, 343-348.

Baldi, P., S. Bonvalot, S., Briole, P., Marsella, M., (2000). *Digital photogrammetry and kinematic GPS for monitoring volcanic areas*. Geophysical. Journal International, 142, (3), 801-811.

Baldi P., Bonvalot S., Briole P., Coltelli M., Gwinner K., Marsella M., Puglisi G., Remy D., (2002). *Validation and comparison of different techniques for the derivation of digital elevation models and volcanic monitoring ( Vulcano Island, Italy)*. International Journal of Remote Sensing, 22, 4783-4800.

Barberi, F., Neri, G., Valenza, M. and Villari, L.

- (1991). *1987-1990 unrest at Vulcano*. Acta Vulcanologica, 1, 95-106.
- Keller, J., (1980). *The island of Vulcano*. Rendiconti Società Geologica Italiana, 36 (1), 369-414.
- Rasà, R. and Villari, L., (1988). *Geomorphological and morpho-structural investigations on La Fossa Cone*. Acta Vulcanologia, 1, 127-133.
- Tinti, S., Bortolucci, E. and Artigliato, A., (1999). *Numerical simulation of the landslide-induced tsunamis of 1988 in Vulcano Island, Italy*. Bulletin Volcanology, 61, 121-137.



**Istituto Nazionale di Geofisica e Vulcanologia**  
Via di Vigna Murata, 605 - 00143 Roma - Italy  
[www.ingv.it](http://www.ingv.it)